UNIVERSITY OF PADUA

Department of Civil and Environmental Engineering

Doctoral Thesis

Hydro-morphodynamics of tidal embayments and climate change

Ph.D. Student :
Jvan BARBARO

Advisor :
Prof. **Stefano LANZONI**

Padua - 2014

UNIVERSITÀ
DEGLI STUDI
DI PADOVA

Sede Amministrativa: Universitá degli Studi di Padova

Dipartimento di Ingegneria Civile, Edile ed Ambientale

DOTTORATO DI RICERCA IN

SCIENZE DELL'INGEGNERIA CIVILE ED AMBIENTALE

CICLO XXVI

Hydro-morphodynamics of tidal embayments and climate change

Coordinatore: Prof. Stefano LANZONI
Supervisore: Prof. Stefano LANZONI

Dottorando: Jvan BARBARO

Contents

Abstract

This thesis is motivated by the desire to understand better and to model some important aspects of tidal estuary. Three different subjects are studied: cross-section modelling; wind characterization in Venice Lagoon (Italy); drainage channel initiation.

It has been developed a physical based analytical model to study the estuary cross-section for hydrodynamics and sediment transport. The main focus is to study the effects of different boundary conditions.

At the bed, three condition are applied: the classical no-slip condition with constant eddy viscosity; a partial-slip condition with constant eddy viscosity; a no-slip condition with parabolic eddy viscosity profile. Solutions are investigated using scaling and perturbations methods. Whereas the partial-slip condition does not consistently improve the no-slip condition, the use of parabolic eddy viscosity is a really impressive progress: it allows a better understanding and representation of the physical dynamics of the environment.

Regarding wind in the Venice lagoon, it has been analysed an 11-years database of wind data taken in the lagoon and in the nearby sea. Wind statistics are studied by rose plots and nine probability density functions. This work results in a characterization of the annual, seasonal, monthly and hourly statistics of the wind in the lagoon.

The last argument of research concerns the modelling of drainage channel initiation in sheet flow condition. The analysis is specialized to model the periodic spacing of parallel drainage channels; this type of networks are present in many different environments and with a wide range of length-scales. The

model is analytical and physical based; solutions are searched by scaling and perturbation methods. The results point out that the main parameters are the water depth, the concentration of sediment, the critical velocity for sediment resuspension. Spacing of drainage channels are found for a wide range of parameters.

Riassunto

L'interesse di questa tesi é quello di meglio comprendere alcuni aspetti importanti degli ambienti a marea. In questo contesto, sono stati analizzati tre argomenti: modellazione delle sezioni trasversali di un estuario, caratterizzazione del vento nella laguna di Venezia e la formazione di canali di drenaggio.

Si é costruito un modello analitico per lo studio dell'idrodinamica e il trasporto dei sedimenti focalizzando l'attenzione alle sezioni trasversali. Lo scopo principale é stato quello di analizzare gli effetti dell'applicazione di differenti condizioni al contorno.

Al fondo sono state applicate tre differenti condizioni: quella classica di non scivolamento con viscositá di vortice costante, la condizione di parziale scivolamento con viscositá costante e la condizione di non scivolamento con profilo parabolico di viscositá. Le soluzioni sono state cercate attraverso l'utilizzo dell'analisi dimensionale e lo sviluppo perturbativo. La condizione di parziale scivolamento non ha comportato un miglioramento significativo rispetto al non scivolamento. Invece, la condizione di viscositá con profilo parabolico risultata una miglioria significativa: permette una migliore comprensione e rappresentazione della fisica del sistema.

Per quanto riguarda il vento in laguna di Venezia, si é studiato un database di 11 anni di dati di vento in laguna e nel mare vicino. Si sono utilizzati grafici di vento a settori e si sono calcolate le distribuzioni di probabilitá. Attraverso questo lavoro, si sono caratterizzati gli andamenti annuali, stagionali, mensili e orari.

L'ultimo argomento riguarda lo studio della formazione di canali di drenaggio in consizioni di flusso laminare. L'analisi riguarda lo studio della spaziatura dei canali a distribuzione parallela e periodica che caratterizzano diversi ambienti per un range ampio di parametri. Il modello é analitico e basato sulla fisica del sistema; le soluzioni sono ricercate attraverso l'analisi dimensionale e i metodi perturbativi. I risultati evidenziano che i parametri principali sono il battente d'acqua, la concentrazione, e la velocitá critica per la risospensione. Si sono trovati i valori di spaziatura dei canali per un ampio spettro di variazione dei parametri.

Thesis structure

This thesis is structured in three independent parts: cross-section modelling; wind characterization in Venice lagoon (Italy); drainage channel formation. The first and last parts are more theoretical, instead the second is more experimental.

Part one is composed of chapter 1 (from page 3). It is developed the analytical model of cross-section and it is used to study the effects of three different boundary conditions at the bed: the classical no-slip condition with constant eddy viscosity; a partial-slip condition with constant eddy viscosity; a no-slip condition with parabolic eddy viscosity profile.

The second part of the thesis consists of chapters 2 (from page 51), where it is analysed an 11-years database of wind data to characterized the wind statistics for the Venice lagoon.

Last part, chapter 3 (from page 121), concerns the study of drainage channel initiation in a sheet flow environment.

Notations

In the thesis, the following notation are used:

- Re, Im and Abs are used to express the real, imaginary and absolute part

of a function or value;

- the imaginary number is denoted as i;
- a star apex is generally used for dimensional quantities;
- square brackets are used to indicate the arguments of a function;
- in the arguments of a function, a semi-colon is used to divide the variables (on the left side) from the parameters (on the right side).

Part I

Cross-section modelling

Chapter 1

Modelling cross-section hydrodynamics and suspended sediment concentration in tidal estuaries: partial slip, no-slip, parabolic eddy viscosity comparison

Abstract

The present research focuses on the hydrodynamical processes and sediment trapping in cross-section in tidal estuaries. The main contribution is the analysis of the effects of three boundary condition at the bed: no-slip condition with constant and parabolic eddy viscosity; partial-slip with constant eddy viscosity.

This model is based on the shallow water equations for the hydrodynamics and the advection-diffusion equation for sediment concentration. The system of equations is closed by the morphodynamic equilibrium condition.

The water motion is forced by tides and density gradients. The estuary is well-mixed, uniform in the along-channel direction with an arbitrary lateral bathymetry. At the free surface it is applied a rigid-lid approximation.

An asymptotic expansion is used to solve the system of equations. The leading order solution consists of an M_2-tidal component for the flow velocity and the residual, and an M_4 component for sediment concentration. Only those component of the first order solution that are relevant for the leading order sediment transport are calculated, i.e. the residual of flow velocity and the M_2 component of the sediment concentration.

The model allows analytical solution of the water motion and sediment transport for the three considered boundary conditions. Considering constant eddy viscosity, the results show that the no-slip and partial slip boundary condition give very similar solutions. Considering the no-slip condition, the use of a parabolic eddy viscosity give a very different solution respect to the use of the classical constant eddy viscosity. The velocity profiles derived with parabolic eddy viscosity show high gradient in the first meter from the bed. In fact, with the parabolic eddy viscosity it is possible to resolved the boundary layer at the bed, whereas with the classical solution it is not possible.

1.1 Introduction

Velocity and suspended sediment concentration could vary significantly within estuarine cross-sections, within cross-sections over time, between cross-sections within an estuary and between estuaries (Valle-Levinson, 2010 [1]). The transverse distribution of velocity and suspended sediment plays a significant role in momentum balance, mixing and transport of material in many estuaries(Geyer, 1993 [2]). Another important aspects that mostly interest cross-section is sediments trapping (Huijts, 2010 [3]), as high concentrations of suspended sediment affect water quality (with all its consequence) and often coincide with pools of easily erodible sediments at the bed. This

means that a knowledge of flow and sediment distributions in estuarine cross-sections is relevant for effective management of estuaries.

The literature in cross-section modelling is becoming quite extensive; there are various approach that range from complex numerical models (e.g., Chen et al., 2009 [4]) to analytical model (e.g.,) and intermediate model (Burchard et al., 2011 [5]).

But only few works are interested in the effects of the different boundary conditions and eddy viscosity formulation. Even if Burchard et al. (2011 [5]) developed a state-of-the-art formulation for the vertical eddy viscosity in an estuarine cross section, to analyse the importance of eddy viscosity formulation on computed flow fields and to improve the physical knowledge of the problem, it is convenient to use analytical model, with which it is easier to properly recognize the effects of the different contributions in the equations.

However it seams very important to properly model the effect of the boundary layer and eddy viscosity formulation, because its direct influence on the entire circulation. Right now there is no confidence in this matter (see Zitman and Schuttelaars, 2012 [6]).

The attention is limited to only three type of boundary condition and eddy viscosity formulation (i.e., no-slip condition with constant and parabolic eddy viscosity; partial-slip with constant eddy viscosity) because these three alternatives cover the most frequently used parametrisations of the eddy viscosity profile ([6]).

The model presented in this study use the same equations and solution technique as in Huijts (2010, [3]) but here it is analysed the effects of different boundary condition.

In section 1.2 it is introduced the geometry of the analysed system and the general assumption and notations. The model is described in section 1.3, while the scaling of the equations is explained in section 1.4, and the perturbation analysis is developed in section 1.5. The analytical solution is reported in section 1.6; the results are shown in section 1.7. Finally section

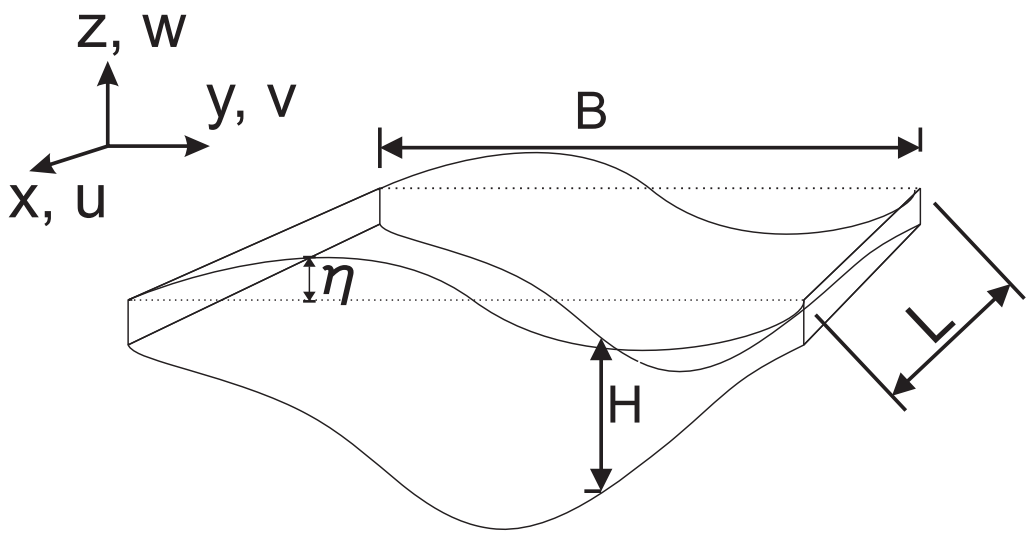

Figure 1.1: A sketch of the idealized embayment. A Cartesian coordinate system is taken such that x is the seaward oriented along channel coordinate, y is the cross-channel coordinate and its origin is on the left border of the estuary (landward looking) and z is the upward vertical coordinate with origin at the tidally averaged free surface. η and H denote the free surface and bed position, respectively.

1.8 reports the conclusions.

1.2 General assumptions, considerations and hypothesis

1.2.1 Basin geometry

Since the present research focuses on the hydrodynamical processes and sediment trapping in cross-section in tidal estuaries, a local model description is used. This model describes a specific cross-section of a estuarine section with a length L^* of the order of a kilometre. The length of this section is small compared to the overall estuary length, the tidal wavelength ($\sim$ 400 km), the tidal excursion length (tens of kilometres) and the geometric length scale ($\sim 5 - 40$ km). Assuming the bathymetry to be uniform in the longitudinal direction in the investigated estuary reach, the model results to be practically

two-dimensional, involving only the lateral and vertical coordinate.

The idealized estuary is infinitely long, with constant width B^*, and it has an arbitrary bathymetry in the cross-channel direction. The bathymetry is described by $z^* = -H^*[y^*]$, with H^* a positive function; in particular it is characterised by a minimum (and maximum) depth.

The orthogonal Cartesian reference system consists of a sea-ward oriented x-axis, a y-axis with the origin on the left bank, and an up-ward pointing z-axis, with origin at the mean water surface.

1.2.2 Hydrodynamics

The water motion is described by the shallow water equations on an f-plane for along-channel uniform conditions. The density variations over the depth are assumed to be negligible, i.e. the focus is on partially to well-mixed estuaries.

The water motion is driven by an externally prescribed M_2-tide with cross-sectional average velocity amplitude U_T^* and angular frequency ω_T. Furthermore, prescribed time-independent along-estuary density gradients induce a mean flow with typical velocity U_D^*. Lateral density gradients and Coriolis force result in lateral velocities with a typical magnitude V^*. The typical river discharge velocity, U_R^*, is assumed to be small compare to density driven velocities and, therefore, is neglected.

It is used the rigid lid approximation; this means that variation in surface elevation are neglected, but barotropic pressure gradients are retained and internally prescribed by boundary conditions.

Table 1.1 reports the values of the various parameters characterizing the estuary hydrodynamics.

1.2.3 Sediment and bed

Sediment consists of a single class of fine cohesionless particles, that is assumed to be transported as suspended load, without significant effects

Parameter	Typical value	Description
U_T^*	1 ms^{-1}	cross-section average velocity amplitude
ω_T	$1.4X10^{-}4$ s^{-1}	tide angular frequency
U_D^*	0.1 ms^{-1}	velocity amplitude induced by density gradient
V^*	0.1 ms^{-1}	lateral velocity amplitude
U_R^*	0.1 ms^{-1}	river discharge velocity amplitude

Table 1.1: The typical magnitude of the estuary hydrodynamics parameters.

on water density. Sediment in suspension can settle and deposit in mud reaches, forming layers of erodible sediments on top of a non-erodible bottom, $z^* = -H^*[y^*]$.

The distribution of mud reaches along the cross-section is described through a laterally varying erosion coefficient. This erosion coefficient has to be prescribed such that lateral sediment transport is in morphodynamic equilibrium, that is, tidally-averaged sediment erosion balances deposition at every location of the cross-section. The water depth is assumed to be unaffected by the presence of the mud reaches; hence, the erodible layer is necessarily thin compared to water depth.

Furthermore, the suspended sediment concentration, C_m^* ($\sim 10 - 100$ mg/l), is assumed to be small enough to not alter the water density significantly.

1.3 Model

1.3.1 Hydrodynamics

The estuarine hydrodynamics is described by the shallow water equations, that consist of mass and momentum conservation equations. The later equations are derived from the well known Navier-Stokes equations, taking into account the shallow character of the flow field, as described in the following.

3D shallow water equations

Taking into account the along-channel uniformity hypothesis, the mass conservation equation reduces to

$$\frac{\partial v^*}{\partial y^*} + \frac{\partial w^*}{\partial z^*} = 0 \tag{1.1}$$

The Navier-Stokes equations, written in vectorial form, read

$$\frac{d\vec{u^*}}{dt^*} = \frac{\partial \vec{u^*}}{\partial t^*} + \left(\vec{u^*} \cdot \nabla\right) \vec{u^*} = -\nabla\Phi^* - \frac{1}{\rho^*}\nabla p^* + \nu\nabla^2\vec{u^*} - 2\vec{\Omega^*} \times \vec{u^*} \tag{1.2}$$

where $\vec{u^*} = \vec{u^*}[x^*, y^*, z^*, t^*]$ is the flow velocity with components $\vec{u^*} = (u^*, v^*, w^*)$ along the longitudinal, lateral and vertical directions, respectively; Φ^* is the geopotential (see appendix B, page 147); $\rho^* = \rho^*[x^*, y^*, z^*, t^*]$ is the water density; ν is kinematic viscosity; $\vec{\Omega^*}$ is the Earth angular velocity; the scalar product is denoted by $\cdot$; ∇ is the gradient; ∇^2 is the Laplace operator; $\times$ is the cross product. Neglecting the small correction for the centrifugal force in the potential forces, the momentum equation 1.2 becomes

$$\frac{\partial \vec{u^*}}{\partial t^*} + \left(\vec{u^*} \cdot \nabla\right) \vec{u^*} = -\vec{g} - \frac{1}{\rho^*}\nabla p^* + \nu\nabla^2\vec{u^*} - 2\vec{\Omega^*} \times \vec{u^*} \tag{1.3}$$

where $\vec{g}$ is the gravitational acceleration. Integrating over turbulence (Reynolds average), equation 1.3 becomes

$$\frac{\partial \vec{u^*}}{\partial t^*} + \left(\vec{u^*} \cdot \nabla\right) \vec{u^*} = -\vec{g} - \frac{1}{\rho^*}\nabla p^* + \nu\nabla^2\vec{u^*} - \nabla(\vec{A^*}\nabla\vec{u^*}) - 2\vec{\Omega^*} \times \vec{u^*} \tag{1.4}$$

where $A^* = (A_x^*, A_y^*, A_z^*)$ is the eddy viscosity coefficient and the turbulence average operator $< \cdots >$ has been removed for the sake of simplicity. From now on, the fluid variables are assumed to be average over turbulence. The vectorial equation 1.4, splitted in the components along the three reference

axes, becomes

$$\frac{\partial u^*}{\partial t^*} + u^*\frac{\partial u^*}{\partial x^*} + v^*\frac{\partial u^*}{\partial y^*} + w^*\frac{\partial u^*}{\partial z^*} = \\ -\frac{1}{\rho^*}\frac{\partial p^*}{\partial x^*} + \nu\nabla^2 u^* - \nabla(A^*\nabla u^*) - 2\Omega^*(w^*\cos\varphi^* - v^*\sin\varphi^*) \quad (1.5)$$

$$\frac{\partial v^*}{\partial t^*} + u^*\frac{\partial v^*}{\partial x^*} + v^*\frac{\partial v^*}{\partial y^*} + w^*\frac{\partial v^*}{\partial z^*} = \\ -\frac{1}{\rho^*}\frac{\partial p^*}{\partial y^*} + \nu\nabla^2 v^* - \nabla(A^*\nabla v^*) - 2\Omega^* u^*\sin\varphi^* \quad (1.6)$$

$$\frac{\partial w^*}{\partial t^*} + u^*\frac{\partial w^*}{\partial x^*} + v^*\frac{\partial w^*}{\partial y^*} + w^*\frac{\partial w^*}{\partial z^*} = \\ -g - \frac{1}{\rho^*}\frac{\partial p^*}{\partial z^*} + \nu\nabla^2 w^* - \nabla(A^*\nabla w^*) - 2\Omega^* u^*\cos\varphi^* \quad (1.7)$$

Under the assumption (usually satisfied in the field) that the Coriolis vertical component is smaller than gravity ($\Omega^* u^* << g$) and the vertical velocity is much smaller than horizontal velocity ($w^* << u^*, w^* << v^*$, shallow water assumption), the Coriolis force can be approximate as

$$-2\vec{\Omega^*} \times \vec{u^*} \sim -f e_3 \times \vec{u^*} \quad (1.8)$$

where $f = 2\Omega^*\sin\varphi^*$ is the Coriolis parameter.

Using the hydrostatic assumption, eq. 1.7 could be approximate by

$$-g - \frac{1}{\rho^*}\frac{\partial p^*}{\partial z^*} = 0 \quad (1.9)$$

which yields

$$p^* = g\int_{z^*}^{\eta^*} \rho^*\, dz + p_{atm} \quad (1.10)$$

with p_{atm} the atmospheric pressure at the water surface $\eta^*[x^*, y^*, t^*]$. The atmospheric pressure is assumed to be constant. With the present assumption,

ρ^* is not dependent on z, so it follows that

$$p^* = g\rho^*(\eta^* - z^*) + p_{atm} \tag{1.11}$$

Inserting eq 1.11 into eq. 1.5 and 1.6, it yields

$$\frac{\partial u^*}{\partial t^*} + u^*\frac{\partial u^*}{\partial x^*} + v^*\frac{\partial u^*}{\partial y^*} + w^*\frac{\partial u^*}{\partial z^*} = \\ - g\frac{\partial \eta^*}{\partial x^*} + \frac{g}{\rho^*}\frac{\partial \rho^*}{\partial x^*}z + \nu\nabla^2 u^* - \nabla(A^*\nabla u^*) - 2\Omega^*(w^*\cos\varphi^* - v^*\sin\varphi^*) \tag{1.12}$$

$$\frac{\partial v^*}{\partial t^*} + u^*\frac{\partial v^*}{\partial x^*} + v^*\frac{\partial v^*}{\partial y^*} + w^*\frac{\partial v^*}{\partial z^*} = \\ - g\frac{\partial \eta^*}{\partial y^*} + \frac{g}{\rho^*}\frac{\partial \rho^*}{\partial y^*}z + \nu\nabla^2 v^* - \nabla(A^*\nabla v^*) - 2\Omega^* u^*\sin\varphi^* \tag{1.13}$$

$$\tag{1.14}$$

Because of the along-channel uniformity hypothesis, terms containing the longitudinal derivative of the velocity $\frac{\partial \vec{u}}{\partial x^*}$ vanish.

The longitudinal ($\frac{\partial \rho^*}{\partial x^*}$) and lateral ($\frac{\partial \rho^*}{\partial y^*}$) tidally-averaged density gradients are externally prescribed on the basis of the data, characterizing a specific estuary.

Moreover, dimensional analysis indicates that the horizontal component of the eddy viscosity is negligible compared to the leading order contributions in the equations.

The momentum equations then reduce to

$$\frac{\partial u^*}{\partial t^*} + v^*\frac{\partial u^*}{\partial y^*} + w^*\frac{\partial u^*}{\partial z^*} = \frac{g}{\rho_{ref}}\frac{\partial \rho^*}{\partial x^*}z^* - g\frac{\partial \eta^*}{\partial x^*} + \frac{\partial}{\partial z^*}\left(A_z^*\frac{\partial u^*}{\partial z^*}\right) + fv^* \tag{1.15}$$

$$\frac{\partial v^*}{\partial t^*} + v^*\frac{\partial v^*}{\partial y^*} + w^*\frac{\partial v^*}{\partial z^*} = \frac{g}{\rho_{ref}}\frac{\partial \rho^*}{\partial y^*}z^* - g\frac{\partial \eta^*}{\partial y^*} + \frac{\partial}{\partial z^*}\left(A_z^*\frac{\partial v^*}{\partial z^*}\right) - fu^* \tag{1.16}$$

where ρ_{ref} is a constant reference density determined by Boussinesq closure.

Boundary conditions and forcing

The shear stress is assumed to vanish at the free water surface, where the kinematic boundary conditions hold; in the rigid lid approximation these conditions imply

$$\begin{cases} w^* = 0 \\ A_z^* \dfrac{\partial u^*}{\partial z^*} = 0 \\ A_z^* \dfrac{\partial v^*}{\partial z^*} = 0 \end{cases} \qquad \text{at } z^* = 0 \tag{1.17}$$

Although the estuary bed is assumed to be impermeable, two different boundary conditions are investigated:
I: a no-slip condition

$$u^* = v^* = w^* = 0 \qquad \text{at } z^* = -H^*[y^*] \tag{1.18}$$

II: a partial slip condition

$$\begin{cases} w^* = 0 \\ A_z^* \dfrac{\partial u^*}{\partial z^*} = s^* u^* \\ A_z^* \dfrac{\partial v^*}{\partial z^*} = s^* v^* \end{cases} \qquad \text{at } z^* = -H^*[y^*] \tag{1.19}$$

where s^* is partial slip parameter chosen on the basis of the measured velocity profile (see Schramkowskiand de Swart, 2002 [7]).
In case of a no-slip boundary condition, both a constant and a parabolic eddy viscosity profile are considered.

At the lateral boundaries there is no overall lateral flux of water. Hence, the following integral condition holds:

$$\int_{-H^*}^{0} v^* \, dz = 0 \text{ at } y^* \in \{0, B^*\} \tag{1.20}$$

which, in turn, implies that the overall lateral water flux vanishes at each

location in the cross-section:

$$\int_{-H^*}^{0} v^* \, dz = 0 \text{ for all } y^* \tag{1.21}$$

Finally, a semi-diurnal tidal discharge is imposed over the cross-section:

$$\frac{1}{S^*} \int_0^{B^*} \int_{-H^*}^{0} u^* dz dy = U^* \cos\left(\omega_T t^*\right) \tag{1.22}$$

where S^* is the cross-section area

$$S^* = \int_0^{B^*} H^*[y^*] \, dy \tag{1.23}$$

1.3.2 Eddy viscosity models

Constant eddy viscosity profile

The no-slip and partial-slip boundary conditions are considered in conjuction with an eddy viscosity modelled as proposed by Munk and Anderson (1948, [8]), Bowden (1959, [9]) and Dyer (1973, [10]). In the presence of stratification, it reads

$$A_z^* = A_0(1 + 10Ri)^{-1/2} \tag{1.24}$$

where

$$A_0 = 2.5 \times 10^{-3} U_T^* H_0^* \tag{1.25}$$

is the vertical eddy viscosity coefficient in absence of stratification, and U_T is the tide-average mean velocity amplitude. The coefficient H_0 is half cross-section averaged water depth, and Ri is the Richardson number defined on the basis of a typical density difference between bed and surface $\Delta\rho$

$$Ri = g \frac{\Delta\rho}{\rho_{ref}} \frac{H_0^*}{U_T^{*2}}. \tag{1.26}$$

Note that the Richardson number and the vertical eddy viscosity are assumed constant in time and z.

Parabolic eddy viscosity profile model

The other considered eddy viscosity profile is a parabolic profile. This takes into account the vertical variation of eddy viscosity which is described by a two parameter equation

$$A_z^*[y^*, z^*] = A_0 \left(1 - \left(\frac{\sqrt{1-R}}{1-\delta}\left(\frac{z^*}{H^*} + \delta\right)\right)^2\right)(1 + 10Ri)^{-1/2} \qquad (1.27)$$

Here the parameter R, varying in the interval (0,1), controls the value of eddy viscosity at the bed, while δ parametrizes the depth at which the maximum eddy viscosity occurs, ranging from 0 to $\left(1+\sqrt{1-R}\right)^{-1}$. A_0 and Ri are the same.

1.3.3 Sediment dynamics

The sediment mass balance equation, given the shallow water assumption and the along-estuary uniform condition, simplifies to

$$\frac{\partial c^*}{\partial t^*} + \frac{\partial}{\partial y^*}\left(v^* c^* - K_y \frac{\partial c^*}{\partial y^*}\right) + \frac{\partial}{\partial z^*}\left(\left(w^* - w_s\right) c^* - K_z \frac{\partial c^*}{\partial z^*}\right) = 0 \qquad (1.28)$$

where c^* is the sediment concentration, w_s is the settling velocity while K_y and K_z are the lateral and vertical eddy diffusivity coefficients, assumed to be constant. In particular, it is used $K_y = 5\ m^2 s^{-1}$ (Fisher et al., 1979 [11]) while K_z is parametrized as suggested by Munk and Anderson (1948, [8])

$$K_z = A_0(1 + 3.33Ri)^{-3/2} \qquad (1.29)$$

for a vertically constant eddy viscosity, and

$$K_z = A_0 \left(1 - \left(\frac{\sqrt{1-R}}{1-\delta}\left(\frac{z^*}{H^*}+\delta\right)\right)^2\right)(1+3.33Ri)^{-3/2} \tag{1.30}$$

for parabolic eddy viscosity.

Similar to the boundary conditions for the lateral water flux, the lateral sediment transport has to vanish at the lateral boundaries

$$\int_{-H^*}^{0}\left(v^*c^* - K_y\frac{\partial c^*}{\partial y^*}\right)dz = 0 \text{ at } y^* \in \{0, B^*\} \tag{1.31}$$

The sediment flux through the water surface must vanish:

$$w_s c^* + K_z\frac{\partial c^*}{\partial z^*} = 0 \text{ at } z^* = 0 \tag{1.32}$$

The sediment flux normal to the bed consists of an erosion and deposition flux. The erosion E_s^* is modelled as

$$E_s^* \equiv -K_y\frac{\partial c^*}{\partial y^*}n_y - K_z\frac{\partial c^*}{\partial z^*}n_z = w_s c_* \text{ at } z^* = -H^*[y^*] \tag{1.33}$$

where $\vec{n} = (n_y, n_z)$ is the upward unit vector normal to the bottom and c_* is a reference concentration modelled as

$$c_*[y^*, t^*] = \rho_s\frac{|\tau_b^*[y^*, t^*]|}{(\rho_s - \rho_{ref})\, g d_s}a^*[y^*] \tag{1.34}$$

Here ρ_s is the sediment density, τ_b^* the bed shear stress, d_s is the sediment grain size and $a^*[y^*]$ is the erosion coefficient, that is related to the amount of sediment available for resuspension at the bed. The bed shear stress is defined at $z^* = -H^*[y^*]$ by

$$\vec{\tau_b^*} = \rho_{ref}A_z^*[z^* = -H^*[y^*]]\frac{\partial\vec{u^*}}{\partial z^*} \tag{1.35}$$

The bed shear stress is assumed to be much larger than the critical bed shear

stress for sediment erosion. Clearly, at equilibrium $c^* = c_*$.

The deposition flux normal to the bed D^* is modelled as

$$D^* \equiv w_s c^* n_z \text{ at } z^* = -H^*[y^*] \tag{1.36}$$

In morphodynamic equilibrium, the tidally averaged rate of bed variation vanishes,

$$< \frac{\partial z_b^*}{\partial t^*} >= \frac{1}{T} \int_0^T \frac{\partial z_b^*}{\partial t^*} \, d\tau = 0 \tag{1.37}$$

where z_b^* is the bed elevation and angular bracket denote tidal-averaging.

The Exner equation describing bed evolution can be written as

$$(1-p)\frac{\partial z_b^*}{\partial t^*} = D^* - E_s^* \tag{1.38}$$

with p sediment porosity.

The equilibrium condition 1.37 implies that a balance exists between deposition and erosion, such that

$$< D^* > - < E_s^* >= 0 \tag{1.39}$$

Integrating over the depth, the sediment mass balance equation 1.28 gives

$$\int_{-H^*}^{0} \left(\frac{\partial c^*}{\partial t^*} + \frac{\partial}{\partial y^*} \left(v^* c^* - K_y \frac{\partial c^*}{\partial y^*} \right) + \frac{\partial}{\partial z^*} \left(\left(w^* - w_s \right) c^* - K_z \frac{\partial c^*}{\partial z^*} \right) \right) \, dz = 0 \tag{1.40}$$

Using Leibniz integral rule, one finds

$$\int_{-H^*}^{0} \frac{\partial c^*}{\partial t^*} \, dz + \frac{\partial}{\partial y^*} \int_{-H^*}^{0} \left(v^* c^* - K_y \frac{\partial c^*}{\partial y^*} \right) \, dz - \left(v^* c^* - K_y \frac{\partial c^*}{\partial y^*} \right) \Big|_{-H^*} \frac{\partial H^*}{\partial y^*} + \\ + \left(\left(w^* - w_s \right) c^* - K_z \frac{\partial c^*}{\partial z^*} \right) \Big|_{-H^*}^{0} = 0 \tag{1.41}$$

Taking into account the boundary conditions at the water surface $z^* = 0$ and

at the bed $z^* = -H^*[y^*]$, along with the definition for D^* and E_s^*, it follows that

$$\int_{-H^*}^{0} \frac{\partial c^*}{\partial t^*}\, dz + \frac{\partial}{\partial y^*} \int_{-H^*}^{0} \left(v^* c^* - K_y \frac{\partial c^*}{\partial y^*} \right) dz + \\ + \left(K_y \frac{\partial c^*}{\partial y^*} \right) \Big|_{-H^*} \frac{\partial H^*}{\partial y^*} + \left(w_s c^* + K_z \frac{\partial c^*}{\partial z^*} \right) \Big|_{-H^*} = 0 \tag{1.42}$$

and rearranging

$$\int_{-H^*}^{0} \frac{\partial c^*}{\partial t^*}\, dz + \frac{\partial}{\partial y^*} \int_{-H^*}^{0} \left(v^* c^* - K_y \frac{\partial c^*}{\partial y^*} \right) dz = \\ = \left(-K_y \frac{\partial c^*}{\partial y^*} \right) - \left(w_s c^* + K_z \frac{\partial c^*}{\partial z^*} \right) \equiv D^* - E_s^* \tag{1.43}$$

Averaging over a tidal period and considering the system in morphodynamic equilibrium, it follows that

$$\frac{\partial}{\partial y^*} \int_{-H^*}^{0} \left(< v^* c^* > - K_y < \frac{\partial c^*}{\partial y^*} > \right) dz = < D^* > - < E_s^* > = 0 \tag{1.44}$$

Recalling the lateral boundary condition on the lateral sediment transport, the morphodynamic equilibrium implies

$$\int_{-H^*}^{0} \left(< v^* c^* > - K_y < \frac{\partial c^*}{\partial y^*} > \right) dz = 0 \text{ for all } y^* \tag{1.45}$$

Essentially, the mean balance between deposition and erosion requires a mean balance between advective and diffusive sediment transport in the lateral direction along each vertical section. In the following, equation 1.45 will be refereed to as the morphodynamic equilibrium condition.

Recalling the definition of the erosion E_s^* (eq. 1.33) and that the reference concentration c_* (eq. 1.34) has been assumed to vary linearly with the erosion coefficient $a^*[y^*]$, the morphodynamic equilibrium condition can be written

as a first order linear differential equation for the erosion coefficient

$$I_1 \frac{\partial a^*}{\partial y^*} + I_2 a^* = 0 \tag{1.46}$$

where I_1 and I_2 are known integrals given by

$$I_1 = \int_{-H^*[y^*]}^{0} -K_y < \frac{c^*}{a^*} > dz \tag{1.47}$$

$$I_2 = \int_{-H^*}^{0} \left(< v \frac{c^*}{a^*} > -K_y \frac{\partial < \frac{c^*}{a^*} >}{\partial y^*} \right) dz \tag{1.48}$$

To determine the integration constant needed to solve eq. 1.46, an additional condition is required, namely

$$\frac{1}{B^*} \int_0^{B^*} a^*[y^*] \, dy = a_* \tag{1.49}$$

Here a_* is a reference value for the average amount of sediment available for resuspension in the cross-section. In particular a_* is prescribed considering the order of magnitude of sediment concentration that is expected on the basis of field observations.

1.4 Scaling

The various quantities defined so far are scaled as

$$x^* = L^* x,\ y^* = B^* y,\ z^* = H_0^* z,\ t^* = \frac{1}{\omega_T} t \tag{1.50}$$

$$u^* = U_T^* u,\ v^* = V^* v,\ w^* = \frac{V^* H_0^*}{B^*} w \tag{1.51}$$

$$H^* = H_0^* H,\ S^* = B^* H_0^* S \tag{1.52}$$

$$a^* = a_* a,\ \tau_b^* = \frac{\rho_{ref} A_z^* U_T^*}{H_0^*} \tau_b,\ c^* = \frac{\rho_s \rho_{ref} A_z^* U_T^* a_*}{H_0^* \left(\rho_s - \rho_{ref}\right) g d_s} c \tag{1.53}$$

$$\left(\frac{\partial^2 u}{\partial z^2}\right)^* = \frac{U_T^*}{H_0^{*2}} \left(\frac{\partial^2 u}{\partial z^2}\right),\ \left(\frac{\partial^2 v}{\partial z^2}\right)^* = \frac{f U_T^*}{\omega_T H_0^{*2}} \left(\frac{\partial^2 v}{\partial z^2}\right) \tag{1.54}$$

$$\left(\frac{\partial \eta}{\partial x}\right)^* = \frac{\omega_T U_T^*}{g} \left(\frac{\partial \eta}{\partial x}\right),\ \left(\frac{\partial \eta}{\partial y}\right)^* = \frac{f U_T^*}{g} \left(\frac{\partial \eta}{\partial y}\right) \tag{1.55}$$

$$A_z^* = \omega_T H_0^{*2} A_z,\ k_z^* = \omega_T H_0^{*2} k_z,\ \omega_s^* = \omega_T H_0^* \omega_s,\ f^* = \omega_T f \tag{1.56}$$

where a star apex denotes dimensional variables. This scaling is the same as in Huijts (2010, [3]), see there for details.

From eq. 1.19, it follows that

$$s^* = \omega_T H_0 s \tag{1.57}$$

where it has been used that $A_z^*/(\omega_T H_0^{*2}) \approx 1$, that means that friction is alwayes important in the full water column.

Since lateral gradients are effective over the topographic length scale defined by

$$L_{top} = \frac{H_0^*}{mean \left| \frac{\partial H}{\partial y} \right|}. \tag{1.58}$$

in the present analysis we assume that $L_{top} \sim B^*$. If this is not the case, the equations should be scaled with L_{top} (see Zitman and Schuttelaars, 2012 [6]).

The scaling follows from the main balances in the hydrodynamic and sediment equations. Considering the order of magnitude of the various dimen-

sionless terms (see tab. 1.2) in the longitudinal momentum equation, there must be a balance among local inertial, eddy viscosity and the surface slope. Imposing that these terms are of the same order yields the scaling for longitudinal velocity curvature ($\frac{\partial^2 u}{\partial z^2}$) and lateral surface gradient ($\frac{\partial \eta}{\partial x}$). Recalling that the longitudinal eddy viscosity scales as $\frac{U_T^*}{H_0^{*2}}$ it follows $\frac{A_z^*}{\omega_T H_0^{*2}} \sim 1$. On the other hand the lateral momentum equation is characterized by a balance among Coriolis force, eddy viscosity and the surface slope. Imposing that these terms are of the same order yields the scaling for the lateral velocity curvature ($\frac{\partial^2 v}{\partial z^2}$) and the lateral surface gradient ($\frac{\partial \eta}{\partial y}$).

The resulting dimensionless shallow water equations then read

$$\frac{\partial u}{\partial t} + \frac{V^*}{\omega_T B^*}\left(v\frac{\partial u}{\partial y} + w\frac{\partial u}{\partial z}\right) = \frac{U_D}{U_T}z - \left(\frac{\partial \eta}{\partial x}\right) + \frac{1}{\omega_T H_0^2}\left(\frac{\partial}{\partial z}A_z\frac{\partial u}{\partial z}\right) + \frac{V^* f}{\omega_T U_T}v \tag{1.59}$$

$$\frac{V^*}{U_T}\frac{\partial v}{\partial t} + \frac{V^*}{U_T}\frac{V^*}{\omega_T B^*}\left(v\frac{\partial v}{\partial y} + w\frac{\partial v}{\partial z}\right) = \\ = \frac{U_D}{U_T}\frac{\left(\frac{\partial \rho}{\partial y}\right)^*}{\left(\frac{\partial \rho}{\partial x}\right)^*}z - \frac{f}{\omega_T}\left(\frac{\partial \eta}{\partial y}\right) + \frac{f}{\omega_T}\frac{1}{\omega_T H_0^2}\left(\frac{\partial}{\partial z}A_z\frac{\partial v}{\partial z}\right) - \frac{f}{\omega_T}u \tag{1.60}$$

$$\frac{\partial v}{\partial y} + \frac{\partial w}{\partial z} = 0 \tag{1.61}$$

where $U_D \equiv \frac{gH_0}{\omega_T \rho_0}\frac{\partial \rho}{\partial x}$ is the typical velocity scale for the density driven mean circulation. Note that $\frac{\partial \rho}{\partial x}$ is prescribed uniformly in the cross-section. The dimensionless sediment mass balance equation becomes

$$\frac{\partial c}{\partial t} + \frac{V^*}{\omega_T B^*}\left(v\frac{\partial c}{\partial y} + w\frac{\partial c}{\partial z} - \frac{K_y}{V^* B^*}\frac{\partial^2 c}{\partial y^2}\right) - \frac{w_s}{\omega_T H_0}\frac{\partial c}{\partial z} - \frac{1}{\omega_T H_0^2}\left(\frac{\partial}{\partial z}K_z\frac{\partial c}{\partial z}\right) = 0 \tag{1.62}$$

The boundary and integral conditions associated with the flow field are

$$w = A_z \frac{\partial u}{\partial z} = A_z \frac{\partial v}{\partial z} = 0 \text{ at } z = 0 \tag{1.63}$$

$$u = v = w = 0 \text{ at } z = -H[y] \tag{1.64}$$

$$\int_{-H}^{0} v\, dz = 0 \text{ for all y} \tag{1.65}$$

$$\frac{1}{S} \int_0^1 \int_{-H}^{0} u dz dy = \cos[t] \tag{1.66}$$

where

$$S = \int_0^1 H[y]\, dy \tag{1.67}$$

In the case of the partial-slip boundary condition at the bed, eq. 1.64 has to be replaced by

$$\begin{cases} w = 0 \\ A_z \dfrac{\partial u}{\partial z} = u \\ A_z \dfrac{\partial v}{\partial z} = v \end{cases} \qquad \text{at } z = -H[y] \tag{1.68}$$

The dimensionless boundary conditions for suspended sediment concentration become

$$\int_{-H}^{0} \left(vc - \frac{K_y}{V^* B^*} \frac{\partial c}{\partial y} \right) dz = 0 \text{ at } y \in \{0, 1\} \tag{1.69}$$

$$\frac{w_s}{\omega_T H_0} c + \frac{K_z}{\omega_T H_0^2} \frac{\partial c}{\partial z} = 0 \text{ at } z = 0 \tag{1.70}$$

$$E_s \equiv -\frac{K_y}{V^* B^*} \frac{V^*}{\omega_T B^*} \frac{\partial c}{\partial y} n_y - \frac{K_z}{\omega_T H_0^2} \frac{\partial c}{\partial z} n_z = \frac{w_s}{\omega_T H_0} c_* \text{ at } z = -H[y] \tag{1.71}$$

$$c_* = |\tau_b|\, a \tag{1.72}$$

$$\vec{\tau}_b = A_z \frac{\partial \vec{u}}{\partial z} \tag{1.73}$$

Finally, the morphodynamic equilibrium condition equation and the integral

Parameter	Value	Assumption	Description
$\varepsilon \equiv \frac{V^*}{U_T}$	0.1	$O[\varepsilon]^1$	lateral vs. longitudinal scale
$\frac{f}{\omega_T}$	0.6	$O[1]$	scaled Coriolis parameter
$\frac{A_z}{H_0^2\omega_T}$	1	$O[1]$	scaled vertical eddy viscosity parameter
$\frac{K_z}{H_0^2\omega_T}$	0.7	$O[1]$	scaled vertical eddy diffusivity coefficient
$\frac{\omega_s}{H_0\omega_T}$	0.7	$O[1]$	scaled settling velocity parameter
$\frac{\left(\frac{\partial\rho}{\partial y}\right)}{\left(\frac{\partial\rho}{\partial x}\right)}$	2	$O[1]$	lateral vs. longitudinal density gradient
$\frac{K_y}{B^*V^*}$	0.03	$O[\varepsilon]^1$	scaled lateral eddy diffusivity coefficient
$\frac{U_D}{U_T}$	0.3	$O[\varepsilon]^1$	density-induced flow vs. tidal velocity amplitude
$\frac{V^*}{B^*\omega_T}$	0.06	$O[\varepsilon]^2$	internal lateral advection scale vs. width

Table 1.2: The typical magnitude of the dimensionless parameters

condition, necessary to fix the total amount of sediment in the cross-section, become

$$\int_{-H}^{0} \left(< vc > - \frac{K_y}{V^*B^*} < \frac{\partial c}{\partial y} > \right) dz = 0 \text{ for all y} \tag{1.74}$$

$$\int_0^1 a \, dy = 1 \tag{1.75}$$

Following Huijts (2010 [3]), it is assumed that the non-linear (inertial) terms in the momentum and sediment mass balance equations are $o(\epsilon^2)$.

1.5 Perturbation analysis

Solutions of the scaled equations (1.59-1.62) are derived as perturbation series in power of the small parameter $\varepsilon \equiv V^*U_T \sim 0.1$

$$\Psi = \Psi_0 + \varepsilon\Psi_1 + o(\varepsilon^2) \tag{1.76}$$

where $\Psi = \{u, v, w, \frac{\partial\eta}{\partial x}, \frac{\partial\eta}{\partial y}, c\}$ and the subscript denotes the component order of approximation. The various dimensionless numbers are ordered sort ϵ in table 1.2.

Using this expansion, a leading order system of equations (ε^0-term) and a higher order system of equation (ε^1-term) are obtained and analytically

solved.

Leading order problem

The dimensionless equations for the $O[\varepsilon^0]$ flow field are given by

$$\frac{\partial u_0}{\partial t} = -\frac{\partial \eta_0}{\partial x} + A_z \frac{\partial^2 u_0}{\partial z^2} \tag{1.77}$$

$$\frac{\partial \eta_0}{\partial y} - A_z \frac{\partial^2 v_0}{\partial z^2} + f u_0 = 0 \tag{1.78}$$

$$\frac{\partial v_0}{\partial y} + \frac{\partial w_0}{\partial z} = 0 \tag{1.79}$$

In case of no-slip boundary condition at the bottom, the boundary and integral conditions read

$$u_0 = v_0 = w_0 = 0 \text{ at } z = -H[y] \tag{1.80}$$

The condition of a stress free surface and no normal flow through the surface is given by

$$w_0 = \frac{\partial u_0}{\partial z} = \frac{\partial v_0}{\partial z} = 0 \text{ at } z = 0 \tag{1.81}$$

and no lateral water transport

$$\int_{-H}^{0} v_0 \, dz = 0 \text{ for all y} \tag{1.82}$$

At the leading order the forcing reads

$$\frac{1}{S} \int_0^1 \int_{-H}^{0} u_0 dz dy = \cos[t] \tag{1.83}$$

In case of partial slip assumption at the bed, eq. 1.80 reads

$$\begin{cases} w_0 = 0 \\ A_z \dfrac{\partial u_0}{\partial z} = s u_0 \qquad \text{at } z = -H[y] \\ A_z \dfrac{\partial v_0}{\partial z} = s v_0 \end{cases} \tag{1.84}$$

The longitudinal leading order flow is driven by a balance among local acceleration, the surface gradient forcing and turbulent friction. The lateral leading order flow is governed by a balance among the lateral surface gradient, Coriolis forcing and turbulent friction.

The water motion is forced by the semi-diurnal M_2-tide. The lateral flow is forced at the semi-diurnal frequency by the Coriolis force. For convenience, a second subscript will denote the tidal harmonic components of a particular term (e.g., u_{02}).

Because a semi-diurnal tidal discharge is imposed, at leading order only the M_2 component of the velocity is not zero (the other normal modes vanish). On the other hand, the leading order suspended sediment concentration is determined by a balance between local inertia, vertical settling and vertical diffusion effects

$$\frac{\partial c_0}{\partial t} - w_s \frac{\partial c_0}{\partial z} - \frac{\partial}{\partial z}\left(K_z \frac{\partial c_0}{\partial z} \right) = 0 \tag{1.85}$$

implying that the leading order concentration c_0 is determined by a balance in the vertical.

The boundary conditions at the bottom read

$$-K_z \frac{\partial c_0}{\partial z} = w_s \left| \frac{\partial \vec{u_{02}}}{\partial z} \right| a \text{ at } z = -H[y] \tag{1.86}$$

and at the surface

$$w_s c_0 + K_z \frac{\partial c_0}{\partial z} = 0 \text{ at } z = 0 \tag{1.87}$$

The presence of the absolute value of the vertical velocity gradient in 1.86, implies that at the leading order the sediment concentration can be written as a Fourier series which contains a mean term and even over-tides of M_2,

$$c_0 = c_{00} + c_{04} + ... \tag{1.88}$$

First order problem

The $o[\varepsilon^1]$ flow field problem is given by the equations

$$\frac{\partial u_1}{\partial t} = \frac{U_D}{U_T} z - \left(\frac{\partial \eta_1}{\partial x}\right) + A_z \left(\frac{\partial^2 u_1}{\partial z^2}\right) + f v_0 \tag{1.89}$$

$$\frac{\partial v_0}{\partial t} = \frac{U_D}{U_T} \frac{\left(\frac{\partial \rho}{\partial y}\right)}{\left(\frac{\partial \rho}{\partial x}\right)} z - \left(\frac{\partial \eta_1}{\partial y}\right) + A_z \left(\frac{\partial^2 v_1}{\partial z^2}\right) - f u_1 \tag{1.90}$$

$$\frac{\partial v_1}{\partial y} + \frac{\partial w_1}{\partial z} = 0 \tag{1.91}$$

with boundary and integral conditions: no slip and no normal flow at the bottom

$$u_1 = v_1 = w_1 = 0 \text{ at } z = -H[y] \tag{1.92}$$

no stress at the water surface and no normal flow through the free surface

$$w_1 = \frac{\partial u_1}{\partial z} = \frac{\partial v_1}{\partial z} = 0 \text{ at } z = 0 \tag{1.93}$$

and no lateral water transport at any location in the cross-section

$$\int_{-H}^{0} v_1 \, dz = 0 \text{ for all y} \tag{1.94}$$

In case of partial slip assumption at the bed, eq. 1.92 reads

$$\begin{cases} w_1 = 0 \\ A_z \dfrac{\partial u_1}{\partial z} = s u_1 \qquad \text{at } z = -H[y] \\ A_z \dfrac{\partial v_1}{\partial z} = s v_1 \end{cases} \tag{1.95}$$

The presence of v_0 in 1.89 induces a forcing on u_1 with an M_2 frequency, and the presence of a time-independent density gradient in the longitudinal direction results in a residual flow component. This suggests a decomposition of the form

$$u_1 = u_{10} + u_{12} + \dots \tag{1.96}$$

$$v_1 = v_{10} + v_{12} + \dots \tag{1.97}$$

The equation and boundary conditions for suspended sediment concentration are

$$\frac{\partial c_1}{\partial t} - w_s \frac{\partial c_1}{\partial z} - K_z \frac{\partial^2 c_1}{\partial z^2} = 0 \tag{1.98}$$

$$K_z \frac{\partial c_1}{\partial z} = -w_s \frac{\frac{1}{2}\left(\frac{\partial u_0}{\partial z} \cdot \left(\frac{\partial u_1}{\partial z}\right)^* + \frac{\partial u_1}{\partial z} \cdot \left(\frac{\partial u_0}{\partial z}\right)^*\right)}{\left|\frac{\partial \vec{u_0}}{\partial z}\right|} a \text{ at } z = -H[y] \tag{1.99}$$

$$w_s c_1 + K_z \frac{\partial c_1}{\partial z} = 0 \text{ at } z = 0 \tag{1.100}$$

The first order sediment concentration c_1 results from the bed shear stress at first order, that results from the leading order and first order flow. Harmonic analysis of the right-hand side term in 1.99 shows that the sediment concentration can be written as a Fourier series which contains a residual component c_{10} and components that varies at the M_2 tidal frequency and its overtides

$$c_1 = c_{10} + c_{12} + \dots \tag{1.101}$$

Note that the term c_{12} arises as a consequence of the non-linearity of the bed shear stress.

Morphodynamic equilibrium condition

The morphodynamic equilibrium condition, up to $o[\varepsilon^2]$, requires that, for any location y,

$$\int_{-H}^{0} \left(< v_0 c_0 > + < v_1 c_0 > + < v_0 c_1 > - \frac{K_y}{V^* B^*} < \frac{\partial c_0}{\partial y} > \right) dz = 0 \quad (1.102)$$

Recalling that the velocity components consists of M_2, M_4 and residual components

$$v_0 = v_{02},\ v_1 = v_{10} + v_{12} \quad (1.103)$$

and the concentration can be written

$$(1.104)$$

$$c_0 = c_{00} + c_{04},\ c_1 = c_{10} + c_{12} \quad (1.105)$$

it follows that the only tidally average contributions at order ϵ^2 are

$$T_{M0} = \int_{-H}^{\eta} (< v_{10} c_{00} >)\ dz \quad (1.106)$$

$$T_{M2} = \int_{-H}^{\eta} (< v_{02} c_{12} >)\ dz \quad (1.107)$$

$$T_{\text{diff}} = \int_{-H}^{\eta} \left(-\frac{K_y}{V^* B^*} < \frac{\partial c_{00}}{\partial y} > \right) dz \quad (1.108)$$

Now equation 1.102 becomes

$$T_{M0} + T_{M2} + T_{\text{diff}} = 0 \text{ for all y} \quad (1.109)$$

Hence, the system is in morphodynamic equilibrium if the mean lateral sediment transport induced by the mean flow, T_{M0}, by the semi-diurnal flow u_{02}, T_{M2}, and by diffusion, T_{diff}, balance. Although the mean transport T_{M2} induced by tidal flow is usually ignored or modelled as turbulent diffusion, it can be quite important. Crucial for its importance is the phase difference between the lateral tidal velocity and the semi-diurnal component of the sediment concentration. The more these two quantities are in phase, the larger their contribution to the mean lateral sediment transport.

1.6 Analytical solution

The main interest of the present work is to determine the tidally average lateral sediment transport responsible for the sediment distribution across the estuary section. As discuss in section 1.5, the following constituents of flow and sediment concentration contribute to control sediment dynamics: the leading order tidal M_2 flow, $\vec{u}_{02}$; the first order residual flow, $\vec{u}_{10}$; the leading order residual sediment concentration, c_{00}; the semi-diurnal component of the first order sediment concentration, c_{12}.
A normal mode solution is considered by introducing the following expansion

$$\Psi_j = \text{Re}\left[\hat{\Psi}_j[x,y,z]e^{i\omega t}\right] \tag{1.110}$$

where $\Psi_j = \{u_j, v_j, w_j, \left(\frac{\partial \eta}{\partial x}\right)_j, \left(\frac{\partial \eta}{\partial y}\right)_j, c_j\}$ at each perturbation order j and the hat indicates coefficients that are functions only of spatial coordinates. Substituting this expansion into the leading and first order momentum and mass conservation equations yields a series of ordinary differential equations that allow the calculation of the coefficients $\hat{\Psi}_j$.

For a more easy interpretation of the analytical solutions and for their representation, in the following the equations are dimensional, as well as the figures.

The parameters used for all figures are those reported in section 1.9,if

not otherwise specified; these parameters are taken as reference values for a typical estuary (e.g., the James River - USA).

1.6.1 Constant eddy viscosity with no-slip condition

Hydrodynamics

In leading order, the spatial structure of the velocity is a function of the surface gradient

$$\hat{u}_{02} = \frac{ig}{\omega}\left(\frac{\partial\hat{\eta}}{\partial x}\right)_{02}\left(1-\frac{\cosh(\alpha z)}{\cosh(\alpha H)}\right) \tag{1.111}$$

$$\hat{v}_{02} = \frac{fg}{\omega^2}\left(\frac{\partial\hat{\eta}}{\partial x}\right)_{02}\left(1-\frac{\cosh(\alpha z)}{\cosh(\alpha H)}+\frac{i\omega}{2A_z}\left(z^2-H^2\right)\right)+ \\ +\frac{g}{2A_z}\left(\frac{\partial\hat{\eta}}{\partial y}\right)_{02}\left(z^2-H^2\right) \tag{1.112}$$

where $\alpha = \sqrt{\frac{i\omega}{A_z}}$.

The surface gradient $\left(\frac{\partial\hat{\eta}}{\partial x}\right)_{02}$ results from eq. 1.83 and $\left(\frac{\partial\hat{\eta}}{\partial y}\right)_{02}$ from the boundary condition 1.82.They read

$$\left(\frac{\partial\hat{\eta}}{\partial x}\right)_{02} = \frac{\omega U_T S}{ig}\left(\int_0^{B^*}\frac{1}{\alpha}(\alpha H-\tanh(\alpha H))dy\right)^{-1} \tag{1.113}$$

$$\left(\frac{\partial\hat{\eta}}{\partial y}\right)_{02} = \frac{if}{\omega}\left(\frac{\partial\hat{\eta}}{\partial x}\right)_{02}\left(3\frac{\alpha H-\tanh(\alpha H)}{(\alpha H)^3}-1\right) \tag{1.114}$$

Here the longitudinal surface gradient $\left(\frac{\partial\hat{\eta}}{\partial x}\right)_{02}$ is constant in the lateral direction. The lateral surface gradient $\left(\frac{\partial\hat{\eta}}{\partial y}\right)_{02}$ depends on the transverse coordinate y, i.e. on the bathymetry.

The vertical velocity coefficient $\hat{w_{02}}$ is obtained by integrating the conti-

nuity equation over depth and imposing the no-flux condition at the bed:

$$\hat{w}_{02} = \frac{1}{6A_z\omega^2}\left(6g\left(fA_z\left(\frac{\partial\hat{\eta}}{\partial x}\right)_{02}\left(\alpha^2 H(z+H)+\right.\right.\right.$$
$$-\operatorname{sech}(\alpha H)(\sinh(z\alpha)+\sinh(\alpha H))\tanh(\alpha H))+$$
$$\left.\left.\left.+H(z+H)\omega^2\left(\frac{\partial\hat{\eta}}{\partial y}\right)_{02}\right)\frac{\partial H}{\partial y}-g(z-2H)(z+H)^2\omega^2\frac{\partial}{\partial y}\left(\frac{\partial\hat{\eta}}{\partial y}\right)_{02}\right)\right. \tag{1.115}$$

Figure 1.2 shows a contour plots of the real part of the three component of the velocity. The figure also shows the tidally averaged suspended sediment concentration c_{00} in morphodynamic equilibrium.

At the first order each variable is expanded into a mean value ($\hat{\Psi}_{i0}$) and its tidal-harmonic components ($\hat{\Psi}_{i2}, \hat{\Psi}_{i4}, \dots$), namely

$$\Psi_i[x,y,z,t] = \hat{\Psi}_{i0}[x,y,z] + \hat{\Psi}_{i2}[x,y,z]e^{i\omega t} + \hat{\Psi}_{i4}[x,y,z]e^{i2\omega t} + ... \tag{1.116}$$

The contribution of the residual flow component $\hat{\Psi}_{i0}[x,y,z]$is obtained by tidally averaging equations 1.89-1.91. The solution reads

$$\hat{u}_{10} = -\frac{1}{A_z}\left(\frac{1}{6}\frac{g}{\rho_{ref}}\left(\frac{\partial\rho}{\partial x}\right)\left(z^3+H^3\right)-\frac{g}{2}\left(\frac{\partial\hat{\eta}}{\partial x}\right)_{10}\left(z^2-H^2\right)\right) \tag{1.117}$$

$$\hat{v}_{10} = -\frac{fg}{12A_z^2\rho_0}\left(\frac{1}{10}(z^5+H^5)+H^3(z^2-H^2)\right)\frac{\partial\rho}{\partial x}+$$
$$+\frac{fg}{4A_z^2}\left(\frac{1}{6}\left(z^4-H^4\right)-H^2\left(z^2-H^2\right)\right)\left(\frac{\partial\hat{\eta}}{\partial x}\right)_{10}+$$
$$-\frac{g}{6A_z\rho_0}(z^3+H^3)\frac{\partial\rho}{\partial y}+\frac{g}{2A_z}(z^2-H^2)\left(\frac{\partial\hat{\eta}}{\partial y}\right)_{10} \tag{1.118}$$

The longitudinal velocity is driven by the longitudinal tidally averaged density gradient (the gravitational circulation). The Coriolis deflecting the gravitational circulation is one of the contribution to the lateral tidally averaged velocity. Apart from this contributions, the tidally averaged lateral density

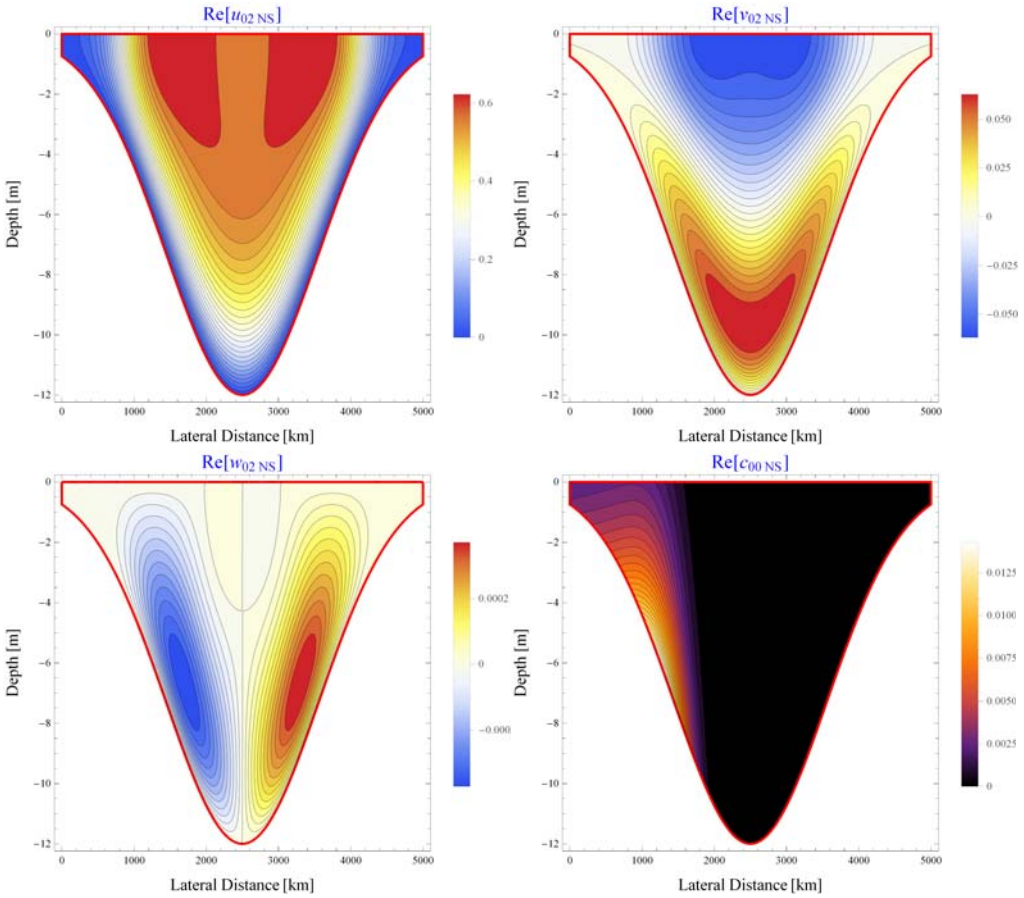

Figure 1.2: Model with no-slip (NS) boundary condition and constant eddy viscosity: contour plots of the three components of the leading order velocity u, v and w (real part) at max ebb and tidally averaged suspended sediment concentration c_{00}. The longitudinal component u is positive when directed sea-ward; the lateral component v is positive when directed towards the right bank; the vertical component w is positive if directed up-ward.

gradient contributes to the lateral mean velocity as well. The surface gradient is calculated by imposing the boundary conditions of equation 1.83 and 1.82, respectively; namely

$$\left(\frac{\partial\hat{\eta}}{\partial x}\right)_{10} = -\frac{3}{8}\frac{1}{\rho_{ref}}\frac{\int_0^{B^*} H^4\,dy}{\int_0^{B^*} H^3\,dy}\frac{\partial\rho}{\partial x} \tag{1.119}$$

$$\left(\frac{\partial\hat{\eta}}{\partial y}\right)_{10} = \frac{7}{48}\frac{fH^3}{A_z\rho_0}\frac{\partial\rho}{\partial x} - \frac{3}{8}\frac{H}{\rho_{ref}}\frac{\partial\rho}{\partial y} + \frac{2}{5}\frac{fH^2}{A_z}\left(\frac{\partial\hat{\eta}}{\partial x}\right)_{10} \tag{1.120}$$

The solution for the mean vertical velocity is obtained by integrating the continuity equation over depth and requiring that the bed is impermeable to the flow

$$\begin{aligned}\hat{w}_{10} = {} & \frac{fg}{24A_z^2\rho_0}(2H^2z^3 - 9H^4 - 7H^5)\frac{\partial H}{\partial y}\frac{\partial\rho}{\partial x} + \frac{g}{2A_z\rho_0}H^2(z+H)\frac{\partial H}{\partial y}\frac{\partial\rho}{\partial y} + \\ & + \frac{fg}{6A_z^2}H(z^3 - 5H^2z - 4H^3)\frac{\partial H}{\partial y}\left(\frac{\partial\hat{\eta}}{\partial x}\right)_{10} + \frac{g}{A_z}H(z+H)\frac{\partial H}{\partial y}\left(\frac{\partial\hat{\eta}}{\partial y}\right)_{10} + \\ & + \frac{g}{6A_z}(z+H)^2(z-2H)\frac{\partial}{\partial y}\left(\frac{\partial\hat{\eta}}{\partial y}\right)_{10}\end{aligned} \tag{1.121}$$

The three component of the residual first order velocity are shown in figure 1.3.

Sediment concentration

The component of the suspended sediment concentration at the leading order is the tidally averaged one. Integrating the tidally averaged equation 1.85 over the vertical coordinate, imposing the condition of vanishing sediment flux through the surface, gives that

$$K_z\frac{\partial c_{00}}{\partial z} + \omega_s c_{00} = 0 \tag{1.122}$$

The tidally averaged suspended sediment concentration is thus determined by the balance between the verticall diffusion and settling of sediment. The

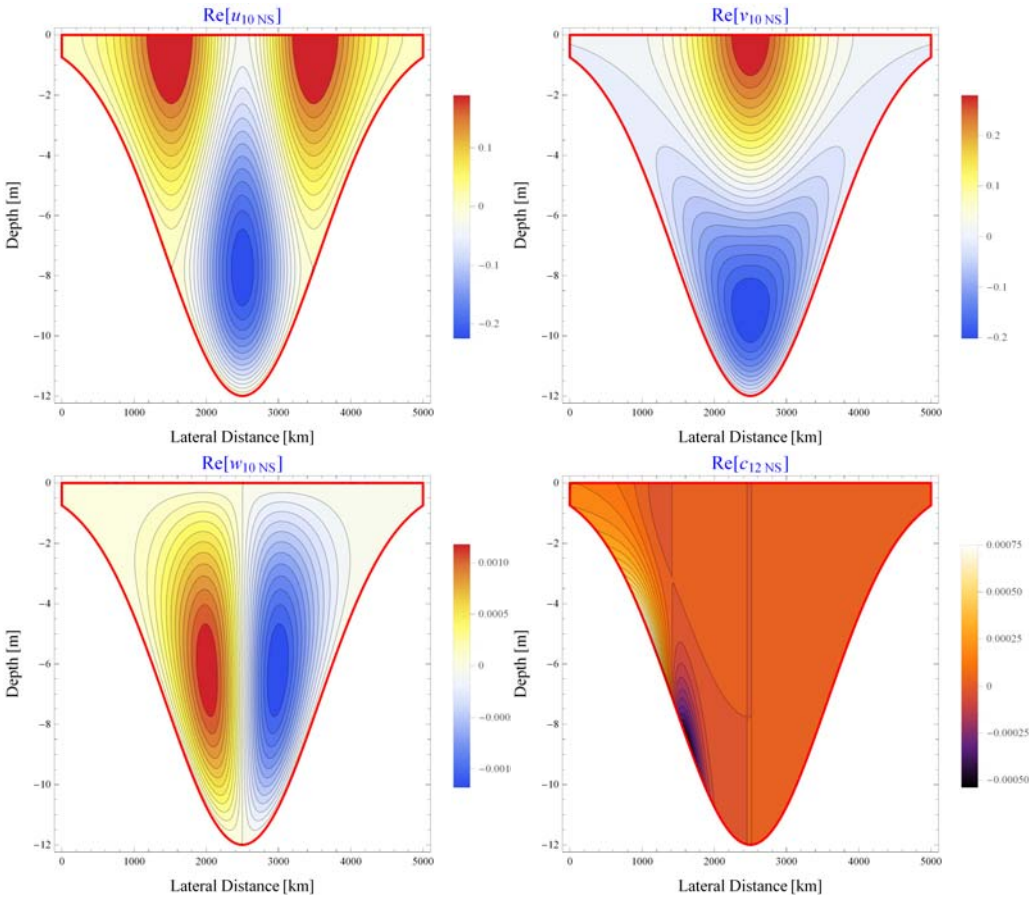

Figure 1.3: Model with no-slip (NS) boundary condition and constant eddy viscosity: contour plots of the three components of the first order residual velocity and the suspended sediment concentration c_{12}. The longitudinal component u is positive when directed sea-ward; the lateral component v is positive when directed towards the right bank; the vertical component w is positive if directed up-ward.

boundary condition have their default values at the bed, requires that

$$-K_z \frac{\partial c_{00}}{\partial z} = \omega_s \left|\tau_b\right|_{00} a[y] \text{ at } z = -H[y] \tag{1.123}$$

where τ_{b00} denotes the mean component of the zeroth order bed shear stress

$$\left|\tau_b\right|_{00}[x,y] = A_z \rho_0 \left|\frac{\partial \vec{u_{02}}}{\partial z}\right| \text{at} z = -H[y] \tag{1.124}$$

The solution of the boundary value problem provided by equations 1.122-1.123 is given by

$$c_{00}[x,y,z] = \left|\tau_b\right|_{00} e^{-\frac{\omega_s}{K_z}(z+H)} a[y] \frac{\rho_s}{(\rho_s - \rho_{ref}) g d_s} \tag{1.125}$$

where $\frac{K_z}{\omega_s}$ is an e-folding length scale controlling the decay of suspended sediment concentration in the water column above the bottom. The residual suspended sediment concentration is controlled by the erosion coefficient (a) multiplied by the mean component of the bed shear stress.

The first order solution for the suspended sediment concentration is obtained expanding the concentration into its tidal-harmonic components. It was demonstrated that in the morphodynamic equilibrium condition the only concentration component that is important up to $O[\varepsilon^2]$ is $\hat{c}_{12}$, because of the correlation with the M_2 component of transverse velocity.

The complex coefficient $\hat{c}_{12}[x,y,z]$ is given by

$$\hat{c}_{12}[x,y,z] = -\frac{e^{-\frac{(z+H)\omega_s + (z-H)R}{2K_v}} \omega_s \left(\left(-1 + e^{\frac{zR}{K_v}}\right)\omega_s - \left(1 + e^{\frac{zR}{K_v}}\right) R\right)}{\left(-1 + e^{\frac{HR}{K_v}}\right)\omega_s^2 + 2i\left(-1 + e^{\frac{HR}{K_v}}\right) K_v \omega_T + \left(1 + e^{\frac{HR}{K_v}}\right)\omega_s R} \cdot \frac{\rho_s \left|\hat{\tau}_b\right|_{12}}{(\rho_s - \rho_{ref})\, g d_s} a[y] \tag{1.126}$$

where $R = \sqrt{\omega_s^2 + 4iK_v\omega_T}$ and $\left|\hat{\tau}_b\right|_{12}$ is the first order semi-diurnal compo-

nent of the absolute value of the bed shear stress:

$$|\hat{\tau}_b|_{12}[x,y] = \frac{A_z\rho_0}{2}\frac{\left(\frac{\partial\hat{\vec{u}}_{02}}{\partial z}\cdot\left(\frac{\partial\hat{\vec{u}}_{10}}{\partial z}\right)^* + \frac{\partial\hat{\vec{u}}_{10}}{\partial z}\cdot\left(\frac{\partial\hat{\vec{u}}_{02}}{\partial z}\right)^*\right)}{\left|\frac{\partial\vec{u_{02}}}{\partial z}\right|} \text{ at } z=-H[y] \quad (1.127)$$

Now it is possible to calculate the erosion coefficient by imposing the morphodynamic equation 1.102, which leads to a first order differential equation

$$I_1\frac{da}{dy} + I_2 a = 0 \quad (1.128)$$

where I_1 and I_2 are known integrals given by

$$I_1[y] = \int_{-H}^{0} -K_y\frac{c_{00}}{a[y]}dz \quad (1.129)$$

$$I_2[y] = \int_{-H}^{0}\left(\hat{v}_{10}\frac{\hat{c}_{00}}{a[y]} + \hat{v}_{02}\frac{\hat{c}^*_{12}}{a[y]} - K_y\frac{\partial\left(\frac{\hat{c}_{00}}{a[y]}\right)}{\partial y}\right)dz \quad (1.130)$$

The erosion coefficient reads

$$a[y] = a_0 e^{-\int_0^y I_2/I_1\,dy} \quad (1.131)$$

where the integration constant a_0 is obtained by imposing the boundary condition 1.75; this yields

$$a_0 = \frac{a_*}{\frac{1}{B^*}\int_0^{B^*} e^{-\int_0^y \frac{I_2}{I_1}dy}\,dy} \quad (1.132)$$

1.6.2 Constant eddy viscosity with partial-slip condition

Let us now consider the flow field solution and the concentration distribution resulting from the assumption of a partial-slip boundary condition at the bed.

Hydrodynamics

As in the no-slip case, the horizontal tidal velocity coefficients are solved as function of surface gradient by imposing the boundary conditions 1.19. They read

$$\hat{u}_{02} = \frac{ig}{\omega_T}\left(1 - \frac{\cosh(\alpha z)}{\cosh(\alpha H) + \frac{\alpha A_z}{s}\sinh(\alpha H)}\right)\left(\hat{\frac{\partial\eta}{\partial x}}\right)_{02} \tag{1.133}$$

$$\hat{v}_{02} = \frac{fg}{\omega_T^2}\left(1 - \frac{\cosh(\alpha z)}{\cosh(\alpha H) + \frac{\alpha A_z}{s}\sinh(\alpha H)} + \frac{\alpha^2}{2}(z^2 - H^2) - \frac{\alpha^2 A_z}{s}H\right)\left(\hat{\frac{\partial\eta}{\partial x}}\right)_{02} + + \frac{g}{2A_z}\left(z^2 - H^2 - \frac{2A_z}{s}H\right)\left(\hat{\frac{\partial\eta}{\partial y}}\right)_{02} \tag{1.134}$$

where $\alpha = \sqrt{i\omega_T/A_z}$. The water surface gradient is estimated through the boundary conditions 1.65 and 1.66

$$\left(\hat{\frac{\partial\eta}{\partial x}}\right)_{02} = \frac{\omega_T U_T S}{ig}\left(\int_0^{B^*}\frac{1}{\alpha}(\alpha H - \frac{\sinh(\alpha H)}{\cosh(\alpha H) + \frac{\alpha A_z}{s}\sinh(\alpha H)})dy\right)^{-1} \tag{1.135}$$

$$\left(\hat{\frac{\partial\eta}{\partial y}}\right)_{02} = \frac{fA_z}{\alpha\omega_T^2}\left(-\frac{3\sinh(\alpha H)}{H^2(H + 3\frac{A_z}{s})(\cosh(\alpha H) + \frac{\alpha A_z}{s}\sinh(\alpha H))} + + \frac{3\alpha}{H(H + 3\frac{Az}{s})} - \alpha^3\right)\left(\hat{\frac{\partial\eta}{\partial x}}\right)_{02} \tag{1.136}$$

It immediately appears that the longitudinal component of the surface gradient $\left(\hat{\frac{\partial\eta}{\partial x}}\right)_{02}$ is constant; while the transverse component $\left(\hat{\frac{\partial\eta}{\partial y}}\right)_{02}$ depends on only y-coordinate through the bathymetry.

The vertical velocity coefficient is obtained by integrating the continuity equation over the depth and applying the condition of bottom imperme-

ability

$$\hat{w}_{02} = \frac{gf}{\omega_T^2}\left(z\alpha^2 H + \left(-\sinh(z\alpha)\sinh(\alpha H) + z\alpha^3\left(\frac{A_z}{s}\right)^2\sinh(2\alpha H) + \right.\right.$$
$$+\frac{\alpha A_z}{s}\cosh(\alpha H)(z\alpha\cosh(\alpha H) - \sinh(z\alpha)) + z\alpha^4\left(\frac{A_z}{s}\right)^3\sinh(\alpha H)^2\Bigg)\cdot$$
$$\left.\cdot\left(\cosh(\alpha H) + \frac{\alpha A_z}{s}\sinh(\alpha H)\right)^{-2}\right)\frac{\partial H}{\partial y}\left(\frac{\partial\hat{\eta}}{\partial x}\right)_{02} +$$
$$+\frac{gz}{A_z}\left(\frac{A_z}{s} + H\right)\frac{\partial H}{\partial y}\left(\frac{\partial\hat{\eta}}{\partial y}\right)_{02} +$$
$$+\frac{g}{6A_z}\left(3zH\left(H + \frac{2A_z}{s}\right) - z^3\right)\frac{\partial}{\partial y}\left(\frac{\partial\hat{\eta}}{\partial y}\right)_{02} \tag{1.137}$$

Figures 1.4 show a contour plots of the real part of the three component of the velocity. Figure 1.4 also reporteds the real part of the tidally averaged suspended sediment concentration c_{00}. The first order of approximation is processed as in section 1.6.1. The horizontal mean flow (residual flow) is obtained as a function of mean surface gradient by solving the mean part of the first order momentum equation and the relative boundary conditions. In practice, each variable is expanded into its tidal-harmonic components

$$\Psi_i[x,y,z,t] = \hat{\Psi}_{i0}[x,y,z] + \hat{\Psi}_{i2}[x,y,z]e^{i\omega_T t} + \hat{\Psi}_{i4}[x,y,z]e^{i2\omega_T t} + \dots \tag{1.138}$$

with $\hat{\Psi}_{i0}$ the time-independent term related to residual flow, obtained by solving the first order equations average over a tidal period. The horizontal

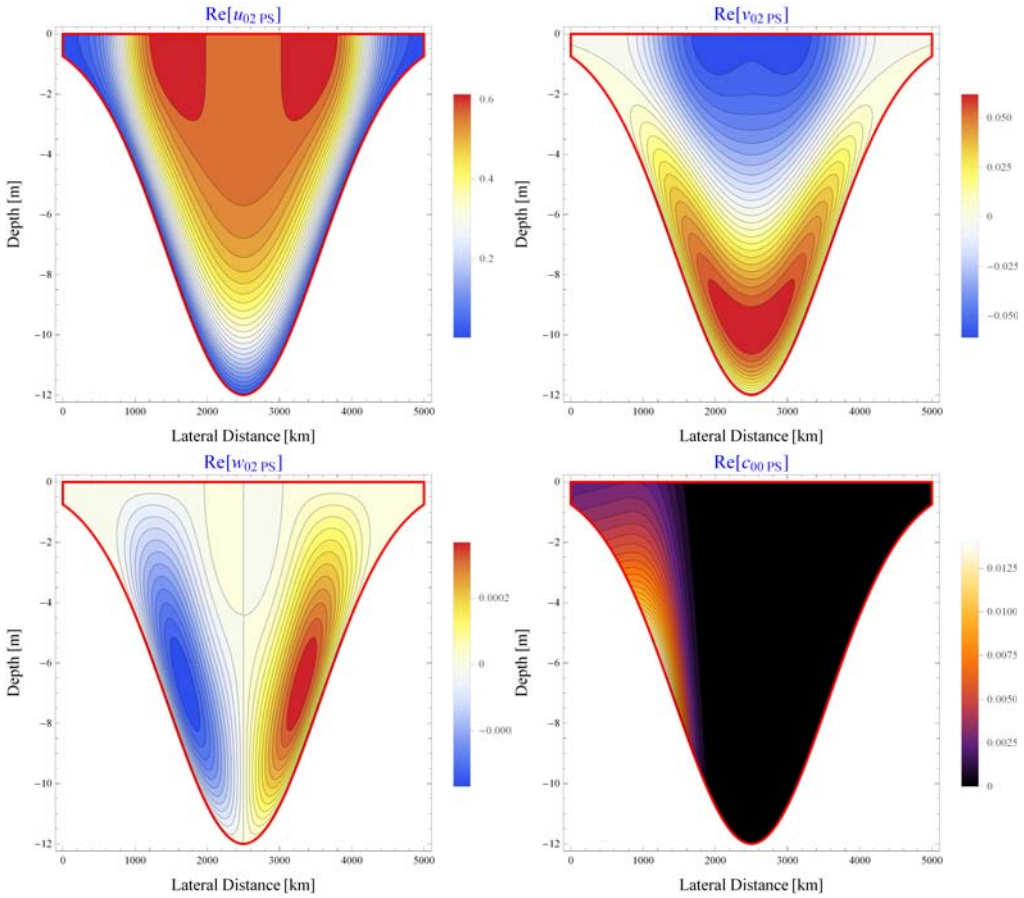

Figure 1.4: Model with partial-slip (PS) boundary condition and constant eddy viscosity: contour plots of the three components of the leading order velocity u, v and w (real part) and tidally averaged suspended sediment concentration c_{00}. The longitudinal component u is positive when directed sea-ward; the lateral component v is positive when directed towards the right bank; the vertical component w is positive if directed up-ward.

velocity read

$$\hat{u}_{10} = -\frac{g}{6A_z\rho_{ref}}\left(z^3 + H^3 + 3\frac{A_z}{s}H^2\right)\frac{\partial\rho}{\partial x} + \frac{g}{2A_z}\left(z^2 - H^2 - 2\frac{A_z}{s}H\right)\left(\frac{\partial\hat{\eta}}{\partial x}\right)_{10} \tag{1.139}$$

$$\begin{aligned}\hat{v}_{10} = &-\frac{fg}{120A_z^2\rho_0}\left(z^5 + 10z^2H^3 - 9H^5 - 15\frac{A_z}{s}H^4\right)\frac{\partial\rho}{\partial x} + \\ &+ \frac{fg}{24A_z^2}\left(z^4 - 6z^2H^2 + 5H^4 + 8\frac{A_z}{s}H^3\right)\left(\frac{\partial\hat{\eta}}{\partial x}\right)_{10} + \\ &- \frac{g}{6A_z\rho_0}(z^3 + H^3 + 3\frac{A_z}{s})\frac{\partial\rho}{\partial y} + \frac{g}{2A_z}(z^2 - H^2 - 2\frac{A_z}{s}H)\left(\frac{\partial\hat{\eta}}{\partial y}\right)_{10}\end{aligned} \tag{1.140}$$

Surface gradient is calculated by using boundary conditions; it reads

$$\left(\frac{\partial\hat{\eta}}{\partial x}\right)_{10} = -\frac{3}{8\rho_0}\frac{\int_0^{B^*} H^3(H - 4\frac{A_z}{s})\frac{\partial\rho}{\partial x}\,dy}{\int_0^{B^*} H^2(H + 3\frac{A_z}{s})\,dy} \tag{1.141}$$

$$\left(\frac{\partial\hat{\eta}}{\partial y}\right)_{10} = \frac{fH^3}{48A_z\rho_0}\frac{7H + 18\frac{A_z}{s}}{H + 3\frac{A_z}{s}}\frac{\partial\rho}{\partial x} - \frac{3H}{8\rho_0}\frac{H + 4\frac{A_z}{s}}{H + 3\frac{A_z}{s}}\frac{\partial\rho}{\partial y} + \frac{fH^2}{5A_z}\frac{2H + 5\frac{A_z}{s}}{H + 3\frac{A_z}{s}}\left(\frac{\partial\hat{\eta}}{\partial x}\right)_{10} \tag{1.142}$$

The mean vertical velocity is determined by integrating mean continuity equation over the depth and applying bottom impermeability

$$\begin{aligned}\hat{w}_{10} = &\frac{fgzH^2}{24A_z^2\rho_0}(2z^2 - 9H^2 - 12H\frac{A_z}{s})\frac{\partial H}{\partial y}\frac{\partial\rho}{\partial x} + \frac{gzH}{2A_z\rho_0}(H + 2\frac{A_z}{s})\frac{\partial H}{\partial y}\frac{\partial\rho}{\partial y} + \\ &+ \frac{fgzH}{6A_z^2}(z^2 - 5H^2 - 6H\frac{A_z}{s})\frac{\partial H}{\partial y}\left(\frac{\partial\hat{\eta}}{\partial x}\right)_{10} + \frac{gz}{A_z}(H + \frac{A_z}{s})\frac{\partial H}{\partial y}\left(\frac{\partial\hat{\eta}}{\partial y}\right)_{10} + \\ &- \frac{gz}{6A_z}(z^2 - 3H^2 - 6H\frac{A_z}{s})\frac{\partial}{\partial y}\left(\frac{\partial\hat{\eta}}{\partial y}\right)_{10}\end{aligned} \tag{1.143}$$

A snapshot of the three component of the residual first order velocity is shown as contour plots in figure 1.5. The values of the various parameters are reported in section 1.9.

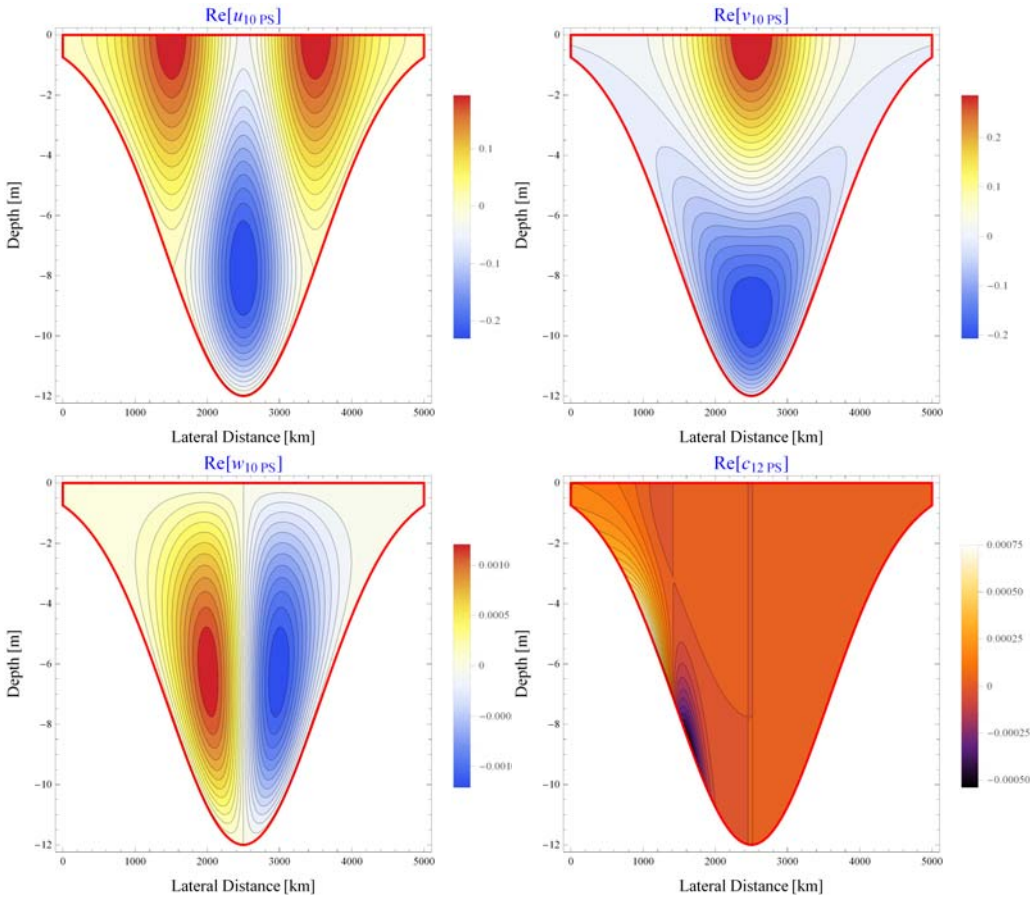

Figure 1.5: Model with partial-slip (PS) boundary condition and constant eddy viscosity: contour plots of the three components of the first order residual velocity and the suspended sediment concentration c_{12}. The longitudinal component u is positive when directed sea-ward; the lateral component v is positive when directed towards the right bank; the vertical component w is positive if directed up-ward.

Sediment concentration

The structure of the mass balance equation is similar to that obtained by considering the no-slip boundary condition. However, owing to the different flow field arising form the imposition of a partial-slip condition, bed shear stress now read

$$|\tau_b|_{00}[x,y] = s\rho_0\sqrt{\text{Abs}\left[\frac{\partial\hat{u}_{02}}{\partial z}\right]^2 + \text{Abs}\left[\frac{\partial\hat{v}_{02}}{\partial z}\right]^2 + \text{Abs}\left[\frac{\partial\hat{w}_{02}}{\partial z}\right]^2}\,\text{at}\,z = -H[y] \tag{1.144}$$

$$|\tau_b|_{12}[x,y] = \frac{s\rho_0}{2}\frac{\left(\frac{\partial\hat{\vec{u}}_{02}}{\partial z}\cdot\left(\frac{\partial\hat{\vec{u}}_{10}}{\partial z}\right)^* e^{i\omega_T t} + \frac{\partial\hat{\vec{u}}_{10}}{\partial z}\cdot\left(\frac{\partial\hat{\vec{u}}_{02}}{\partial z}\right)^* e^{-i\omega_T t}\right)}{\sqrt{\text{Abs}\left[\frac{\partial\hat{u}_{02}}{\partial z}\right]^2 + \text{Abs}\left[\frac{\partial\hat{v}_{02}}{\partial z}\right]^2 + \text{Abs}\left[\frac{\partial\hat{w}_{02}}{\partial z}\right]^2}}\ \text{at}\ z = -H[y] \tag{1.145}$$

1.6.3 Parabolic eddy viscosity profile with no-slip condition

Let us finally consider the case of a parabolic eddy viscosity profile. The procedure follow to derive the leading and first order of the flow field and of the sediment concentration are similar to that describe in section 1.6.1.

Now the solution are very long analytical expressions function of hypergeometric functions. In the following are presented only the results by their figures.

1.7 Comparison

It has been made a comparison for the three different boundary conditions. In figure 1.8 various vertical profile of the velocity u-component are compared for different vertical section in the cross-section, from the side bank to the centre of the estuary. The difference between the classical condition and the partial-slip is minimal, and it decreases moving toward the deeper

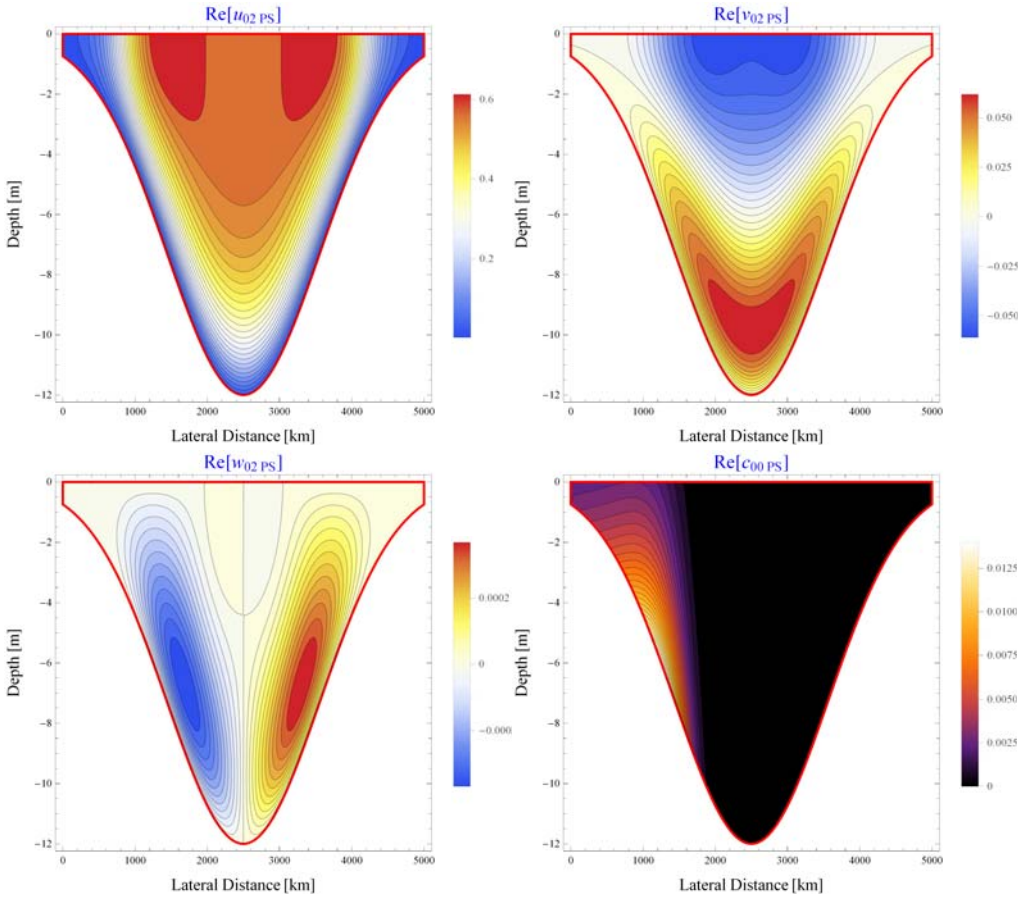

Figure 1.6: Model with no-slip boundary condition and parabolic eddy viscosity (PEV): contour plots of the three components of the leading order velocity u, v and w(real part) and tidally averaged suspended sediment concentration c_{00}. The longitudinal component u is positive when directed sea-ward; the lateral component v is positive when directed towards the right bank; the vertical component w is positive if directed up-ward.

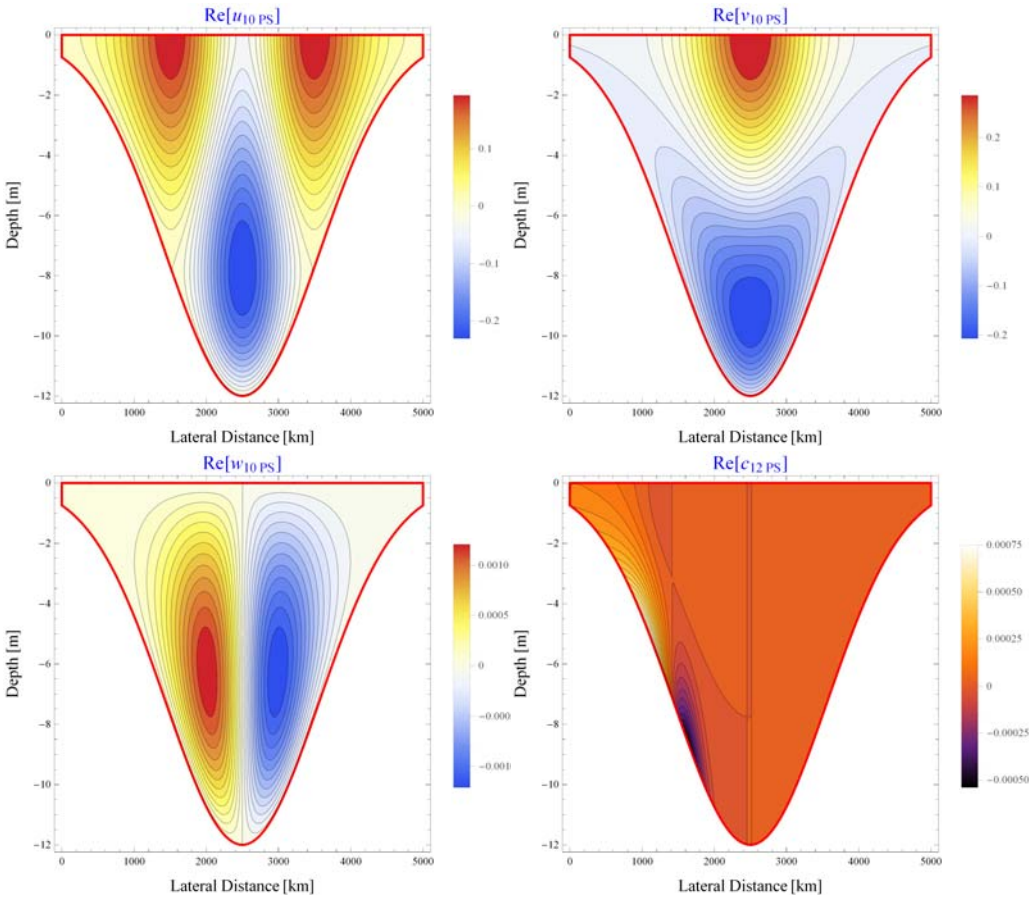

Figure 1.7: Model with no-slip boundary condition and parabolic eddy viscosity (PEV): contour plots of the three components of the first order residual velocity and the suspended sediment concentration c_{12}. The longitudinal component u is positive when directed sea-ward; the lateral component v is positive when directed towards the right bank; the vertical component w is positive if directed up-ward.

part of the estuary. Instead the difference with the parabolic eddy viscosity is impressive. The gradient of the velocity is very high in the boundary layer; after a small portion of the total depth, the velocity becomes almost constant. To maintain the same discharge in the cross-section, the maximum velocity is smaller than the case of constant viscosity.

Similarly, in figure 1.9 various vertical profile of the velocity v-component are compared for the same different vertical section. Also in this case the partial-slip condition is quite similar to the classical solution derived with constant eddy viscosity and no-slip condition. The solution with parabolic eddy viscosity again shows high gradient in the bed boundary layer and globally it is very different form the classical one.

1.8 Summary and conclusions

It has been developed a model for the investigation of the influence of boundary condition at the bed, on both hydrodynamic and suspended sediment distribution in cross section of tidal estuary. The main contribution is the analysis of the effects of three boundary condition at the bed: no-slip condition with constant and parabolic eddy viscosity; partial-slip with constant eddy viscosity.

The model allows analytical solution of the water motion and sediment transport for the three considered boundary conditions.

The model is analytical and so it allows highly accurate calculation and high space resolution. These are important aspects when dealing with cross-section analysis and mud reach search. The model is built-up with implicit dependency on the different forcing and parameters, they all appear as function in the results. Even if in this way it is not optimised for fast calculation, it is quite fast and this easily permits sensitivity analysis on the most relevant factors that affect the model. So the model is extremely flexible for wide variation of forcing and parameters.

Considering constant eddy viscosity, the results show that the no-slip and

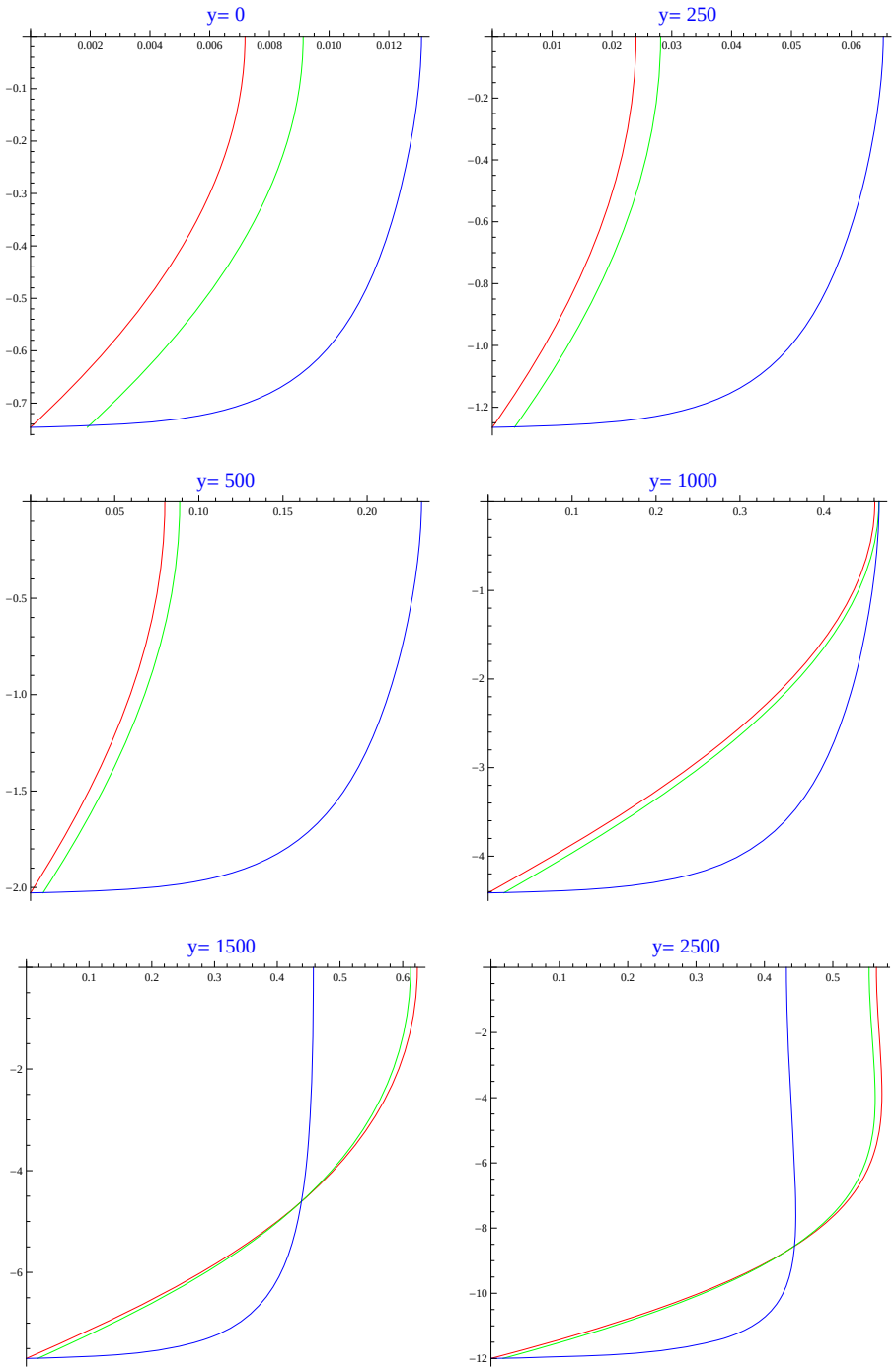

Figure 1.8: Comparison profiles for of the u-component of the velocity for different vertical section in the cross-section: in red the solution with no-slip and constant eddy viscosity; in green the case of partial-slip and constant eddy viscosity; in blue the profile for the case of no-slip and parabolic eddy viscosity.

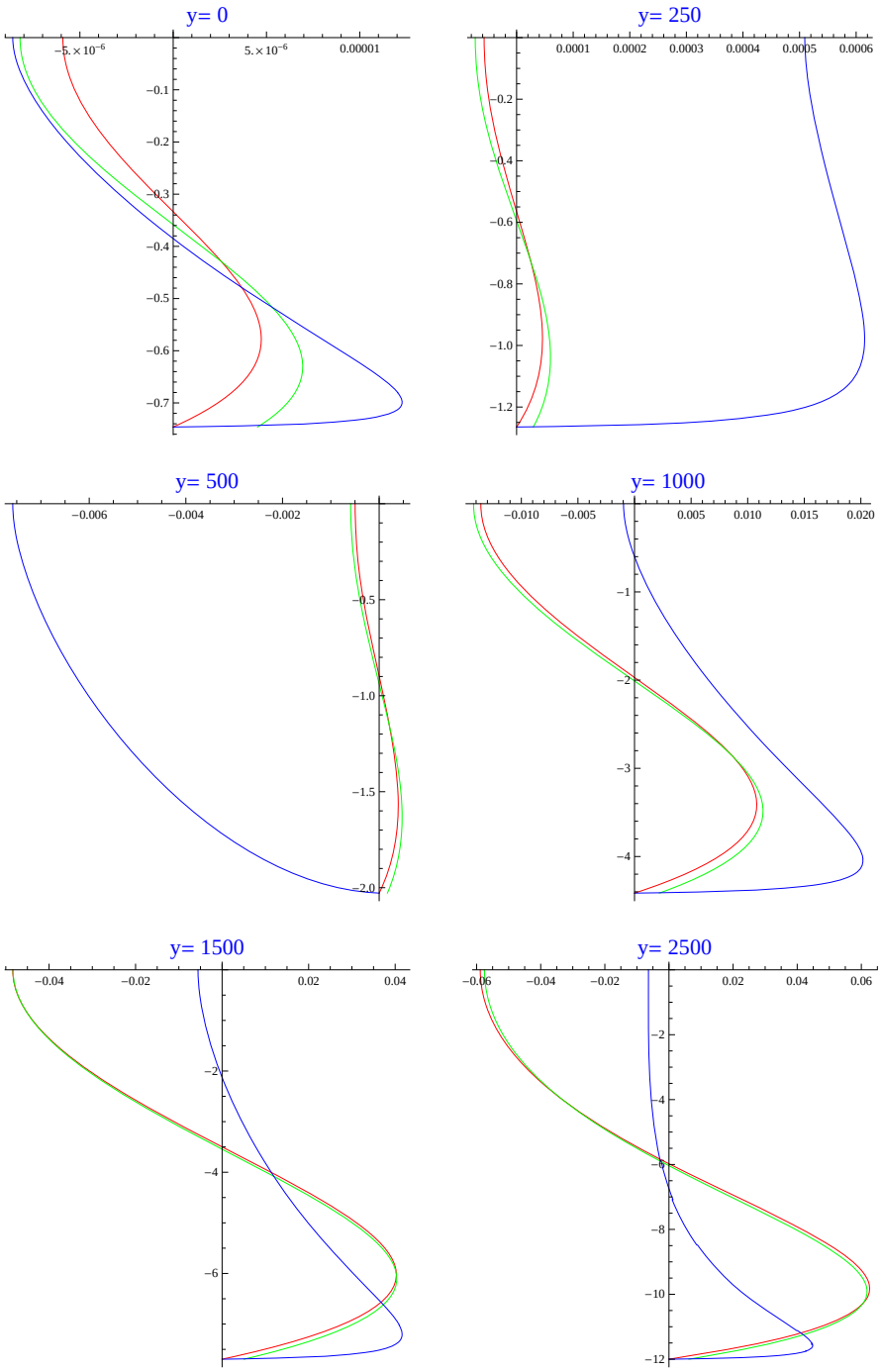

Figure 1.9: Comparison profiles for of the v-component of the velocity for different vertical section in the cross-section: in red the solution with no-slip and constant eddy viscosity; in green the case of partial-slip and constant eddy viscosity; in blue the profile for the case of no-slip and parabolic eddy viscosity.

partial slip boundary condition give very similar solutions. Considering the no-slip condition, the use of a parabolic eddy viscosity give a very different solution respect to the use of the classical constant eddy viscosity. The velocity profiles derived with parabolic eddy viscosity show high gradient in the first meter from the bed. In fact, with the parabolic eddy viscosity it is possible to resolved the boundary layer at the bed, whereas with the classical solution it is not possible.

It remain to better compared and understand the effect of parabolic eddy viscosity to the sediment concentration distribution and to compared the solution with field data. In this way it will be possible to verify if effectively the parabolic eddy viscosity is a real improvement to the modelling of hydrodynamics and sediment distribution in cross-section.

1.9 Parameters and constants

Typical estuary geometry and sediment characteristics

$B^* \sim 5\ km,$ estuary width

$L \sim 1\ km,$ length of the investigated reach

$H_{\min} \sim 1\ m,$ cross-section minimum depth

$H_{\max} \sim 12\ m,$ cross-section maximum depth

$H_0 \sim 3\ m,$ cross-section mean depth

$C_m \sim 10 - 100\ mg/l,$ mean sediment concentration

$d_s \sim 20\ \mu$m, sediment grain size

$a_* \sim 4 \times 10^{-6},$ reference erosion coefficient

$w_s \sim 1\ mm/s,$ settling velocity

$\rho_s \sim 2650\ kgm^{-3},$ sediment density

$\Delta\rho \sim 2\ kgm^{-3},$ bed to surface density difference

Typical features of the tide forcing and the resulting mean flow (order of magnitude

$\omega_T = 1.4 \times 10^{-4}\ s^{-1},$ M_2-tide angular frequency

$U_T \sim 1\ m/s,$ cross-sectionally averaged tidal velocity amplitude

$U_D \sim 0.1\ m,$ mean flow induced by longitudinal density gradient

$V^* \sim 0.1\ m,$ typical velocity caused by lateral density gradient and Coriolis force

$U_R \sim 0.01 - 0.001\ m,$ typical velocity induced by river discharge

$\frac{\partial \rho}{\partial x} \sim 0.5 \times 10^{-3}\ kg/m^{-4},$ longitudinal density gradient

$\frac{\partial \rho}{\partial y} \sim 1 \times 10^{-3}\ kg/m^{-4},$ lateral density gradient

$K_v \sim 0.009\ m^2 s^{-1},$ vertical eddy diffusivity coefficient

$K_y = 5\ m^2 s^{-1},$ lateral eddy diffusivity coefficient

Eddy viscosity

$R \sim 0.01$

$\delta \sim 0.5$

$Ri \sim$

$A_0 \sim$

Constants

$g = 9.8\ ms^{-2},$ gravitational acceleration

$f = 10^{-4}\ s^{-1},$ Coriolis parameter

$\rho_{ref} = 1020\ kgm^{-3},$ reference density

Part II

Wind wave erosion

Chapter 2

Statistical evaluation of wind characteristics and wind energy density in the Lagoon of Venice, Italy

2.1 Abstract

The present study characterizes the sea-surface wind energy potential in view of its implications for modelling salt-marsh bank retreat in the Venice Lagoon (North-Eastern Italy).

A wind velocity/direction dataset of 11 years is analysed in terms of yearly, seasonal, monthly and hourly distributions of the wind field. Autocorrelation and wind event lengths are also analysed to better characterize wind events. The analysis is made by use of wind rose plots and wind probability density function.

It is found that wind climate inside the lagoon is weaker (yearly mean speed 3.8±2.7 and 3.3±2.2 m/s for Southern and Northern part, respectively) than over the sea (yearly mean speed 4.8 ± 3.6 m/s). The prevailing wind direction is North-East, and the second dominant direction is from South-

East, the latter mainly connected to land-sea breeze. In the last 10 years there was an anticlockwise rotation of the wind direction by about 22° in the two prevailing wind directions.

Wind velocity is highest between September and April, December being the windiest month. Land-sea breeze appears in February, it intensifies until March , to decrease in August and vanish in November.

Hourly analyses highlight that high wind conditions generally happen between 8 pm to 8 am in the open sea, and between 12 pm and 8 am within the lagoon; there is a maximum probability of low wind around 1 pm in the open sea, while inside the lagoon there are two minima around 11 am and 8 pm.

Autocorrelation analysis indicates that wind is a highly autocorrelated phenomenon: wind autocorrelation falls below 0.5 only after 7 to 8 hours for the Northern and Southern lagoon, respectively, and after at least 10 hours for the nearby open sea.

2.2 Introduction

Many studies related to wind characteristics have been made in recent years worldwide. This is partially due to increased interest in alternative energy resources; indeed, the available literature is most frequently concerned, more or less explicitly, with wind power modelling for turbine installation. Nevertheless, modelling the sea-surface wind field is of primary importance in a number of fields connected to meteorology, oceanography and climatology. Some of these investigations concern wind field measurements by remote sensing (e.g., Meissner et al. 2001 [12]; Canestrelli et al., 2003 [13]; Monahan, 2006 [14]), estimates of airsea exchanges (e.g., Isemer and Hasse 1991 [15]; Wanninkhof 1992 [16]; Wanninkhof and McGillis 1999 [17]), wind induced sea currents (e.g., Wu and Tsanis, 1995 [18]; Carniel et al., 2009 [19]; Burchard, 2009 [20]) and wind-waves (e.g., Yang et al., 2013 [21]; Johnson, 1998 [22]), but the list could indeed be much longer.

An active field of research connected with the characterization of wind speed distribution is the study of wind-wave erosion in estuaries. Generally, these studies focus on wind-wave generation and evolution (e.g., Carniello et al., 2011 [23]; Fagherazzi et al., 2009 [24]; Jouon et al., 2009 [25]; Moller et al., 1999 [26]), wave impact on salt-marshes and tidal flats (e.g., Tonelli, et al., 2010 [27]; Fagherazzi et al., 2007 [24]; Mariotti and Fagherazzi, 2010 [28]; Carniello et al., 2010 [29]; Marani et al., 2011 [30]) or the increase in sediment re-suspension (e.g., Chao et al., 2008 [31]; Kessarkar et al., 2009 [32]; Talke and Stacey, 2008 [33]).

The present work is concerned with the topic of marsh lateral erosion and it focuses on the sea-surface wind field characterization. For a morphological study of lagoon evolution, it is of primary importance to statistically characterize the wind field to provide crucial input for wind-wave erosion modelling. In fact, an important variable in wind-wave generation models (and consequently in erosion models) is the correct representation of the wind field and, in particular, of the wind energy power. To correctly evaluate the wave energy generated in a shallow water environment, it is necessary to have a detailed knowledge of various statistical characteristics of the wind field. For a selected site, this is made by investigating wind characteristics, such as speed, direction, duration, etc. through appropriate probability distribution functions (PDFs).

There are several works that deal with the frequency distribution of wind speed, and several PDFs have been proposed (see Carta et al, 2009 [34] and Morgan et al., 2011 [35] for a review). In general, the Weibull PDF is widely used to estimate a site's probability distribution of wind speed and wind power density ([34]). However, it has been noted that the Weibull distribution may not perform well in all cases and that it is generally not appropriate for both low and high wind speed (e.g., Chang, 2011 [36]; Zhou et al., 2010 [37]; Sarkar et al., 2011 [38]). The wind speed probability distribution is greatly dependent on the local morphology and climate conditions; for these reasons, it is important to identify appropriate site-dependent PDFs.

To analyse wind characteristics in the Venice lagoon, we use a dataset of 11 years of wind speed data (taken with a frequency of 5 minutes). The study area is described in section 2.3.1; the sea surface wind dataset is outlined in section 2.3.2. Wind rose and probability plots are briefly described in sections 2.3.3 and 2.3.4. A review of the properties of the used probability distribution functions is presented in section 2.3.5; whereas parameter estimation methods and accuracy judgement criteria are introduced in section 2.3.6 and 2.3.7. Wind power density definition and equations are written in section 2.3.8. A discussion of the observed statistics of the sea surface wind speeds is presented in section 2.4.1, while the results of the power density analysis are reported in section 2.4.2. Finally, summary and conclusions are given in section 2.5.

2.3 Materials and methods

2.3.1 Study area

The lagoon of Venice (Italy) is located in the Northern Adriatic Sea (Italy) and is the largest lagoon in Italy and a protected Ramsar site. It is a wide shallow basin with an area of about 550 km^2, roughly 80% of which is covered by water. The lagoon is also characterized by the presence of small islands (about 5% of the total surface) and wide salt marshes and tidal flats (about 10% of the total surface).

Dominant winds are the *Bora*, a North-Easterly wind, and the *Scirocco*, blowing from South-East.

2.3.2 Data

The wind observation dataset is provided by Istituzione Centro Previsioni e Segnalazioni Maree (ICPSM; Center for Tidal Level Forecast and Signalling) of the Venice Municipality. We consider three stations: an offshore oceanographic platform ("Piattaforma Aqua Alta" of CNR-ISMar, hereafter referred to as PAA), representative of the wind field in the open sea (15 km

Figure 2.1: Map of the Venice Lagoon with the location of the measuring stations: PAA - Piattaforma Aqua Alta, SAL - Laguna Nord Saline, CHI - Chioggia Porto

station	latitude	longitude	height [m]	date interval
PAA	45°18'51" N	12°30'30" E	15	01/01/2000-31/12/2011
SAL	45°29'44" N	12°28'19" E	9	01/01/2000-31/12/2011
CHI	45°13'57" N	12°16'50" E	9	01/01/2004-31/12/2011

Table 2.1: List of ICPSM stations with geographical co-ordinates, anemometer height above mean sea level, date range.

offshore), a station representative of the wind field in the Northern part of the Venice lagoon ("Laguna Nord Saline" of ICPSM, hereafter SAL) and one representative of the Southern part of the Venice lagoon ("Chioggia Porto" of ICPSM, hereafter CHI). The station positions are presented in Fig. 2.1, while station characteristics and time interval of available data are reported in Tab. 2.1. To be notice wind gust data at SAL station start only form 01/01/2009.

Each station is equipped with the same instruments: a floating hydrometer (SIAP ID7877) for tidal level measurements and a cup anemometer (SIAP VT0705B) for measurements of horizontal wind speed and wind direction. Measurement procedures, data sampling and data quality validation are identical for each station.

The anemometer characteristics for wind speed measurements are, as

specified in the instrument data-sheet: range 0-50 m/s; resolution 0.1 m/s; accuracy 0.5 m/s with speed less than 10 m/s, 5% otherwise. The anemometer characteristics for wind direction measurements are: range 0°-360°; resolution 2°; accuracy 3°.

Wind observations are available every 5 minutes, and each value is the mean of the last 15 minutes (sampling interval), with an instrument frequency of 0.2 Hz (for both direction and speed). The wind gust value is the maximum wind speed over the last 15 minutes, measured at instrument frequency. The direction of the gust value is not reported.

From now on, wind speed is considered as the absolute value of the wind vector, such that it is a positive quantity, and will be expressed in meters per seconds. In some analyses the frequency distribution of wind speed is expressed using the Beaufort scale (see App. E).

For wind direction it is adopted the convention to consider the direction from which the wind is blowing (meteorological convention). Wind directions is a continuous variable, but in some analyses it is sometimes discretized in 16 sectors 22°30' wide, corresponding to the cardinal directions, such as North (N), North-North-East (NNE), North-East (NE), etc. The first sector (N) ranges between -11°14'99' North to 11°15' North.

The dataset was pre-validated by ICPSM. A final quality control check of the data was done before the analyses. The following tests were performed: date and time control; range constraints; repeated data check; block sensor problem; spike exclusion. The following range limits were used: 0°-360°for wind direction; 0-50 m/s for wind speed (both mean and gust). Sensors were considered to be not operational if observations do not change for more than 36 and 12 consecutive measure, for wind direction and speed respectively. Spike analysis were considered only for consecutive data. The limits for spike exclusion are: ±180°for wind direction and ±20 m/s for wind speed. Because it was decided to use wide limits for data quality control, a plot-based visual check was performed to identify problematic data. In case of doubtful data, they were compared with other datasets. Wind data values

without direction or speed information have been excluded from the analysis. Isolated data (no data before and after) were also excluded form the analysis. There is no interpolation for missing data.

Being wind speed proportional to elevation, for result comparison wind measurements are converted to the standard height of 10 m, by the use of the Hellmann law. This correlates the wind speed readings at two different heights (near water surface), under the hypothesis of atmospheric neutral stability, namely

$$v(z) = v(z_0)(\frac{z}{z_0})^{\alpha} \tag{2.1}$$

where z_0 is the height of measured wind velocity, $v(z_0)$; z is the elevation at which the wind velocity needs to be estimated; the exponent α is a function of: orography, height, hour of the day, season, land features and surface roughness, wind speed, temperature, and air condition. Despite its variability, a constant roughness coefficient of 0.11 is considered because, for the considered heights (9 to 15 m), the effect of a variable Hellman exponent is negligible (less than 4%). For the same reason Hellmann's law, rather than the more appropriate Monin-Obukhov correction is adopted.

Wind is a continuous variable and, due to analogue to digital conversion (ADC), it is recorded in discrete values. The anemometers used record wind values as multiple of about 0.10 m/s and the frequency of a specific value is the frequency of all wind values in an 0.1-width interval around the recorded value. However, it is not known how this interval is distributed, unless one knows the specifications of the ADC device. For example, if the ADC uses a step function, the interval is at the right of the measured value. In this way, having wind speed approximately a Weibull distribution, measurements overestimate wind less than the most frequent value of wind velocity. For goodness of fit calculations, one has to compare the measured frequency at the discrete wind values with the integral of the PDF over the unknown interval. Again, this involves some error. In the following, it is assumed

that the interval is symmetric with respect to the measured values. An evaluation of the error is made using the Weibull distribution of the entire data set for station PAA and comparing a ADC right step function with a ADC symmetric function. For the lowest wind velocities the error could be more than 10% of the expected frequency; for the high speed tail the mean error is of 2.5%. In the region of the mode of the distribution the error is less than 0.1% of the expected frequency. Even if this source of error may not be so relevant in practice, it is important to remember its existence, specially when one calculates a continuous distribution from "discrete" measurements.

2.3.3 Wind Rose diagram

Wind rose is a simple way to present wind speed and direction statistics in a straightforward visual form. In practice, it is a polar histogram of wind direction data in which each sector is a frequency histogram of wind speed data for that direction. The length of each spoke displays the frequency of time the wind blows from that direction. Each concentric circle represents a different frequency. Each spoke presents the frequency of time the wind blows at certain speed ranges (for that direction) by colour bands of appropriate length. Tables of frequencies and summary statistics are produced along with the wind rose diagram. The developed code for wind rose was obtained by modifying the Matlab code shared by M. Ma.

2.3.4 Probability plot

A probability plot (PP) is a graph for the comparison of two dataset, either empirical (measured) or theoretical (PDF based) set. A PP plots two Cumulative Distribution Function (CDF's) against each other. It is a parametric graph with range $[0, 1] \times [0, 1]$. Each point in a PP corresponds to a couple of CDF evaluated at the same wind speed. For identical distributions, all points lie along the diagonal between (0,0) and (1,1); any deviation indicates a difference between the distributions; the greater the distance from

the diagonal, the grater the deviation. The maximum deviation is measured by the Kolmogorov-Smirnov test.

2.3.5 Wind speed distribution

There are several probability density functions (PDF) which provide a good analytical approximation for wind speed frequency near the sea-surface.

After a quick analysis with several PDF's used in literature, a selection of ten PDFs is used in the following.

In particular, we consider the following distributions: Maximum Stable, Gumbel, Extreme Value, Frechet, Weibull, Pareto, Gamma, LogNormal, LogGamma and Erlang.

With the aim of considering zero wind speed in the description of wind regimes, some researchers use hybrid distribution. Following this idea, it is introduced a slightly more complete version, which consider also the lost data. Lost data are the sum of not registered measurements (for example due to instrument breakdown) and values that were registered but that have not passed the quality controls. For any of the following PDF the hybrid distribution, h, corrected for lost data is determined by:

$$h[x;\theta_0,\theta_N,\Phi] = (1-\theta_N)\theta_0\delta[x] + (1-\theta_N-(1-\theta_N)\theta_0)f[x,\Phi] \qquad (2.2)$$

where x is the wind speed variable; θ_0 is the probability of null wind speed observations in the dataset; θ_N is the absolute frequency of lost data; Φ is a set of parameters of the main PDF; δ is the Dirac function; f is the PDF of positive wind speeds in the dataset. Lost data are computed as the difference between the total number of potential measurements (that is, time series length divided by temporal resolution) and dataset actual length. Absolute frequency of lost data is computed as the rate of lost data over total possible measurements. When the dataset is complete (no lost data; $\theta_N = 0$) the hybrid distribution reduces to the usual form, when wind speed

is strictly positive it reduces to a normal PDF.

In the literature there are some differences in the definitions of the analysed distributions, so in the following I report a brief description of each distribution. In the tables and plots throughout the Chapter the different PDFs are indicated as follows: W for Weibull; M for Maximum Stable; G for Gumbel; EV for Extreme Value; F for Frechet; Γ for Gamma; P for Pareto; LN for Log Normal; $L\Gamma$ for Log Gamma; E for Erlang.

Weibull distribution

The Weibull distribution is the most used PDF for wind speed data interpolation. It shows great flexibility and, even if it is quite simple, it generally gives a good fit to experimental data. In fact, according to the International Standard IEC 61400-12 and other international recommendations, the Weibull PDF is the most appropriate distribution for wind speed data. The Weibull distribution is a continuous three-parameter probability density function given by

$$f_W[x;\alpha,\beta,\mu] = \frac{\beta}{\alpha}\left(\frac{x-\mu}{\alpha}\right)^{\beta-1}\exp\left(-\left(\frac{x-\mu}{\alpha}\right)^{\beta}\right) \tag{2.3}$$

where $v \geq \mu$ ($\mu > 0$ is the location parameter (m/s)), $\alpha > 0$ is the Weibull scale parameter (m/s), $\beta > 0$ is the Weibull shape parameter (dimensionless). The Weibull shape parameter generally ranges from 1.1 to 3 for most wind conditions. The location parameter is the minimum observed (or modelled) wind speed. By taking $\mu = 0$, the three parameter Weibull distribution reduces to a two parameter Weibull distribution, that is the most used distribution for wind speed interpolation; if also $\alpha = 2$, it becomes the Rayleigh distribution.

The cumulative frequency distribution is the integral of the Weibull prob-

ability density function, and is given by

$$F_W[x;\alpha,\beta,\mu] = 1 - \exp\left(\frac{x-\mu}{\alpha}\right)^{\beta} \tag{2.4}$$

Averages of powers of v are simply given by

$$mean(v^k) = \alpha^k \Gamma\left(1 + \frac{k}{\beta}\right) \tag{2.5}$$

In particular, the mean (m_W), variance (σ_W) and median (M_W) are given by:

$$m_W = mean(v) = \mu + \alpha\Gamma\left(1 + \frac{1}{\beta}\right) \tag{2.6}$$

$$\sigma_W = mean(v^2) = \alpha^2\left(-\Gamma\left(1 + \frac{1}{\beta}\right)^2 + \Gamma\left(1 + \frac{2}{\beta}\right)\right) \tag{2.7}$$

$$M_W = \mu + \alpha Log(2)^{\frac{1}{\beta}} \tag{2.8}$$

Maximum Stable distribution

The Maximum Stable (hereafter MaxStable) distribution is also known as Generalized Maximum Extreme Value distribution or FisherTippett distribution. It is hardly ever used in wind speed distribution analysis. However, it shows a good fit to the actual database. The MaxStable distribution $f_M[x;\alpha,\beta,\mu]$ is a continuous three-parameter probability density function given by

$$f_M = \begin{cases} \alpha^{-1} e^{-\frac{x-\mu}{\alpha} - e^{-\frac{x-\mu}{\alpha}}} & \beta = 0 \\ \alpha^{-1} e^{-\left(\frac{\beta(x-\mu)}{\alpha}+1\right)^{-1/\beta}} \left(\frac{\beta(x-\mu)}{\alpha} + 1\right)^{-\frac{1}{\beta}-1} & \beta \neq 0 \,\&\, 1 + \frac{\beta(x-\mu)}{\alpha} > 0 \\ 0 & \text{otherwise} \end{cases} \tag{2.9}$$

where $v > \mu$; $\alpha > 0$ is the scale parameter (m/s); β is the shape parameter (dimensionless) and $\mu > 0$ is the location parameter (m/s). The cumulative frequency distribution is

$$F_M[x;\alpha,\beta,\mu] = \begin{cases} e^{-e^{-\frac{x-\mu}{\alpha}}} & \beta = 0 \\ e^{-\left(\frac{\beta(x-\mu)}{\alpha}+1\right)^{-1/\beta}} & \beta \neq 0 \,\&\, 1 + \dfrac{\beta(x-\mu)}{\alpha} > 0 \\ 1 & \text{otherwise} \end{cases} \tag{2.10}$$

The mean (m_M), variance (σ_M) and median (M_M) are given by:

$$m_M = \begin{cases} \gamma_E \alpha + \mu & \beta = 0 \\ \dfrac{\alpha\Gamma[1-\beta] - \alpha + \beta\mu}{\beta} & \beta \neq 0 \,\&\, \beta < 1 \\ \text{Indeterminate} & \text{otherwise} \end{cases} \tag{2.11}$$

$$\sigma_M = \begin{cases} \dfrac{\pi^2\alpha^2}{6} & \beta = 0 \\ \dfrac{\alpha^2\left(\Gamma[1-2\beta] - \Gamma[1-\beta]^2\right)}{\beta^2} & \beta \neq 0 \,\&\, 2\beta < 1 \\ \text{Indeterminate} & \text{otherwise} \end{cases} \tag{2.12}$$

$$M_M = \begin{cases} \mu - \alpha \log[\log[2]] & \beta = 0 \\ \mu - \dfrac{\alpha\left(1 - \log^{-\beta}[2]\right)}{\beta} & \text{otherwise} \end{cases} \tag{2.13}$$

where γ_E is the Euler's constant.

Gumbel distribution

The Gumbel distribution is a continuous two-parameter probability density function given by

$$f_G[x;\alpha,\mu] = \frac{e^{\frac{x-\mu}{\alpha}-e^{\frac{x-\mu}{\alpha}}}}{\alpha} \tag{2.14}$$

where $v > \mu$; $\alpha > 0$ is the scale parameter (m/s) and $\mu > 0$ is the location parameter (m/s). The cumulative frequency distribution is

$$F_G[x;\alpha,\mu] = 1 - e^{-e^{\frac{x-\mu}{\alpha}}} \tag{2.15}$$

The mean (m_G), variance (σ_G) and median (M_G) are given by:

$$m_G = \mu - \gamma_E \alpha \tag{2.16}$$

$$\sigma_G = \frac{\pi^2 \alpha^2}{6} \tag{2.17}$$

$$M_G = \alpha \log[\log[2]] + \mu \tag{2.18}$$

Extreme Value distribution

The Extreme Value distribution is a continuous two-parameter probability density function given by

$$f_{EV}[x;\alpha,\mu] = \frac{e^{-\frac{x-\mu}{\alpha}-e^{-\frac{x-\mu}{\alpha}}}}{\alpha} \tag{2.19}$$

where f_{EV} is the probability of the measured wind speed, $v > \mu$; $\alpha > 0$ is the scale parameter (m/s) and $\mu > 0$ is the location parameter (m/s). The cumulative frequency distribution is

$$F_{EV}[x;\alpha,\mu] = e^{-e^{-\frac{x-\mu}{\alpha}}} \tag{2.20}$$

The mean (m_{EV}), variance (σ_{EV}) and median (M_{EV}) are given by:

$$m_{EV} = \mu + \gamma_E \alpha \tag{2.21}$$

$$\sigma_{EV} = \frac{\pi^2 \alpha^2}{6} \tag{2.22}$$

$$M_{EV} = -\alpha \log[\log[2]] + \mu \tag{2.23}$$

Frechet distribution

The Frechet distribution is a continuous three-parameter probability density function given by

$$f_F[x; \alpha, \beta, \mu] = \frac{\beta e^{-\left(\frac{x-\mu}{\alpha}\right)^{-\beta}} \left(\frac{x-\mu}{\alpha}\right)^{-\beta-1}}{\alpha} \tag{2.24}$$

$v > \mu$; $\alpha > 0$ is the scale parameter (m/s); $\beta > 0$ is the shape parameter (dimensionless) and $\mu > 0$ is the location parameter (m/s). The cumulative frequency distribution is

$$F_F[x; \alpha, \mu] = e^{-\left(\frac{x-\mu}{\alpha}\right)^{-\beta}} \tag{2.25}$$

The mean (m_F), variance (σ_F) and median (M_F) are given by:

$$m_F = \begin{cases} \alpha \Gamma[1 - 1/\beta] + \mu & \beta > 1 \\ \infty & \text{otherwise} \end{cases} \tag{2.26}$$

$$\sigma_F = \begin{cases} \alpha^2 \left(\Gamma[1 - 2/\beta] - \Gamma[1 - 1/\beta]^2\right) & \beta > 2 \\ \infty & \text{otherwise} \end{cases} \tag{2.27}$$

$$M_F = \alpha \log[2]^{-1/\beta} + \mu \tag{2.28}$$

Gamma distribution

The Gamma distribution is an emergent PDF for wind speed data interpolation. This distribution is often referred to as Generalized Gamma distribution, to distinguish it from 2-parameter Gamma and 3-parameter Pearson type III, which are particular cases of this distribution. It shows great flexibility, it is an extension of other PDF's (among the others the Weibull). The Gamma distribution is a continuous four-parameter probability density function given by

$$f_\Gamma[x;\alpha,\beta,\gamma,\mu] = \frac{\gamma}{\alpha\Gamma[\beta]}\left(\frac{x-\mu}{\alpha}\right)^{\gamma\beta-1}\exp\left(-\left(\frac{x-\mu}{\alpha}\right)^{\gamma}\right) \tag{2.29}$$

where $v > \mu$; $\alpha > 0$ is the scale parameter (m/s); $\beta > 0$ and $\gamma > 0$ are the shape parameters (dimensionless) and $\mu > 0$ is the location parameter (m/s). By taking $\gamma = 1$ the four parameter Gamma distribution reduces to a 3-parameter Pearson type III; by taking also $\mu = 0$ it reduces to a 2-parameter Gamma distribution (the most used among the Gamma family for wind speed interpolation). The cumulative frequency distribution is the integral of the Gamma probability density function, and it is given as function of the regularized incomplete gamma function Q

$$F_\Gamma[x;\alpha,\beta,\gamma,\mu] = Q[\beta,0,\left(\frac{x-\mu}{\alpha}\right)^{\gamma}] \tag{2.30}$$

The mean (m_Γ), variance (σ_Γ) and median (M_Γ) are given by:

$$m_\Gamma = \mu + \frac{\alpha\Gamma[\beta+1/\gamma]}{\Gamma[\beta]} \tag{2.31}$$

$$\sigma_\Gamma = \frac{\alpha^2\left(-\Gamma[\beta+1/\gamma]+\Gamma[\beta]\Gamma[\beta+2/\gamma]\right)}{\Gamma[\beta]^2} \tag{2.32}$$

$$M_\Gamma = \mu + \alpha Q^{-1}[\beta,0,1/2]^{1/\gamma} \tag{2.33}$$

where Q^{-1} is the inverse of the regularized incomplete gamma function.

Pareto distribution

The Pareto distribution is a continuous four-parameter probability density function given by

$$f_P[x;\alpha,\beta,\gamma,\mu] = \frac{\beta\alpha^{-1/\gamma}(x-\mu)^{\frac{1}{\gamma}-1}\left(\left(\frac{\alpha}{x-\mu}\right)^{-1/\gamma}+1\right)^{-\beta-1}}{\gamma} \tag{2.34}$$

where $v > \mu$; $\alpha > 0$ is the scale parameter (m/s); $\beta > 0$ and $\gamma > 0$ are the shape parameters (dimensionless) and $\mu > 0$ is the location parameter (m/s). The cumulative frequency distribution is

$$F_P[x;\alpha,\beta,\gamma,\mu] = 1 - \left(\left(\frac{x-\mu}{\alpha}\right)^{1/\gamma}+1\right)^{-\beta} \tag{2.35}$$

The mean (m_P), variance (σ_P) and median (M_P) are given by:

$$m_P = \begin{cases} \dfrac{\alpha\Gamma[\gamma+1]\Gamma[\beta-\gamma]}{\Gamma[\beta]} + \mu & \beta > 1 \\ \text{Indeterminate} & \text{otherwise} \end{cases} \tag{2.36}$$

$$\sigma_P = \begin{cases} \dfrac{\alpha^2\left(\Gamma[\beta]\Gamma[2\gamma+1]\Gamma[\beta-2\gamma] - \Gamma[\gamma+1)^2\Gamma[\beta-\gamma]^2\right)}{\Gamma[\beta]^2} & \beta > 2\gamma \\ \text{Indeterminate} & \text{otherwise} \end{cases} \tag{2.37}$$

$$M_P = \alpha\left(2^{1/\beta}-1\right)^{\gamma} + \mu \tag{2.38}$$

LogNormal distribution

The Log Normal distribution is a continuous two-parameter probability density function given by

$$f_{LN}[x;\sigma,\mu] = \frac{e^{-\frac{(\log[x]-\mu)^2}{2\sigma^2}}}{\sqrt{2\pi}\sigma x} \tag{2.39}$$

where $v > 0$; $\sigma > 0$ is the standard deviation and $\mu > 0$ is the mean (m/s). The cumulative frequency distribution is

$$F_{LN}[x;\sigma,\mu] = \frac{1}{2}\text{Erfc}\left(\frac{\mu - \log(x)}{\sqrt{2}\sigma}\right) \tag{2.40}$$

where Erfc is the the complementary error function. The mean (m_{LN}), variance (σ_{LN}) and median (M_{LN}) are given by:

$$m_{LN} = e^{\mu+\frac{\sigma^2}{2}} \tag{2.41}$$

$$\sigma_{LN} = e^{2\mu+\sigma^2}\left(-1 + e^{\sigma^2}\right) \tag{2.42}$$

$$M_{LN} = e^{\mu} \tag{2.43}$$

Log Gamma distribution

The Log Gamma distribution is a continuous three-parameter probability density function given by

$$f_{L\Gamma}[x;\alpha,\beta,\mu] = \frac{\beta^{-\alpha}(1+x-\mu)^{-\frac{1+\beta}{\beta}}\log[1+x-\mu]^{-1+\alpha}}{\Gamma[\alpha]} \tag{2.44}$$

where $v > 0$; $\alpha > 0$ and $\beta > 0$ are the shape parameters and $\mu > 0$ is the location parameter (m/s). The cumulative frequency distribution is

$$F_{L\Gamma}[x;\alpha,\beta,\mu] = Q[\alpha, 0, \frac{\log[1+x-\mu]}{\beta}] \tag{2.45}$$

where Q is the the generalized regularized incomplete gamma function. The mean ($m_{L\Gamma}$), variance ($\sigma_{L\Gamma}$) and median ($M_{L\Gamma}$) are given by:

$$m_{L\Gamma} = \begin{cases} (1-\beta)^{-\alpha} + \mu - 1 & \beta < 1 \\ \infty & \text{otherwise} \end{cases} \tag{2.46}$$

$$\sigma_{L\Gamma} = \begin{cases} (1-2\beta)^{-\alpha} - (1-\beta)^{-2\alpha} & \beta < 1/2 \\ \infty & \text{otherwise} \end{cases} \tag{2.47}$$

$$M_{L\Gamma} = -1 + e^{\beta\, Q^{-1}[\alpha,0,1/2]} + \mu \tag{2.48}$$

where Q^{-1} is the inverse of the generalized regularized incomplete gamma function.

Erlang distribution

The Erlang distribution is a continuous two-parameter probability density function given by

$$f_E[x;\alpha,k] = \frac{\alpha^k x^{k-1} e^{-x\alpha}}{\Gamma[k]} \tag{2.49}$$

where $v > 0$; k is the shape parameter (positive integer) and $\alpha > 0$ is the rate. The cumulative frequency distribution is

$$F_E[x;\alpha,k] = Q[k,0,\alpha x] \tag{2.50}$$

The mean (m_E), variance (σ_E) and median (M_E) are given by:

$$m_E = \frac{k}{\alpha} \tag{2.51}$$

$$\sigma_E = \frac{k}{\alpha^2} \tag{2.52}$$

$$M_E = \frac{Q^{-1}[k, 0, 1/2]}{\alpha} \tag{2.53}$$

2.3.6 Parameter estimation methods

The present work almost exclusively uses the maximum likelihood method to estimate the parameters of the distributions to be compared (Chang, 2011, [36]). The maximum likelihood estimator is quite stable and relatively easy to use, except in the presence of distributions which do not converge rapidly. Furthermore, it usually yields lower estimation mean square errors with respect to the moment method.

2.3.7 Accuracy evaluation criteria

When dealing with distribution modelling, accuracy evaluation starts with visual analysis. The first step is the construction of a plot that shows data histograms and distribution functions. In this way it is possible to have an idea of what distributions are fitting better. Subsequently accuracy is evaluated on the basis of probability plots.

However, to give more objective results, the distribution performances are tested by numerical analysis. To evaluate the goodness of fitting (GOF) of the considered distributions, several tests are used.

One of the most used GOF measures is the well-known determination coefficient (R^2). This coefficient indicates how much of the total variation in the dependent variable can be accounted for by the derived PDF. The higher the value of the R^2 (with maximum 1) is, the better the calculated distribution approximates the measured data.

Another common GOF is the root mean square error (RMSE), the most

used in literature along with R^2.

Because of historical importance and for comparison with concerning literature, the Pearson Chi-square error (χ^2) is calculated and reported, even if it is not the best test for continuous distributions.

The values of these tests are dependent on how data are binned, whereas the following tests are independent from the number of wind speed classes. The Kolmogorov-Smirnov (KS) and Anderson-Darling (AD) tests are statistical tests specifically designed for GOF of continuous distributions. The KS test is based on the empirical distribution function. The AD test is a modification of the KS test to better adapt the test to different distributions. In the KS test, the critical values do not depend on the specific distribution being tested. Instead, the AD test makes use of the specific distribution in calculating critical values; for this reason it could be considered a more sensitive test. The AD test gives more weight to the tails of the distribution with respect to the KS test; the latter is more sensitive near the centre of the distribution.

2.3.8 Wind power density

For many application, it is convenient to estimate the wind energy output.The wind kinetic energy can be expressed as

$$E(v) = \frac{1}{2}mv^2 \tag{2.54}$$

where m is the mass of the air and v is the instantaneous wind speed vector. Taking into account a cross section area A, perpendicular to the wind direction, and a time interval t, the considered air mass could be modelled as ρAvt; that is: air density ρ (1.225 kg/m^3, in standard conditions) times the considered volume, the latter being the product of the cross section and the length covered by air in time t. In this way equation 2.54 becomes

$$E(v) = \frac{1}{2}\rho Av^3t \tag{2.55}$$

Now it is possible to derive the wind power per unit area perpendicular to wind direction per unit time

$$P(v) = \frac{1}{2}\rho v^3 \tag{2.56}$$

Taking advantage of wind PDF results, it is possible to define a wind power density distribution as

$$p(v) = \frac{1}{2}\rho v^3 f[v] \tag{2.57}$$

where $f[v]$ is a wind speed PDF. The wind power density is expressed in Wm^{-2}. For simplicity the air density is often assumed to be constant, despite it being a function of temperature, pressure and humidity. Considering the common range of air density for the Venice Lagoon, taking into account the typical variation of pressure, temperature and humidity, it is possible to calculate the error introduced with constant air density hypothesis: it is at most of 10% (see also Waewsak et al., 2011 [39]). An interesting model without this restriction is analysed by Carta and Mentado (2007, [40]). They also conclude that the difference between considering or not constant air density is negligible in areas where the standard air density is similar to the mean air density and the range of variation is narrow. The total wind power density per unit area can be expressed as

$$P_t = \frac{1}{2}\rho \int_0^\infty v^3 f[v]\, dv \tag{2.58}$$

It is also convenient to define a threshold wind power density as the wind power density for a wind greater than a minimal velocity

$$P_m = \frac{1}{2}\rho \int_{v_m}^\infty v^3 f[v]\, dv \tag{2.59}$$

In the Venice Lagoon the minimal wind velocity to generate a stable wind-wave field (with favourable characteristics for erosion purposes) is around 6

station	mean ± std ws (m/s)	max ws (m/s)	max dir (°)	max gust (m/s)	mode ws (m/s)	mode dir (°)	median ws (m/s)
PAA	4.8±3.6	30.1	336	42.1	3.0	40	3.9
SAL	3.3±2.2	20.8	60	26.2	1.9	31	2.6
CHI	3.8±2.7	21.4	65	30.7	2.4	42	3.3

Table 2.2: Global statistics for all station from whole dataset (11 years for PAA and SAL; 8 years for CHI). The columns represent: station; mean and standard deviation of wind speed; maximum recorded wind speed and its direction; maximum wind speed gust; wind speed mode and wind direction mode; wind speed median.

m/s at 10 m above water (from direct measurements, not reported here).

2.4 Results and discussion

2.4.1 Wind speed

Global statistics

In this section, global statistics are reported for the entire dataset (Tab.: 2.2 on page 72), considering 11 years for PAA and SAL station, 8 years for CHI station.

It should be noticed that, for the SAL station, missing data are about 10% of the overall period duration. Looking at the yearly plots (see fig. 2.14 on page 98), it is clear that this is primarily related to the large number of missing data in year 2002 (about 72%).

The maximum gust velocity at CHI station is 49 m/s, but it is considered as a spike or an exceptional event. It happened twice in 15 minutes with a mean wind speed of about 10 m/s. There would be a maximum gust at PAA station of 48 m/s, but its interpretation is not clear. It happened in a 20 minute event with a before-event mean wind speed of about 8 m/s and an after-event mean wind speed of 15 m/s; the maximum 5-minute mean wind speed was 30 m/s.

A more comprehensive description of the data is presented in the three

rose plots of figure 2.2 (page 75).

As expected, it is clear from table 2.2 and figure 2.2 (page 72 and 75), that wind velocity in the Venice lagoon is weaker than in the open sea (with a median wind speed of 3.9 ms^{-1}). The Southern station in the lagoon displays higher wind speeds than the Northern part (median wind speed of 3.3 ms^{-1} vs 2.6 ms^{-1}).

For all the stations, the dominant wind is Bora (wind direction around North-East), with a probability of occurrence of about 18% for PAA and 13% for SAL and CHI. If a wider range of directions around the main North-East Bora direction the probability increases to 38% for PAA and around 32% for the lagoon stations. A second important wind direction is around South-East (Scirocco), with a probability of 6% for the open sea and about 7% in the lagoon. Because of the surrounding landscape morphology in the Northern part of the lagoon, the Bora wind is more North-oriented than in the open sea. On the contrary, in the Southern part wind is more widely distributed from North-East to South-East and, differently from the other stations, CHI presents also a relevant wind from the South-West direction, in connection with land-sea breeze.

These results are consistent with what is reported in Massalin and Canestrelli ([41]), even if they analysed only PAA data for the period 1983-2004.

From tables 2.3-2.5 (pages 76-78) it is evident that the calm condition (wind intensity less than 0.3 ms^{-1}) has a low probability to occur at all stations (less than 4%). This agrees with previous wind studies ([41]). The most probable condition is of light to gentle breeze (wind speed between 1.6 to 5.4 ms^{-1}) with a probability greater than 50%. The probability of wind speed greater than breeze ($> 10.7\ m/s$) is low inside the lagoon (less than 3%) but not negligeble in the open sea, with a probability about 8%. From measurements of wind-wave generation in the Venice Lagoon, it seems that only a wind velocity larger than gentle breeze ($> 5.4\ m/s$) is able to generate a wave field capable of eroding salt-marsh banks. Inside the lagoon, the probability to have a wind speed greater than gentle breeze is about 13%

and 21% for the Northern and Southern part of the lagoon respectively.

The parameters of the tested PDF and the statistical GOF are listed in table 2.6 (page 80). The wind speed data histograms with the calculated PDF are presented in Figure 2.3 (page 81).

From tab. 2.6 (page 80), it is clear that it is difficult, and in some way subjective, to establish which is the best distribution to model the data. Figures 2.4-2.6 (page82-84) 82-84) show the histogram with each PDF (top panel), and report PP-plots for each PDF (bottom panel). From these figures, it is possible to see how some PDFs give a good representation of the data only for a portion of the histogram, but any or few give a suitable data interpolation for the entire range of wind speed.

In the case of PAA station, good choices could be: MaxStable and Gamma distributions (for their low RMSE and high χ^2 and R^2 values) or Weibull, Pareto and Erlang distributions for their high values in Anderson Darling and Kolmogorov Smirnov tests. As best choice, it is assumed the Erlang distribution.

Data from station SAL are best modelled by Gamma, Pareto and Erlang distributions (good values in all tests) and with less agreement by MaxStable distribution (good results in RMSE, χ^2 and R^2 tests). As best choice, it is assumed the Gamma distribution.

Gamma, Pareto and Extreme Value distributions seem to be good choices for CHI station, due to their high score in all statistical test; looking at only RMSE and R^2 GOF also MaxStable distribution appears to be good interpolating distributions. As best choice, it is assumed the Extreme Value distribution.

For the selected geographical area, the Pareto, Gamma and Erlang distributions seems to be the most adequate distributions for wind speed analysis, with Pareto as the more suitable. Considering only RMSE and R^2 as GOF, then the best representative distributions are MaxStable and Gamma, with MaxStable as best choice.

For the analysed stations, the Weibull distribution is to be considered a

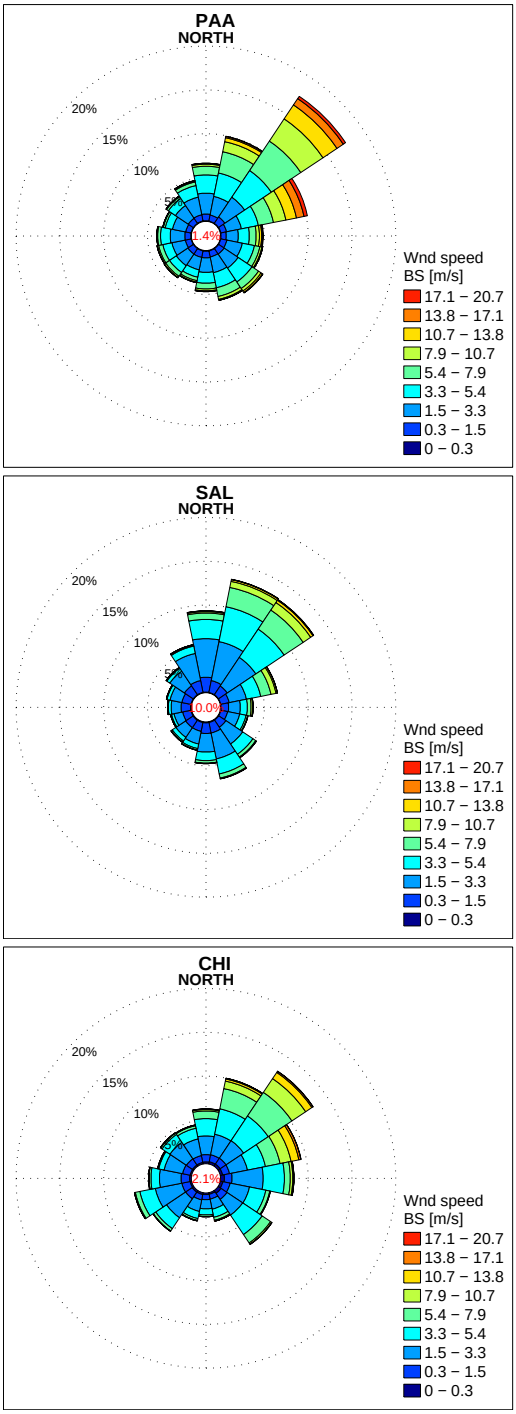

Figure 2.2: Wind rose of the entire dataset for the three stations. Lost data percent refers to not-recorded or false data and are reported in red inside the inner circle.

	wind direction																
BFS	(348.8° ,11.3°]	(11.3° ,33.8°]	(33.8° ,56.3°]	(56.3° ,78.8°]	(78.8° ,101.3°]	(101.3° ,123.8°]	(123.8° ,146.3°]	(146.3° ,168.8°]	(168.8° ,191.3°]	(191.3° ,213.8°]	(213.8° ,236.3°]	(236.3° ,258.8°]	(258.8° ,281.3°]	(281.3° ,303.8°]	(303.8° ,326.3°]	(326.3° ,348.8°]	percent
$[0, 0.3)$	0.07	0.06	0.06	0.07	0.06	0.05	0.07	0.08	0.08	0.07	0.06	0.06	0.07	0.06	0.06	0.07	1.05
$[0.3, 1.5)$	0.77	0.70	0.87	0.66	0.60	0.71	0.75	0.70	0.76	0.76	0.75	0.67	0.68	0.64	0.70	0.72	11.45
$[1.5, 3.3)$	2.38	2.17	2.71	1.74	1.37	1.80	1.92	1.83	1.66	1.45	1.58	1.56	1.66	1.54	1.77	2.05	29.19
$[3.3, 5.4)$	2.08	2.72	3.66	1.97	1.26	1.41	1.91	1.75	1.24	0.86	0.94	1.05	1.10	0.84	0.97	1.35	25.11
$[5.4, 7.9)$	0.99	2.48	4.05	1.75	0.78	0.63	0.90	1.01	0.65	0.40	0.53	0.49	0.33	0.22	0.25	0.42	15.88
$[7.9, 10.7)$	0.23	1.17	3.04	1.45	0.37	0.23	0.35	0.34	0.21	0.17	0.18	0.15	0.07	0.04	0.05	0.10	8.15
$[10.7, 13.8)$	0.08	0.47	1.92	1.22	0.25	0.08	0.19	0.09	0.08	0.06	0.02	0.03	0.02	0.02	0.02	0.04	4.58
$[13.8, 17.1)$	0.02	0.14	0.86	0.88	0.12	0.01	0.05	0.02	0.01	0.	0.	0.	0.	0.	0.	0.01	2.14
$[17.1, 20.7)$	0.01	0.04	0.32	0.40	0.06	0.	0.01	0	0	0	0.	0.	0.	0.	0.	0.	0.84
$[20.7, 24.4)$	0	0.01	0.07	0.05	0.01	0.	0.	0	0.	0	0	0.	0.	0.	0.	0.	0.14
$[24.4, 28.4)$	0	0.	0.	0.	0.	0	0	0	0	0	0	0.	0	0	0	0.	0.1
$[28.4, 32.6)$	0	0	0	0	0	0	0	0	0	0	0	0	0	0	0	0.	0.
≥ 32.6	0	0	0	0	0	0	0	0	0	0	0	0	0	0	0	0	0
percent	6.63	9.95	17.56	10.18	4.89	4.93	6.15	5.82	4.69	3.77	4.08	4.02	3.93	3.35	3.81	4.77	98.54

Table 2.3: Station PAA. Table of percent frequency for each class of possible wind speed and direction. The frequency distribution of wind speed is made according to the Beaufort scale (see App. E). Wind directions are distributed in 16 sectors 22°30' wide, corresponding to the cardinal directions. Last column and last raw report the total sum of corresponding raw and column respectively. The remaining percent correspond to unrecorded or false data (1.43%) and sum of frequency less than 0.01% (0.07%). With 0. it is indicated probability less than 0.01%.

	wind direction																
BFS	(348.8°,11.3°]	(11.3°,33.8°]	(33.8°,56.3°]	(56.3°,78.8°]	(78.8°,101.3°]	(101.3°,123.8°]	(123.8°,146.3°]	(146.3°,168.8°]	(168.8°,191.3°]	(191.3°,213.8°]	(213.8°,236.3°]	(236.3°,258.8°]	(258.8°,281.3°]	(281.3°,303.8°]	(303.8°,326.3°]	(326.3°,348.8°]	percent
[0, 0.3)	0.07	0.06	0.06	0.06	0.06	0.07	0.08	0.10	0.11	0.10	0.11	0.09	0.10	0.08	0.07	0.07	1.29
[0.3, 1.5)	1.69	1.39	1.20	0.98	0.86	0.78	1.00	1.22	1.21	1.02	1.01	0.95	1.08	1.06	1.21	1.38	18.06
[1.5, 3.3)	4.41	4.53	3.92	2.01	1.34	1.40	2.29	3.01	2.13	1.47	1.33	1.00	1.12	1.37	2.01	3.15	36.50
[3.3, 5.4)	2.19	4.06	3.88	1.66	0.81	0.74	1.41	1.75	0.97	0.53	0.49	0.29	0.32	0.35	0.40	0.85	20.72
[5.4, 7.9)	0.73	2.24	2.61	1.18	0.42	0.18	0.39	0.48	0.29	0.16	0.16	0.08	0.07	0.06	0.08	0.12	9.25
[7.9, 10.7)	0.16	0.71	1.03	0.59	0.17	0.04	0.08	0.09	0.05	0.04	0.02	0.02	0.01	0.02	0.02	0.03	3.08
[10.7, 13.8)	0.07	0.20	0.32	0.15	0.05	0	0.01	0.01	0.01	0.01	0.	0.	0.	0.	0.01	0.01	0.85
[13.8, 17.1)	0.02	0.03	0.08	0.01	0.	0	0.	0	0.	0	0.	0.	0.	0.	0.	0.	0.16
[17.1, 20.7)	0.	0.	0.01	0.	0.	0	0	0	0	0	0	0.	0.	0	0	0	0.02
[20.7, 24.4)	0.	0	0	0.	0	0	0	0	0	0	0	0	0	0	0	0	0
[24.4, 28.4)	0	0	0	0	0	0	0	0	0	0	0	0	0	0	0	0	0
[28.4, 32.6)	0	0	0	0	0	0	0	0	0	0	0	0	0	0	0	0	0
≥ 32.6	0	0	0	0	0	0	0	0	0	0	0	0	0	0	0	0	0
percent	9.34	13.22	13.12	6.65	3.71	3.22	5.25	6.67	4.76	3.34	3.13	2.44	2.71	2.94	3.80	5.62	89.93

Table 2.4: Station SAL. Table of percent frequency for each class of possible wind speed and direction. The frequency distribution of wind speed is made according to the Beaufort scale (see App. E). Wind directions are distributed in 16 sectors 22°30' wide, corresponding to the cardinal directions. Last column and last raw report the total sum of corresponding raw and column respectively. The remaining percent correspond to unrecorded or false data (10.03%) and sum of frequency less than 0.01% (0.04%). With 0. it is indicated probability less than 0.01%.

	wind direction																
BFS	(348.8° ,11.3°]	(11.3° ,33.8°]	(33.8° ,56.3°]	(56.3° ,78.8°]	(78.8° ,101.3°]	(101.3° ,123.8°]	(123.8° ,146.3°]	(146.3° ,168.8°]	(168.8° ,191.3°]	(191.3° ,213.8°]	(213.8° ,236.3°]	(236.3° ,258.8°]	(258.8° ,281.3°]	(281.3° ,303.8°]	(303.8° ,326.3°]	(326.3° ,348.8°]	percent
$[0, 0.3)$	0.19	0.25	0.27	0.25	0.40	0.27	0.36	0.16	0.16	0.18	0.20	0.16	0.17	0.14	0.16	0.17	3.51
$[0.3, 1.5)$	0.81	0.76	0.77	0.77	0.86	0.83	0.80	0.55	0.56	0.62	0.86	0.90	0.93	0.84	0.81	0.75	12.42
$[1.5, 3.3)$	2.03	2.28	2.32	2.10	3.61	2.26	2.18	1.15	1.09	1.32	2.58	3.06	2.40	2.11	2.18	1.86	34.54
$[3.3, 5.4)$	1.89	2.80	3.23	2.17	2.47	1.93	2.82	0.97	0.72	0.80	1.45	1.73	0.94	0.61	1.02	1.17	26.74
$[5.4, 7.9)$	0.83	2.32	3.27	1.83	0.73	0.44	1.21	0.35	0.17	0.19	0.31	0.47	0.19	0.10	0.17	0.28	12.88
$[7.9, 10.7)$	0.15	0.85	1.84	1.29	0.29	0.06	0.15	0.07	0.02	0.04	0.02	0.07	0.03	0.02	0.03	0.05	4.99
$[10.7, 13.8)$	0.05	0.24	0.86	0.86	0.11	0.01	0.02	0.02	0.	0.	0.	0.01	0.	0.01	0.01	0.02	2.24
$[13.8, 17.1)$	0.01	0.08	0.20	0.21	0.02	0	0.	0.	0	0.	0.	0.	0.	0.	0.	0.	0.54
$[17.1, 20.7)$	0.	0.01	0.02	0.02	0.	0	0	0.	0	0	0.	0	0.	0	0.	0.	0.06
$[20.7, 24.4)$	0	0	0.	0.	0	0	0	0	0	0	0	0	0.	0	0	0	0.
$[24.4, 28.4)$	0	0	0	0	0	0	0	0	0	0	0	0	0	0	0	0	0
$[28.4, 32.6)$	0	0	0	0	0	0	0	0	0	0	0	0	0	0	0	0	0
≥ 32.6	0	0	0	0	0	0	0	0	0	0	0	0	0	0	0	0	0
percent	5.96	9.59	12.80	9.51	8.50	5.81	7.55	3.28	2.72	3.15	5.43	6.41	4.68	3.83	4.37	4.31	97.92

Table 2.5: Station CHI. Table of percent frequency for each class of possible wind speed and direction. The frequency distribution of wind speed is made according to the Beaufort scale (see App. E). Wind directions are distributed in 16 sectors 22°30' wide, corresponding to the cardinal directions. Last column and last raw report the total sum of corresponding raw and column respectively. The remaining percent correspond to unrecorded or false data (2.08%) and sum of frequency less than 0.01% (0.002%). With 0. it is indicated probability less than 0.01%.

relatively good distribution, but not the best choice as compared with the other analysed PDF. It is a really good choice only for offshore wind speed.

Data independence

Before proceeding, it is essential to check the hypothesis of data independence. This is necessary because wind data are highly autocorrelated over short times. It is also important to remember that each value is the average of the previous 15 minute measurements, so consecutive data (the database frequency is 5 minutes) are strongly correlated. In the following, the results of the analysis are shown for station SAL, but similar results hold for the other stations (data not presented).

In figure 2.7 (page 86) the autocorrelation function for station SAL is reported. It is possible to see how the data are highly autocorrelated in the short time interval; autocorrelation decreases under 0.5 only after about 7 hours (sample number 79) (8 and 10 hours for CHI and PAA, respectively). There is also a small local maximum around 24 hours (sample number 288). In figure 2.8 (page 86) it is reported the autocorrelation for station SAL for increasing time step from 1 to 10 days. It is possible to see how the autocorrelation is really small, but there are periodic small local maxima in autocorrelation every 24 hours (corresponding to sample numbers: 288, 576, 864, 1152, 1440, 1728, 2016, 2304, 2592, 2880). These local maxima point out the presence of a daily structure in the wind speed distribution, basically connected to land/sea breeze.

To analyse the independence of the statistical results from the data sampling techniques, in the following it is shown a comparison among different data sampling: all data (at 5 minute frequency); data extracted (subsampling) from the database at 15, 60, 120 and 420 (i.e., 7 hours) minute frequency. The histograms of figure 2.9 (page 87) show the distributions of the wind speed data as derived from the entire dataset (5 minute sampling) and the 7 hour sub-sampling; the corresponding PDFs are plotted in figure 2.10 (page 87). In table 2.7 (page 88) it is shown the GOF of the most rele-

Station	distribution	AndersonDarling val.	AndersonDarling prob.	AndersonDarling Test	KolmogorovSmirnov val.	KolmogorovSmirnov prob.	KolmogorovSmirnov Test	PearsonChiSquare val.	PearsonChiSquare prob.	PearsonChiSquare Test	RMSE	R^2
PAA	W[1.40, 5.22, 0.087]	2.06	0.085	A	0.080	0.34	A	35.21	0.0058	R	0.011	0.95
PAA	Γ[4.06, 0.60, 0.69, −0.086]	3.33	0.019	R	0.13	0.023	R	17.76	0.47	A	0.0057	0.99
PAA	M[3.05, 2.14, 0.22]	5.90	0.0011	R	0.19	0.0001	R	25.67	0.11	A	0.0042	0.99
PAA	P[105, 56, 0.75, 0.10]	2.34	0.06	A	0.11	0.093	A	32.91	0.012	R	0.013	0.93
PAA	LN[1.30, 0.80]	7.29	0.0002	R	0.21	0.	R	76.44	0.	R	0.01	0.96
PAA	$L\Gamma$[2.79, 0.56, 0.10]	15.73	0.	R	0.30	0.	R	113.88	0.	R	0.031	0.75
PAA	EV[3.32, 2.39]	2.97	0.029	R	0.13	0.022	R	31.92	0.022	R	0.011	0.96
PAA	F[1.03, 2.41]	16.52	0.	R	0.32	0.	R	126.11	0.	R	0.027	0.79
PAA	G[6.83, 4.80]	20.73	0.	R	0.30	0.	R	173.90	0.	R	0.036	0.41
PAA	E[2, 0.41]	2.36	0.059	A	0.10	0.11	A	35.55	0.0053	R	0.0071	0.98
SAL	W[1.50, 3.5, 0.081]	3.89	0.0098	R	0.12	0.094	A	29.80	0.013	R	0.016	0.95
SAL	Γ[4.30, 0.44, 0.74, −0.097]	0.79	0.49	A	0.063	0.80	A	5.58	0.99	A	0.0082	0.98
SAL	M[2.19, 1.44, 0.16]	4.48	0.0051	R	0.18	0.0025	R	10.07	0.86	A	0.0071	0.99
SAL	P[1066, 2432, 0.73, 0.10]	0.76	0.54	A	0.063	0.80	A	10.36	0.80	A	0.022	0.91
SAL	LN[0.95, 0.74]	8.16	0.0001	R	0.24	0.	R	46.13	0.0001	R	0.015	0.96
SAL	$L\Gamma$[2.27, 0.57, 0.10]	19.74	0.	R	0.4	0.	R	106.069	0.	R	0.051	0.70
SAL	EV[2.31, 1.55]	1.91	0.10	A	0.10	0.23	A	9.90	0.87	A	0.012	0.97
SAL	F[1.10, 1.75]	19.78	0.	R	0.41	0.	R	106.93	0.	R	0.039	0.79
SAL	G[4.52, 3.14]	20.20	0.	R	0.38	0.	R	154.74	0.	R	0.048	0.47
SAL	E[2, 0.61]	0.74	0.53	A	0.054	0.92	A	11.18	0.74	A	0.014	0.96
CHI	W[1.56, 4.30, 0.068]	2.69	0.039	R	0.09	0.33	A	31.40	0.011	R	0.034	0.76
CHI	Γ[2.06, 2.08, 1.09, −0.041]	1.09	0.31	A	0.072	0.61	A	18.78	0.34	A	0.033	0.79
CHI	M[2.66, 1.73, 0.13]	4.11	0.0077	R	0.17	0.0029	R	28.71	0.037	R	0.033	0.81
CHI	P[1335, 2853, 0.73, 0.10]	1.83	0.11	A	0.081	0.46	A	22.06	0.14	A	0.037	0.73
CHI	LN[1.14, 0.74]	8.25	0.0001	R	0.22	0.	R	53.66	0.	R	0.038	0.76
CHI	$L\Gamma$[2.24, 0.64, 0.10]	18.28	0.	R	0.37	0.	R	105.46	0.	R	0.059	0.58
CHI	EV[2.81, 1.83]	0.80	0.48	A	0.068	0.69	A	12.55	0.77	A	0.032	0.81
CHI	F[1.05, 2.11]	18.13	0.	R	0.37	0.	R	116.36	0.	R	0.051	0.62
CHI	G[5.39, 3.57]	16.56	0.	R	0.29	0.	R	159.44	0.	R	0.047	043
CHI	E[2, 0.51]	2.92	0.030	R	0.10	0.18	A	27.83	0.033	R	0.035	0.76

Table 2.6: Parameters of the tested PDF and statistical GOF for wind speed. It is used the entire database of the three stations. "0." means less than 10^{-6}.

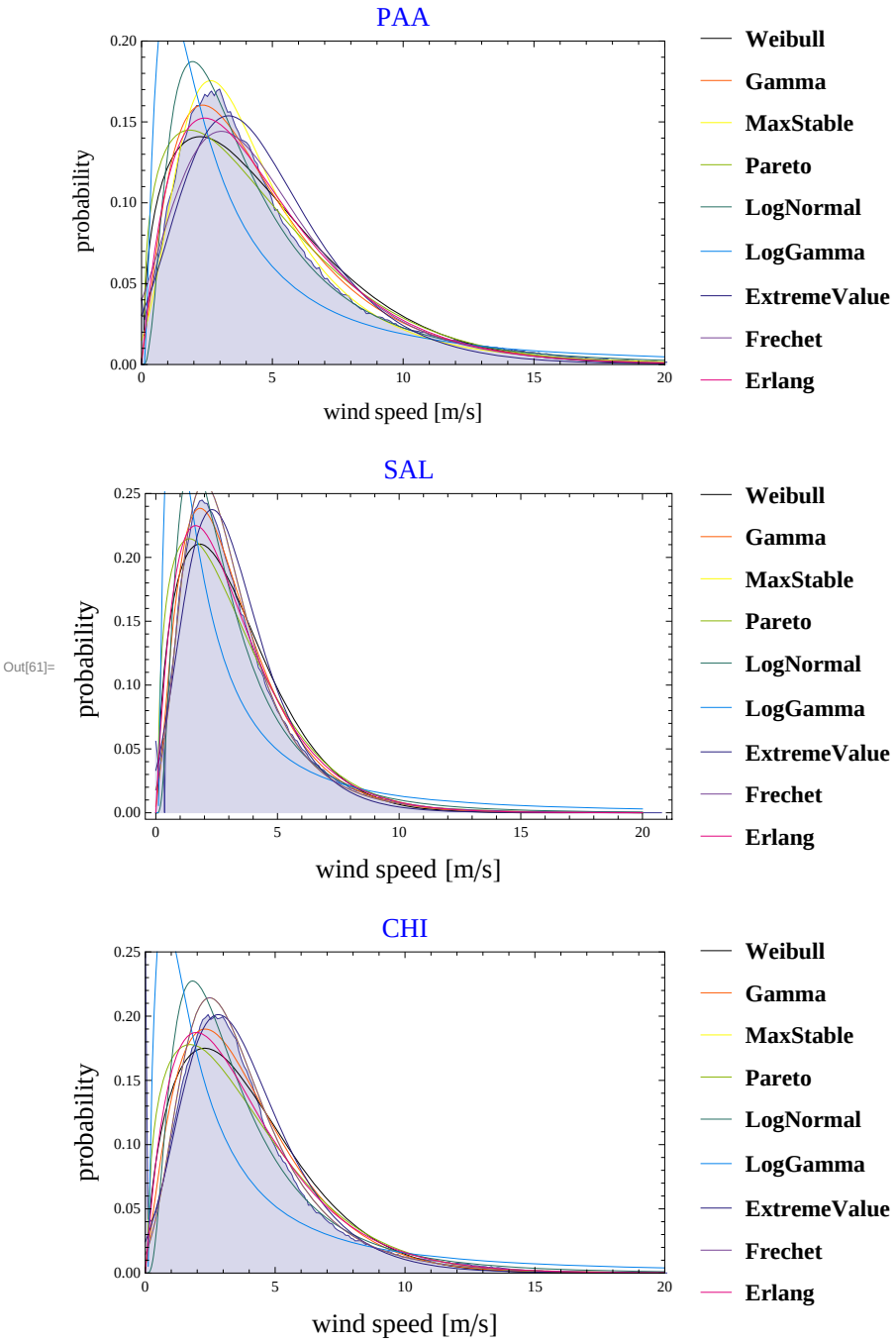

Out[61]=

Figure 2.3: Histograms of the entire dataset (wind speed) for the three stations with the calculated PDF.

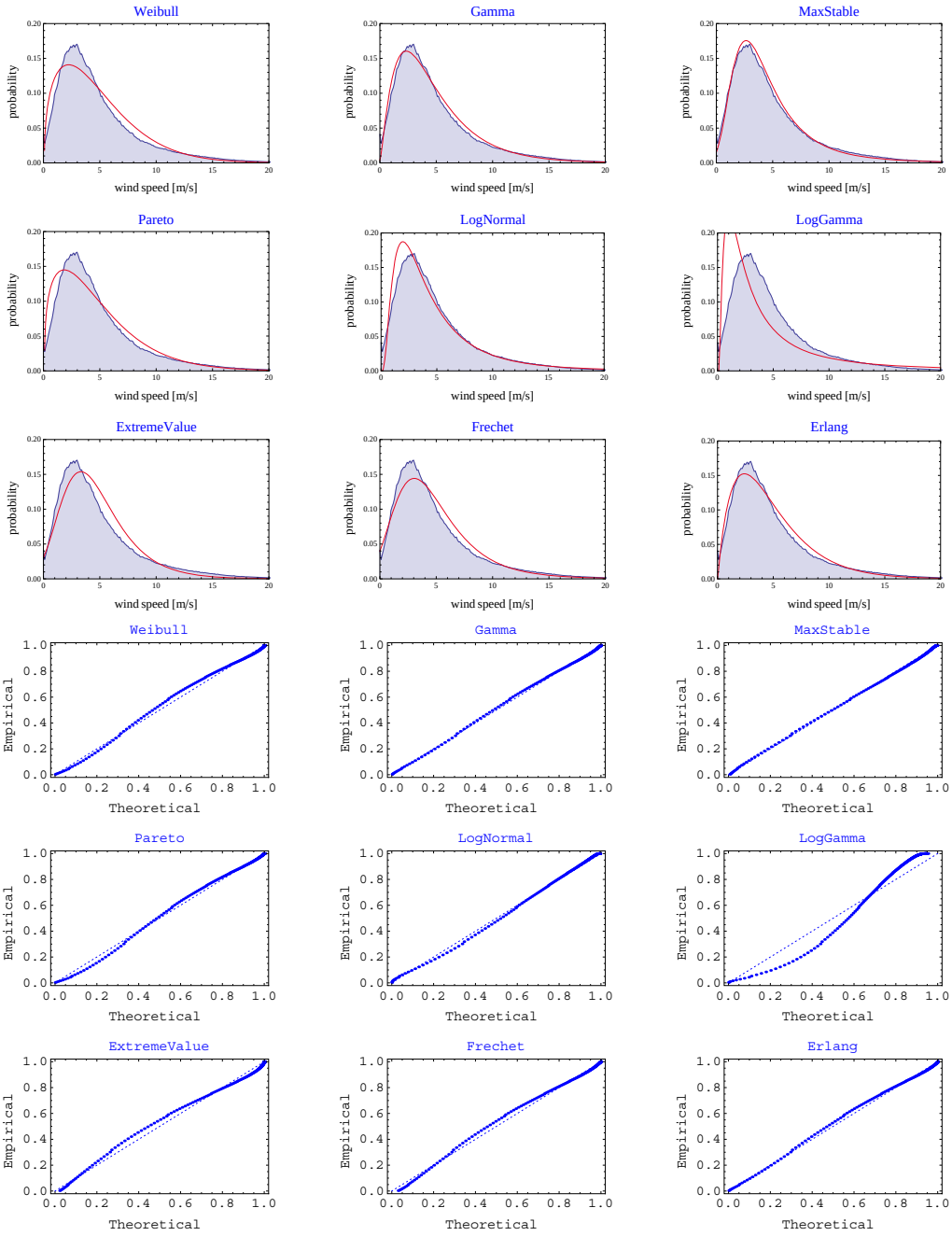

Figure 2.4: PAA station wind speed: histograms of the entire dataset and the calculated PDFs (top); PP-plots of the calculated PDFs (bottom)

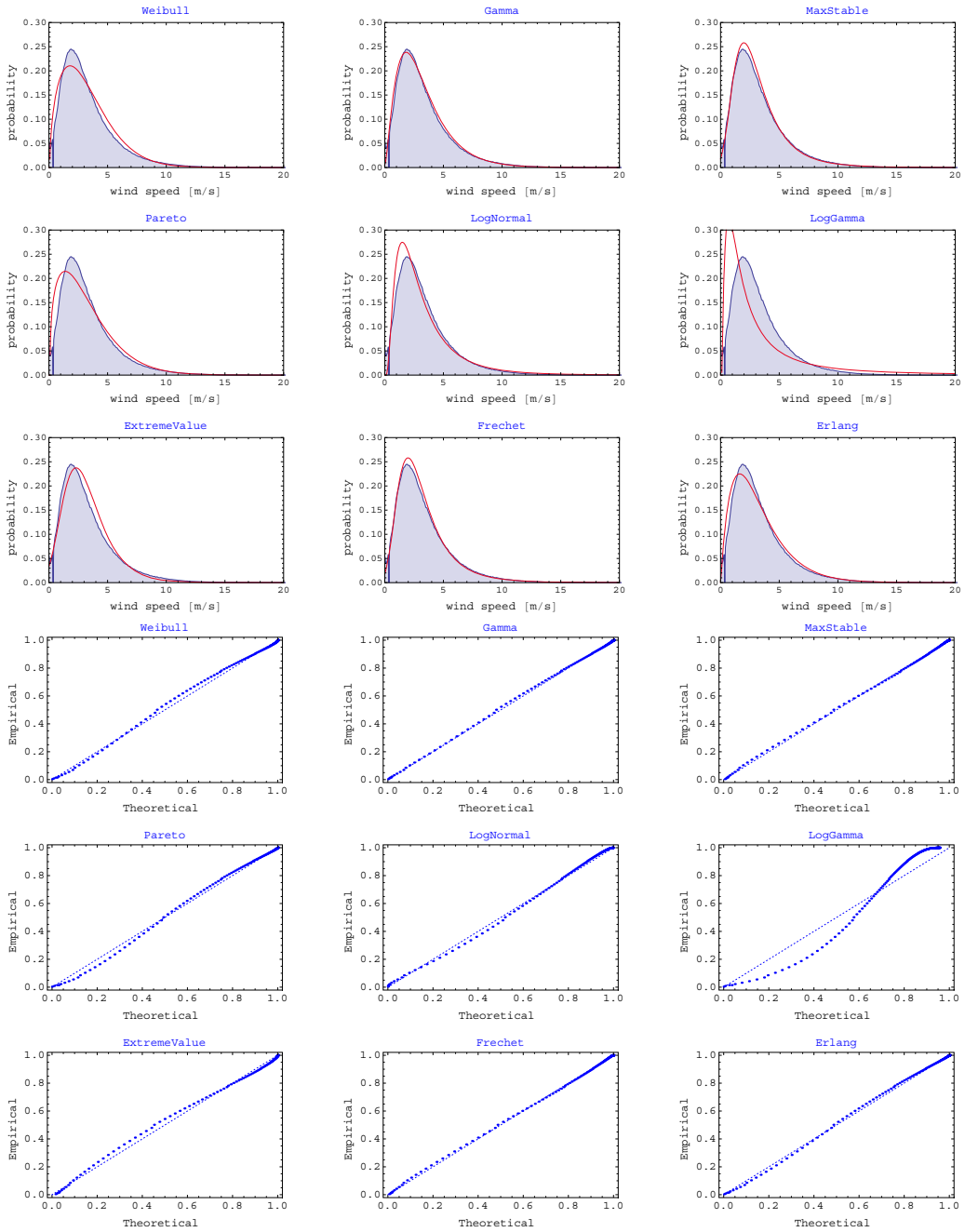

Figure 2.5: SAL station wind speed: histograms of the entire dataset and the calculated PDFs (top); PP-plots of the calculated PDFs (bottom)

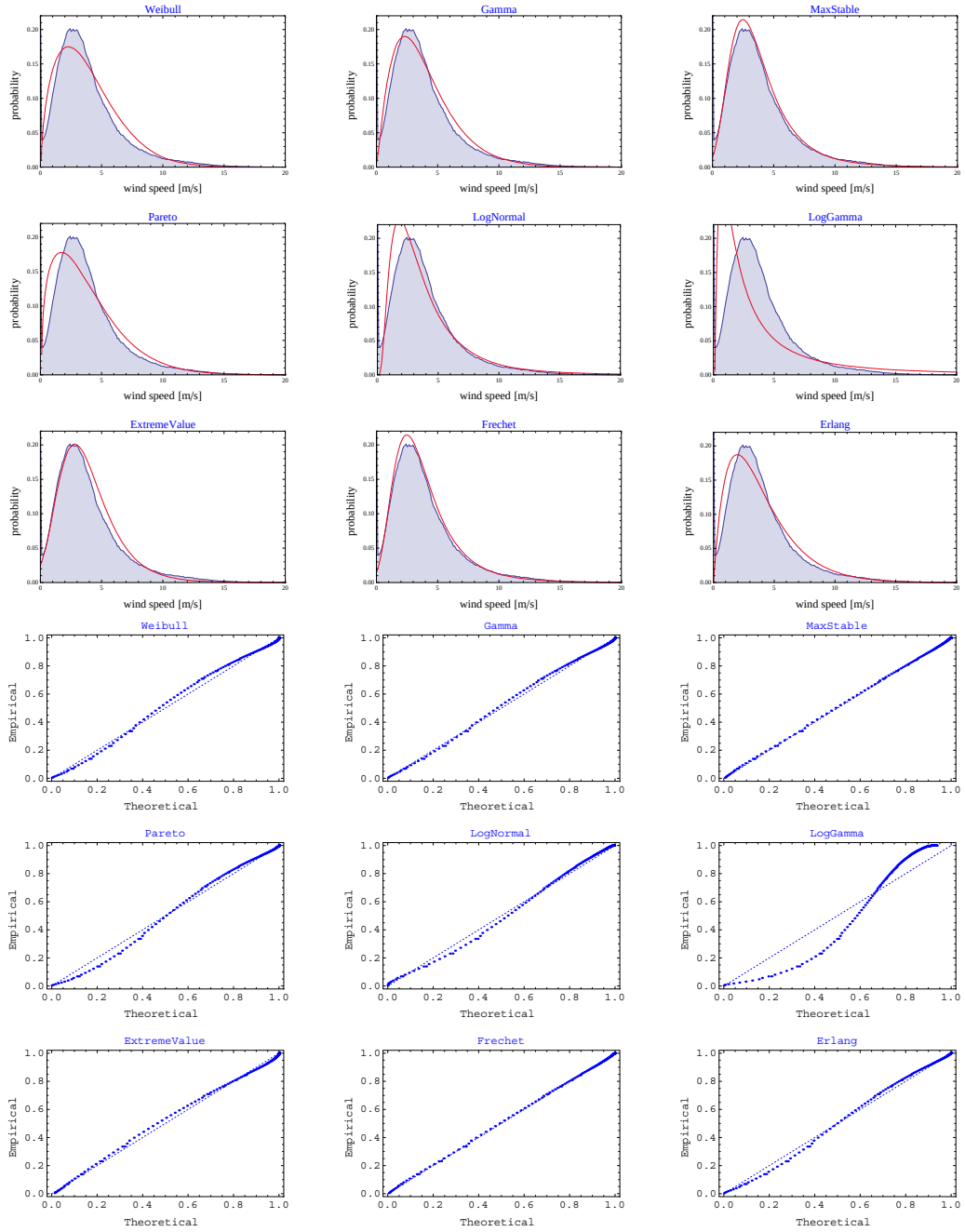

Figure 2.6: CHI station wind speed: histograms of the entire dataset and the calculated PDFs (top); PP-plots of the calculated PDFs (bottom)

vant PDFs. It is clear that, even if there are some differences, for each PDF the results are very similar and that there are no major differences between the PDF calculated for the entire dataset and those obtained from its subsets, even with 420 minute frequency. In the following analyses are thus only performed on the entire dataset, to take advantage of the greater statistical significance.

Yearly statistics

All the stations show a weak variation among years, with variation of the yearly-mean wind speed of about 0.5 m/s (see figure 2.11, top panel on page 89). With some exceptions, it seems that the yearly variations are similar for all the stations. Years 2002, 2006 and 2011 are the less windy years; 2010 is the most windy year.

Hourly statistics

Looking at figures 2.12-2.17 (pages 96-101), it is evident how wind is variable from year to year, even if the main field structure remains the same, with a dominant wind from the first quadrant and a second important component in the second quadrant. However it seems that there is a small anticlockwise rotation of the dominant and secondary wind of at least 22°; this is more noticeable comparing the years before and after 2004. This generalized rotation agrees with what is reported in Massalin and Canestrelli ([41]).

In the Northern part of the lagoon, the general rotation of wind direction is associated with a rise in importance for wind of the fourth quadrant, more evidently starting from 2006. In particular, in 2011 the wind from NW and NNW gives a contribution greater than 15%, whereas before 2006 the wind from this direction was less than 5%.

In the Southern part of the lagoon, in the years 2004-2006 there was an homogeneous distribution of dominant wind from NNE to E; starting from 2007, North-Easterly winds become more important. In the same year there was a reduction in the frequency of wind occurrence from the third quadrant

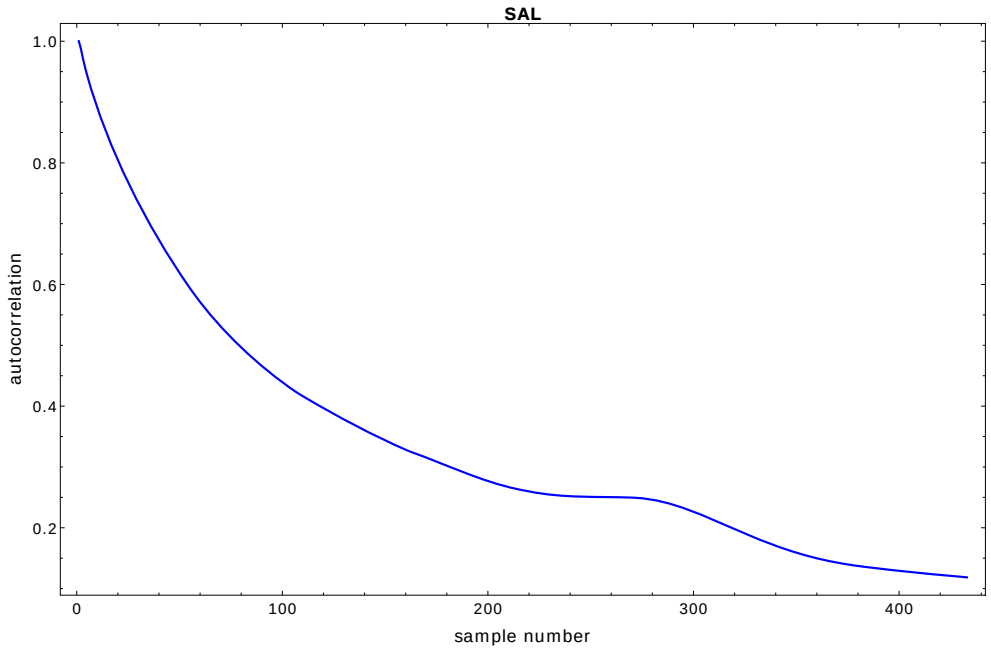

Figure 2.7: SAL station wind speed autocorrelation diagram: from 0 to 36 hour data shift.

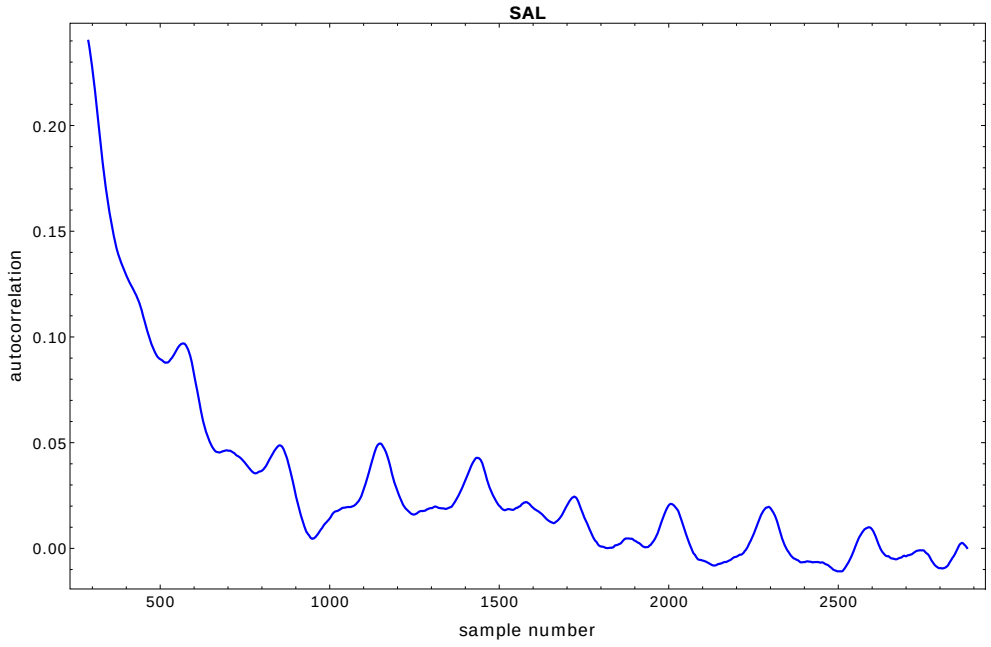

Figure 2.8: SAL station wind speed autocorrelation diagram: from 1 to 10 day data shift.

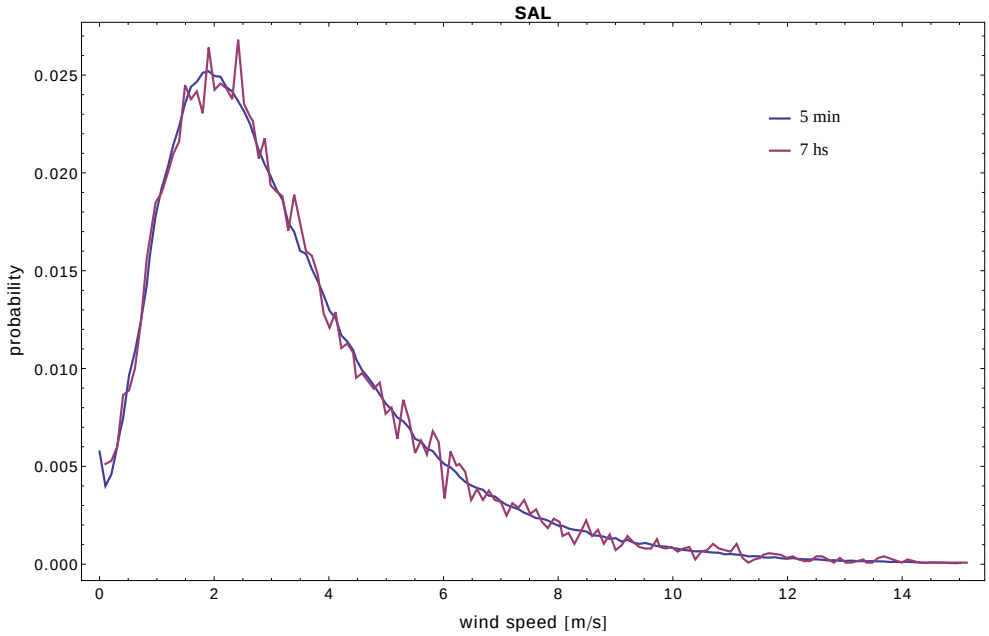

Figure 2.9: SAL station wind speed histograms: entire dataset compared with 7 hour sub-sampling.

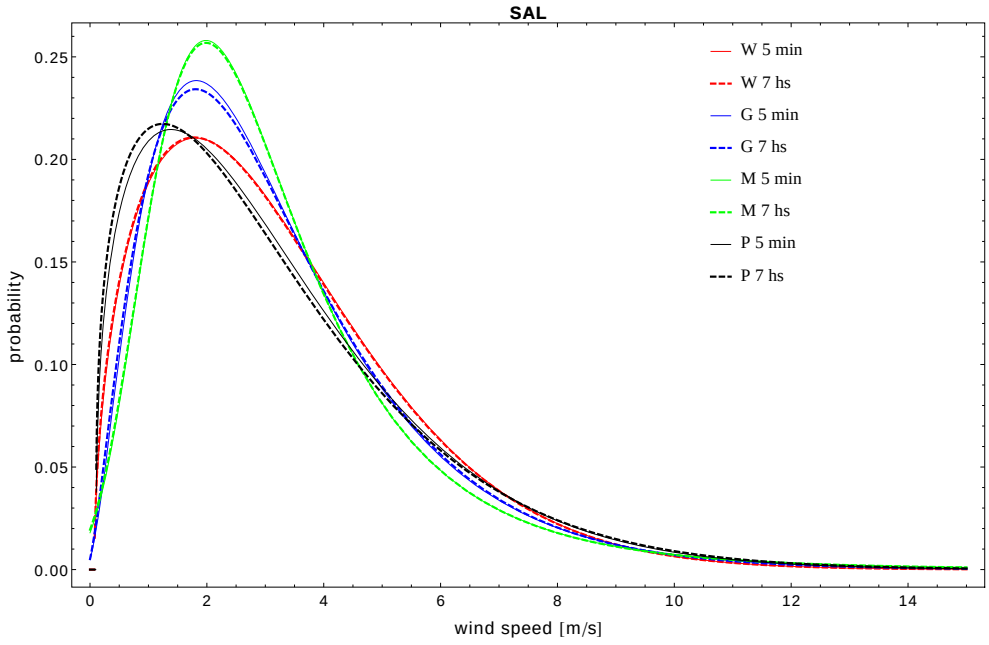

Figure 2.10: SAL station wind speed PDFs: entire dataset compared with 7 hour sub-sampling for the most relevant PDFs.

Frequency	distribution	AndersonDarling			KolmogorovSmirnov			PearsonChiSquare			RMSE	R^2
		val.	prob.	Test	val.	prob.	Test	val.	prob.	Test		
5min	W	3.89	0.010	R	0.12	0.094	A	29.80	0.013	R	0.016	0.95
15min	W	3.61	0.014	R	0.13	0.062	A	35.13	0.004	R	0.016	0.96
60min	W	3.68	0.013	R	0.15	0.026	R	38.52	0.001	R	0.014	0.96
120min	W	3.73	0.012	R	0.17	0.015	R	33.55	0.002	R	0.015	0.96
420min	W	2.70	0.039	R	0.16	0.043	R	36.08	0.001	R	0.016	0.96
5min	G	0.79	0.49	A	0.063	0.80	A	5.58	0.99	A	0.0082	0.99
15min	G	0.84	0.45	A	0.077	0.61	A	3.07	0.99	A	0.0068	0.99
60min	G	0.20	0.99	A	0.050	0.98	A	4.49	0.99	A	0.0055	0.99
120min	G	0.27	0.96	A	0.046	0.99	A	5.63	0.98	A	0.0074	0.99
420min	G	0.83	0.46	A	0.099	0.44	A	20.97	0.10	A	0.0094	0.99
5min	P	0.73	0.54	A	0.063	0.80	A	10.36	0.80	A	0.022	0.91
15min	P	0.77	0.50	A	0.072	0.61	A	11.98	0.75	A	0.022	0.91
60min	P	1.48	0.18	A	0.093	0.40	A	20.69	0.19	A	0.019	0.94
120min	P	1.72	0.13	A	0.10	0.30	A	20.15	0.13	A	0.018	0.94
420min	P	1.05	0.33	A	0.092	0.53	A	22.85	0.063	A	0.025	0.90
5min	M	4.48	0.005	R	0.18	0.002	R	10.07	0.86	A	0.0072	0.99
15min	M	3.74	0.012	R	0.15	0.020	R	7.16	0.97	A	0.0066	0.99
60min	M	2.35	0.059	A	0.12	0.19	A	8.98	0.91	A	0.0058	0.99
120min	M	1.78	0.12	A	0.10	0.30	A	7.50	0.94	A	0.0073	0.99
420min	M	0.48	0.76	A	0.086	0.62	A	14.68	0.40	A	0.0079	0.99

Table 2.7: SAL - GOF for different sampling techniques: one datum every 5, 15, 60, 120 and 420 minutes (each mean of the previous 15 minute measurement).

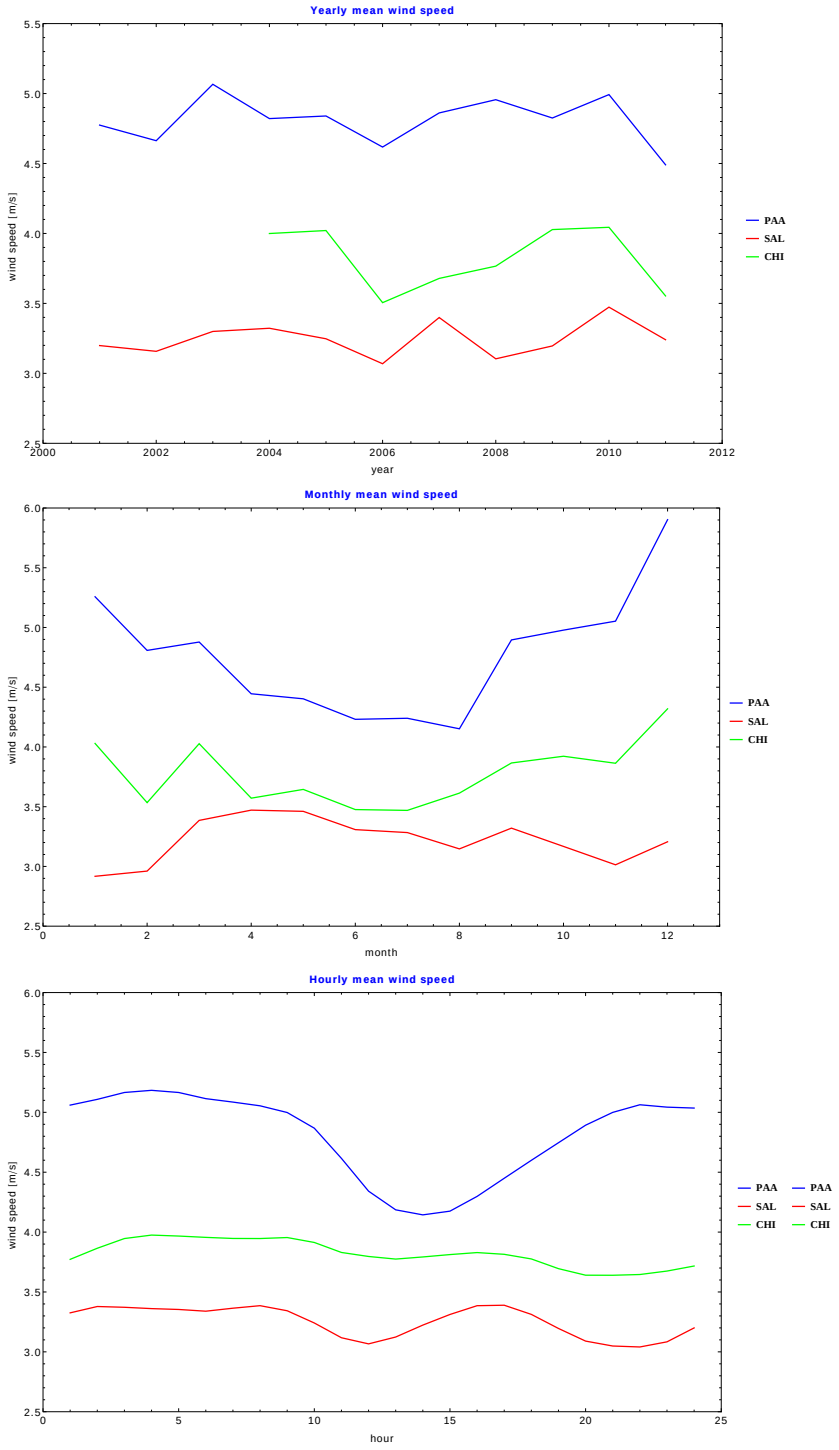

Figure 2.11: Wind speed means: yearly (top), monthly (middle) and hourly (bottom).

and a homogenization of Scirocco wind, from a SE dominant component to a uniform distribution from ESE to SSE. Starting from 2007 CHI sees an increase in wind speed, with maximum in 2008.

Seasonal statistics

Seasonal analysis are made for the following seasons: winter (January to March); spring (April to June); summer (July to September) and autumn (October to December). In figures 2.18-2.20 (pages 102-104) the rose plots of seasonal analysis are shown. It is clear that the windier seasons are winter and autumn.

PAA and SAL show an homogeneous wind presence in third and forth quadrant for winter and autumn, whereas they are marginal in spring and summer. For the same stations the figures point out an important presence of Scirocco in spring and summer. Scirocco is a marginal wind in winter and autumn in PAA, but it is present in winter in SAL. It is to be noticed that for SAL, Scirocco is as frequent as Bora in spring; in all other situations Bora is the clear dominant wind, both in frequency and velocity.

The results for CHI shows a quite different situation. In winter there is a dominance of the first quadrant, with a relatively important contribution in the third quadrant. In spring and summer the wind is principally in the first and second quadrant. In autumn wind distribution is homogeneous in all quadrants except the second. In this station Bora is not as dominant as in the other stations. Only in the year average is Bora a dominant wind for CHI, as, differently from other wind directions, it is present in all the seasons with about the same frequency.

Monthly statistics

Figure 2.11 (middle panel, page 89) shows some basic characterization of the monthly mean wind speeds. In the open sea, monthly changes are dominated by the presence or absence of strong events, typically of Bora, that mainly occur in winter and autumn. On the contrary, the Northern

lagoon is dominated by sea-land breezes, which have an important effect in spring and summer. An intermediate situation characterizes the Southern lagoon, where both breezes and strong events play a relevant role.

As it can be seen in figures 2.21-2.26 (pages 105-110), for the studied area there is a clear and important variation of the wind field during the year. Starting from February, and until May, there is an increase in wind from the second quadrant and a decrease in wind from first and second quadrants. In June and July the wind field is quite stable; from August to November there is a decrease in wind from the second quadrant and an increase for the other sectors. In December and January the wind from E to SSW are negligible.

It should be noticed that August-October exhibits the highest Bora occurrence, even more frequent than in Winter; however wind speed is low, whereas in Winter Bora events are much more intense. This frequent presence of low-speed Bora during Summer is probably connected to sea-land breezes.

In the open sea (PAA) the strongest events are concentrated between December and March, with a maximum in December for the higher wind speed from ENE (about than 7% of wind speed greater than 13.8 m/s). A similar distribution is seen in CHI, but the frequency of wind speed greater than 13.8 m/s from ENE is about 3%.

In the Northern lagoon the highest probability (less than 2%) of $v > 10.7$ m/s is concentrated in February, March and November. This station is alwayes dominated (at least 70%, up to 81%) by wind speeds less than 5.4 m/s.

Hourly statistics

Analyses at the daily scale show daily patterns in wind occurrence. Figure 2.11 (bottom panel on page 89) shows that high wind conditions generally happen between 8 pm and 10 am in the open sea, and between 12 pm and 8 am in the lagoon; there is a maximum probability of low wind around 2 pm in the open sea, while inside the lagoon there are two minima, around 12 am

and 10 pm. The variations in mean speed during the day are about 1m/s in the open sea and about 0.33 and 0.28 m/s for SAL and CHI respectively.

The distribution of wind directions for each hour of the day are shown in figures 2.27-2.32 (pages 111-116). From 4 am wind from the first quadrant is dominant (frequency greater than 60%). Later, a clockwise rotation takes place around 10 am and from 3 pm the second quadrant becomes dominant; Starting from 8 pm there is an increase in wind frequency from the third and fourth quadrants; around 10 pm Southerly winds are dominant. From 1 am to 5 am the wind from the fourth quadrant is stable, and then decreases until 5 pm. In summary, an overall clockwive rotation of wind direction takes place during the day. This rotation is due to sea-land breezes.

The rotation of the dominant wind during the day occurs at all stations, but it is more evident at PAA and SAL. At CHI the rotation is more complicated because of the specific morphology of the area. In particular, the breezes are more intense and from about 1 pm there is a strong dominance of the breeze wind that rotates from E to SW, decreasing in intensity with time. This rotation confirm what was found by Massalin and Canestrelli ([41]). There are other literature contributions that analyse breeze wind in the North Adriatic sea, but they focus on the East coast, where both clockwise and anticlockwise rotations are found, due to local orography ([42] and [43]).

2.4.2 Power density probability distribution

The results of the analysis of power density distribution (eq. 2.57) are summarized in Table 2.8 (page 95), where the parameters of the tested PDF and of the statistical GOF are listed. Calculated wind power histograms and analysed PDFs are reported in Figure 2.33 (page 117). The table and figures show wide departures between PDFs, particularly as compared to the results for the wind speed PDFs (see tab. 2.6 on page 80 and fig. 2.3 on page 81). In this case, the Weibull distribution performs consistently well and comparably to the Gamma distribution.

It should be noticed that the direct use of eq. 2.57 with the best PDF for wind speed does not give good results to represents wind power density. As plotted in figure 2.34 the power density distribution derived by the use of the best PDF calculated for wind speed underestimates the actual power density distribution. Even if the original PDF is quite good, in the equation the wind speed is elevated to the third power, consequently any small error in the middle-high tail of the distribution is amplified. For this reason, whenever it is necessary to use a PDF to calculate wind power, it is better to choose a PDF that is a good approximation of the medium-high tail of the distribution, even if it does not accurately reproduce lower wind speeds.

2.5 Summary and conclusions

A 5-minute resolution, 11-year long, wind dataset from the Venice lagoon has been analysed. This is the first analysis based on such a high-resolution and extensive data set performed for this area.

The analysis considers the spatial dependence of statistical characteristics, comparing wind regimes in different parts of the lagoon and in an offshore site. The wind inside the lagoon is, not unexpectedly, found to be weaker than in the nearby sea, and the Southern part of the lagoon turns out to be windier than the Northern one. The whole region is dominated by Bora, both in intensity and frequency. Scirocco, mostly connected to sea-land breeze regimes, is the second most frequent wind. The windiest months are in autumn and winter (November to March), with maximum wind events in December. The sea-land breezes start in February and end in November, with a stable and strong presence in June and July. The sea-land breezes follow a clockwise rotation. There is a maximum variation in yearly mean wind speed of about 0.5 m/s in the analysed period (2001-2011). It has been noticed a generalised anticlockwise rotation of the yearly wind fields of about 22°in 11 years.

The analysis of wind speed probability distributions points out that gen-

erally the GEV family gives good fits. Other candidate PDFs to describe wind velocity are the Pareto, Gamma and Erlang distributions.

Station	distribution	AndersonDarling			KolmogorovSmirnov			PearsonChiSquare			RMSE
		val.	prob.	Test	val.	prob.	Test	val.	prob.	Test	
SAL	W[1.92,7.54,1.47]	0.83	0.46	A	0.073	0.64	A	4.58	0.99	A	0.15
SAL	Γ[1.34,6.37,1.66,1.23]	0.80	0.48	A	0.063	0.81	A	10.38	0.73	A	0.14
SAL	M[6.51,3.29,-0.017]	3.65	0.0135	R	0.15	0.033	R	27.97	0.032	R	0.24
SAL	P[44.88,32.74,0.51,1.45]	0.86	0.44	A	0.073	0.64	A	9.44	0.80	A	0.15
SAL	LN[2.073,0.52]	2.12	0.079	A	0.14	0.044	R	42.16	0.00021	R	0.35
SAL	LG[92.71,0.029,-5.14]	3.20	0.023	R	0.13	0.057	A	19.90	0.23	A	0.23
SAL	EV[6.52,3.30]	3.78	0.011	R	0.14	0.033	R	28.78	0.026	R	0.24
SAL	F[$8.09 * 10^7$,$2.67 * 10^8$,$-2.67 * 10^8$]	3.79	0.011	R	0.14	0.033	R	28.78	0.026	R	0.24
SAL	G[8.27,3.70]	4.46	0.0052	R	0.17	0.0050	R	44.24	0.00018	R	0.94

Table 2.8: Parameters of the tested PDF for wind power density distribution. It is used the entire database of SAL station

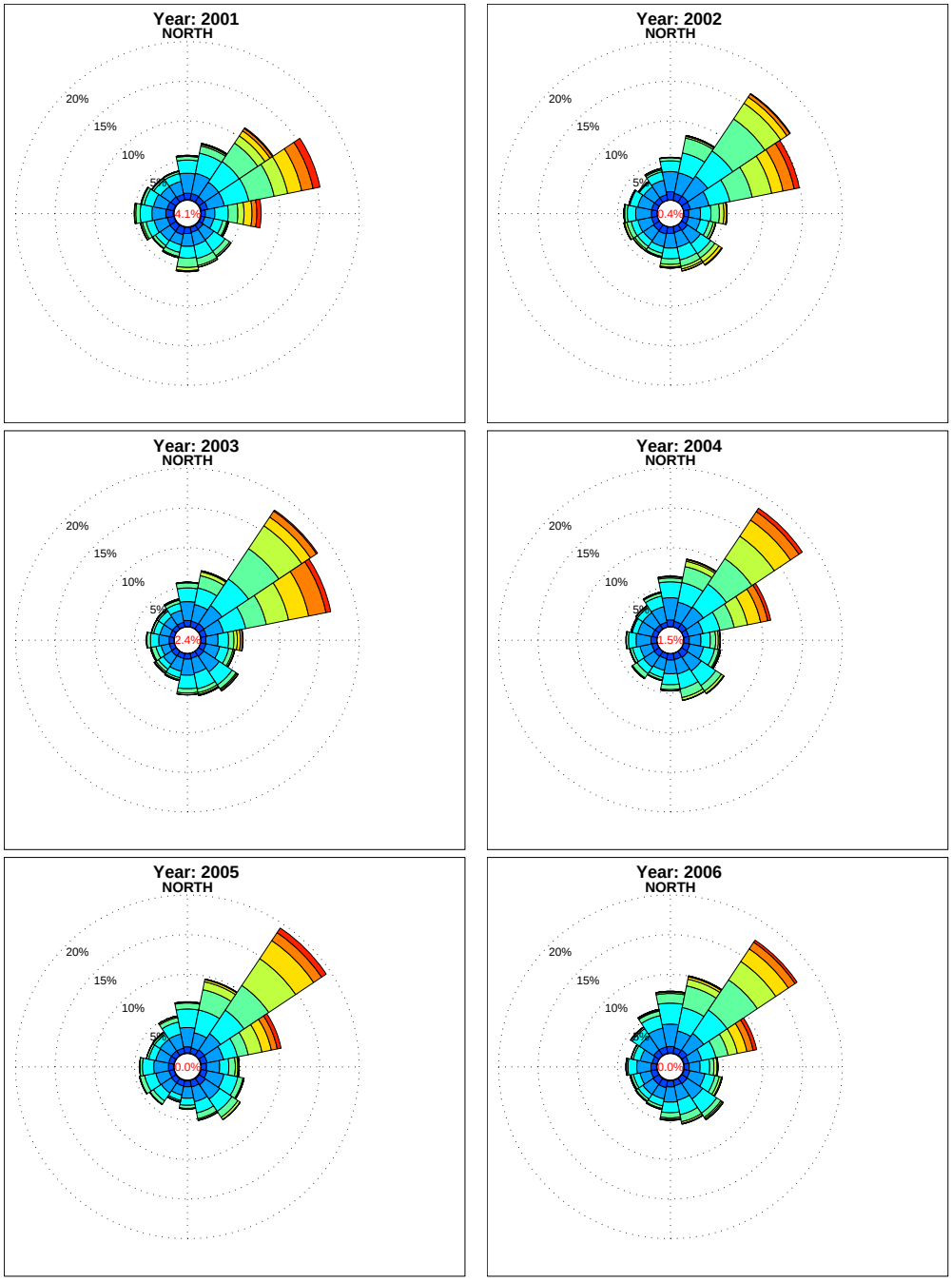

Figure 2.12: Wind rose for each year of the database. Station: PAA

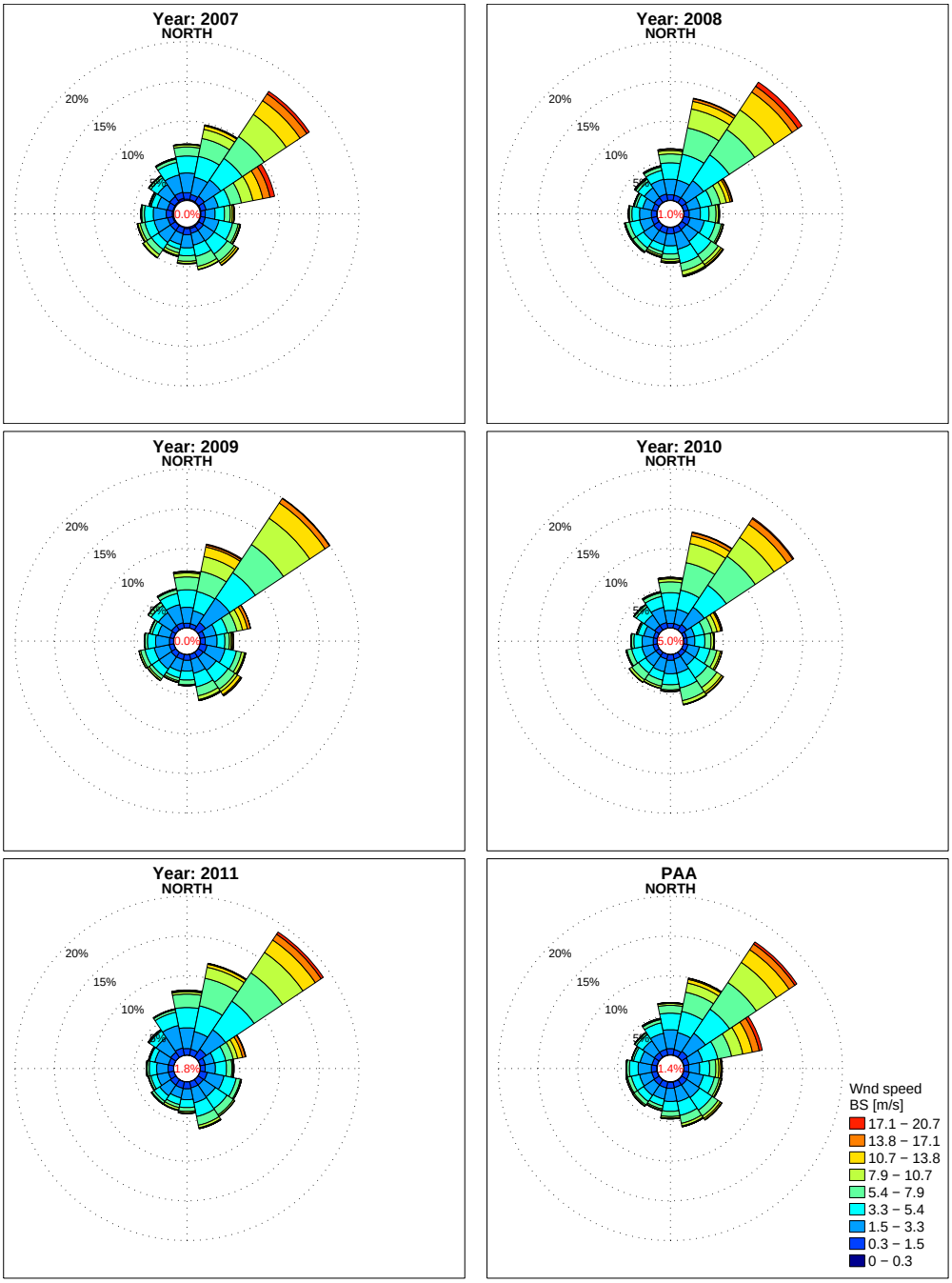

Figure 2.13: Wind rose for each year of the database. Station: PAA

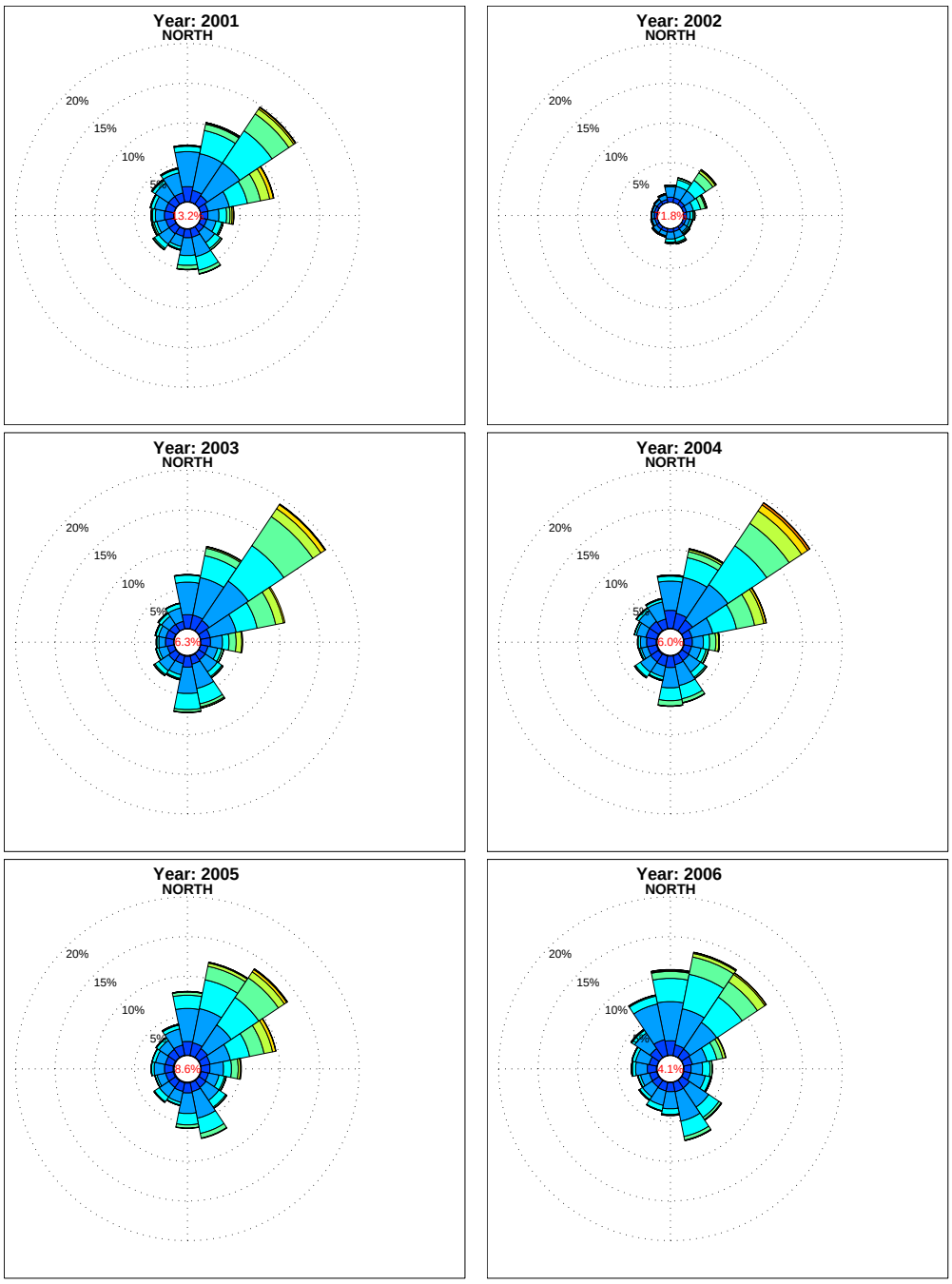

Figure 2.14: Wind rose for each year of the database. Station: SAL

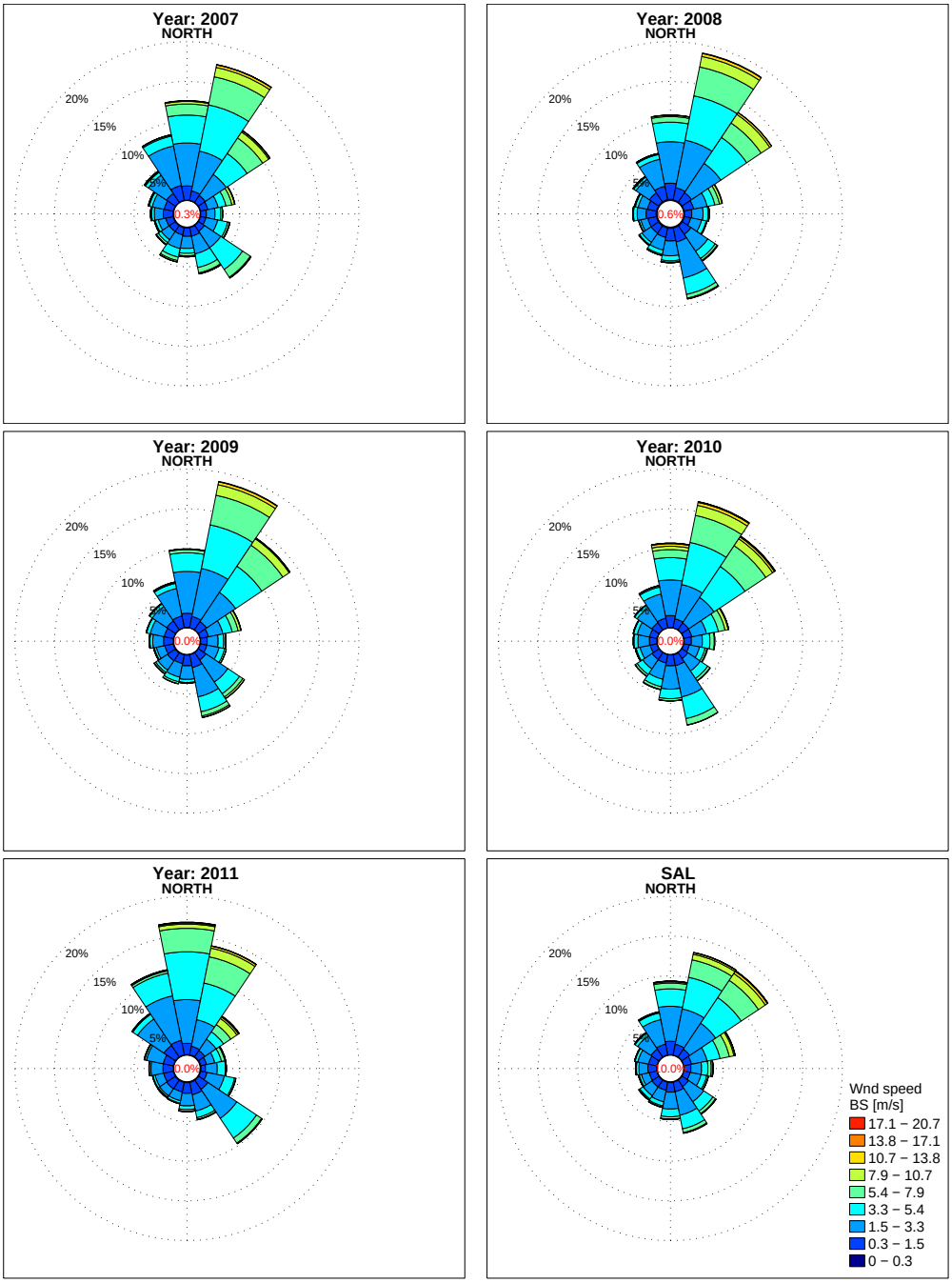

Figure 2.15: Wind rose for each year of the database. Station: SAL

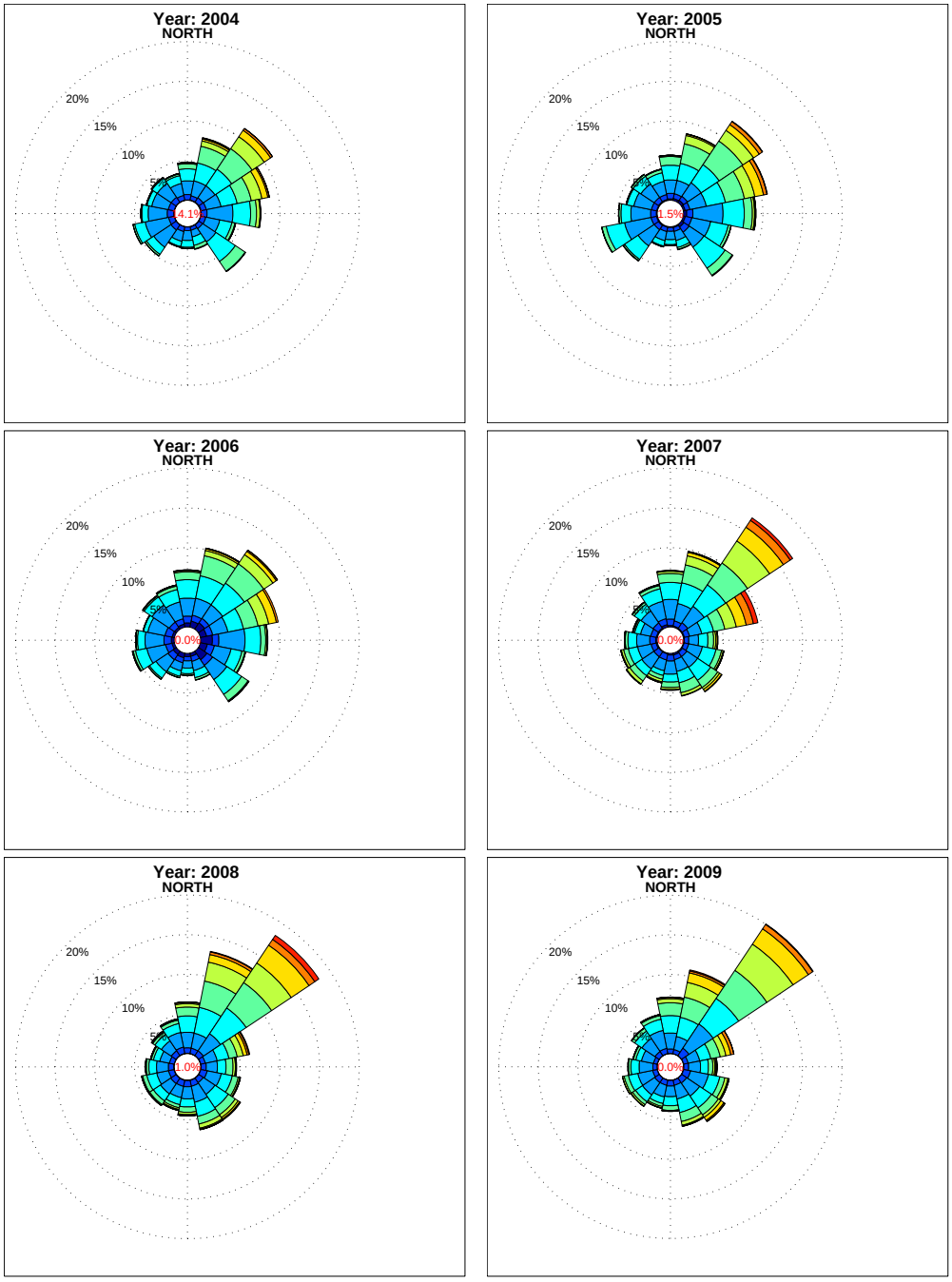

Figure 2.16: Wind rose for each year of the database. Station: CHI

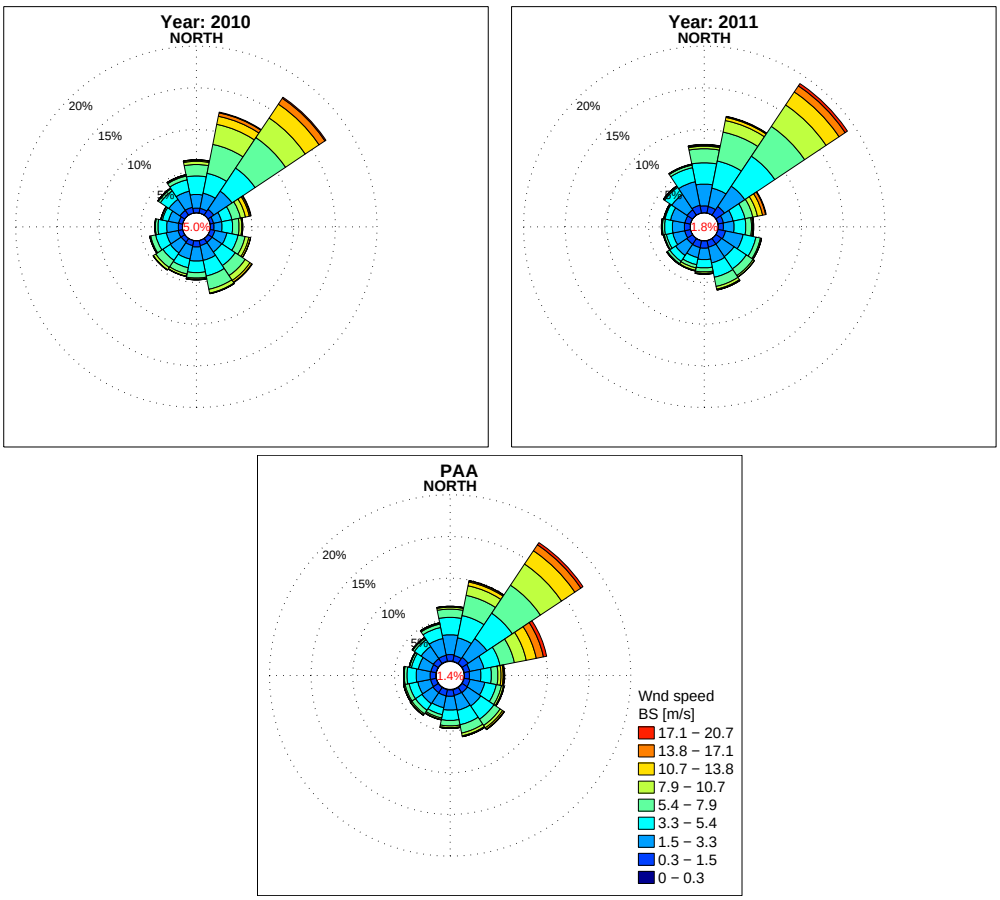

Figure 2.17: Wind rose for each year of the database. Station: CHI

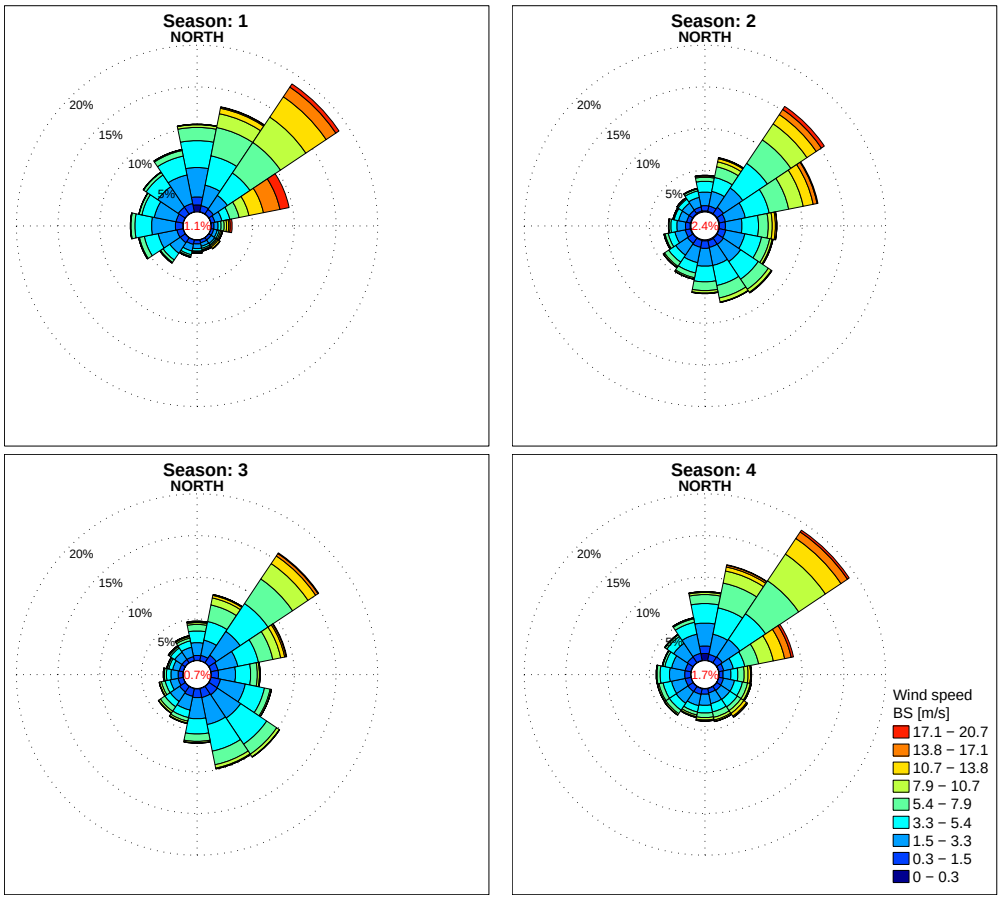

Figure 2.18: Wind rose for seasonal evolution of mean wind speed, starting from Winter. Station: PAA

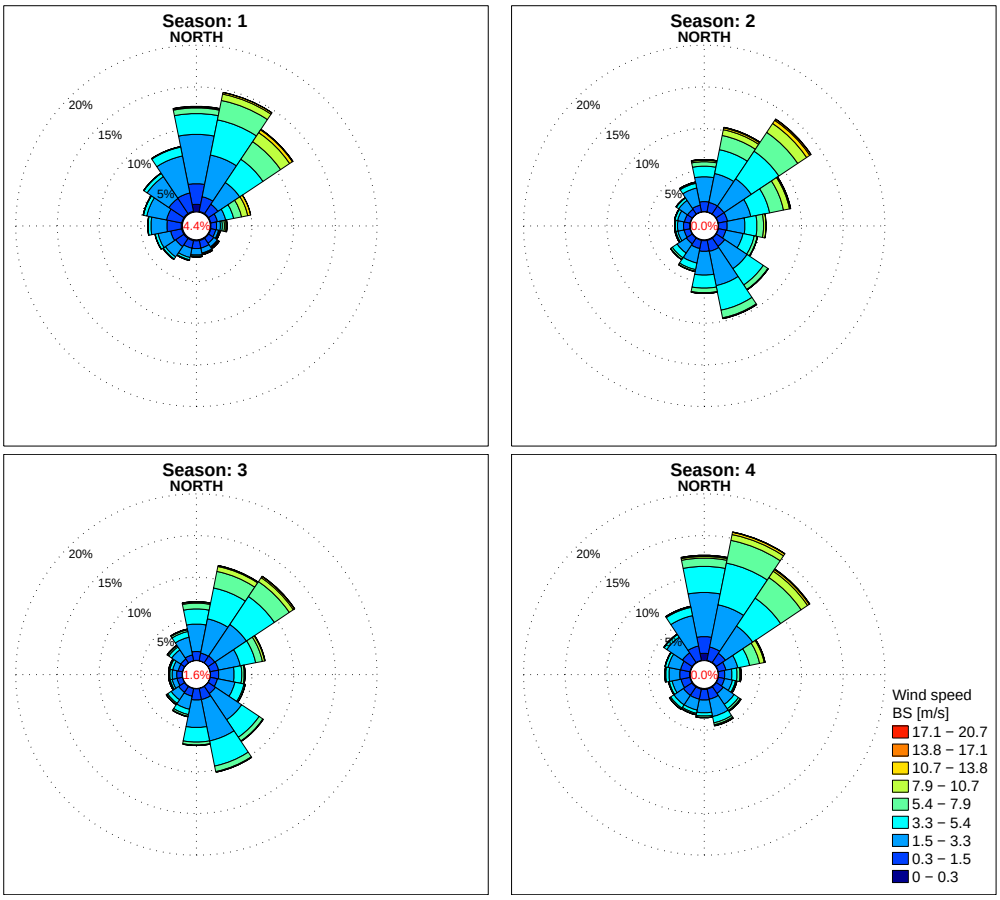

Figure 2.19: Wind rose for seasonal evolution of mean wind speed, starting from Winter. Station: SAL

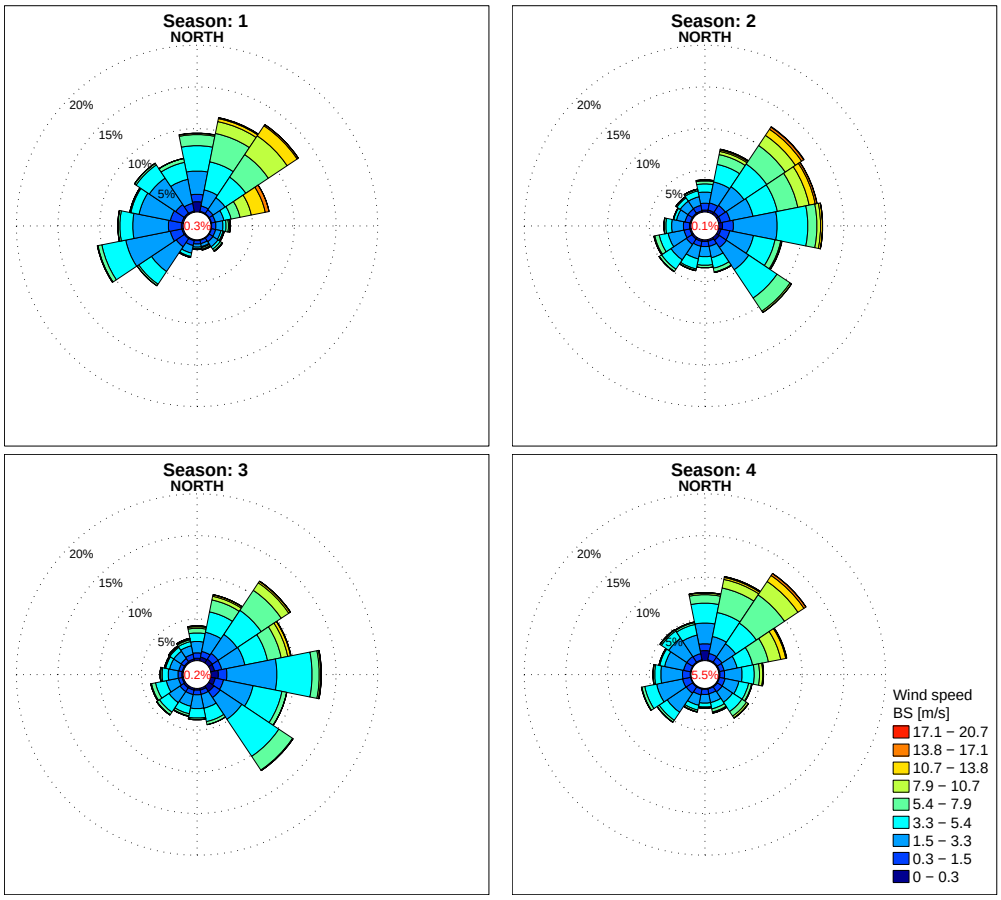

Figure 2.20: Wind rose for seasonal evolution of mean wind speed, starting from Winter. Station: CHI

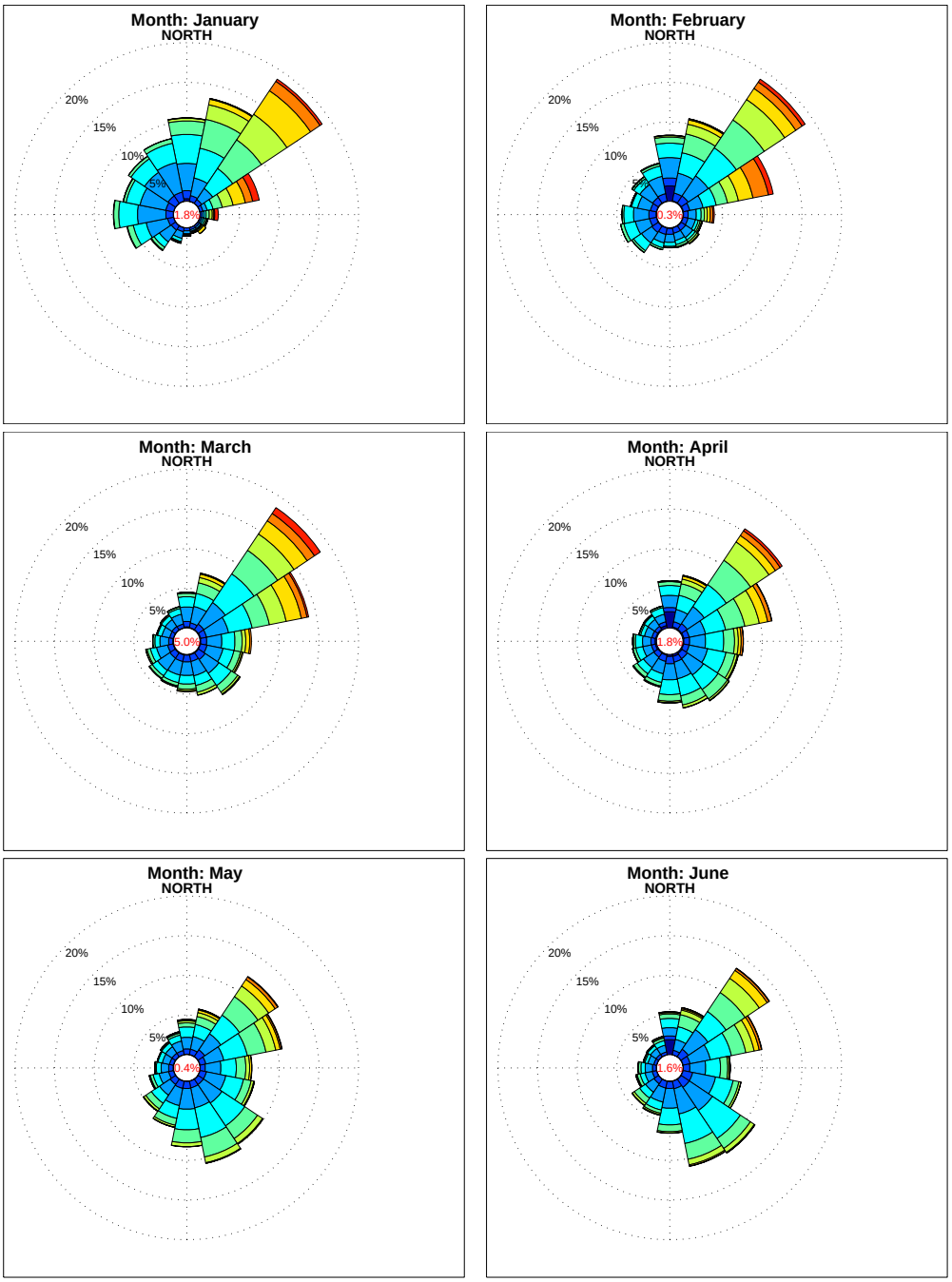

Figure 2.21: Wind rose for monthly evolution of mean wind speed. Station: PAA

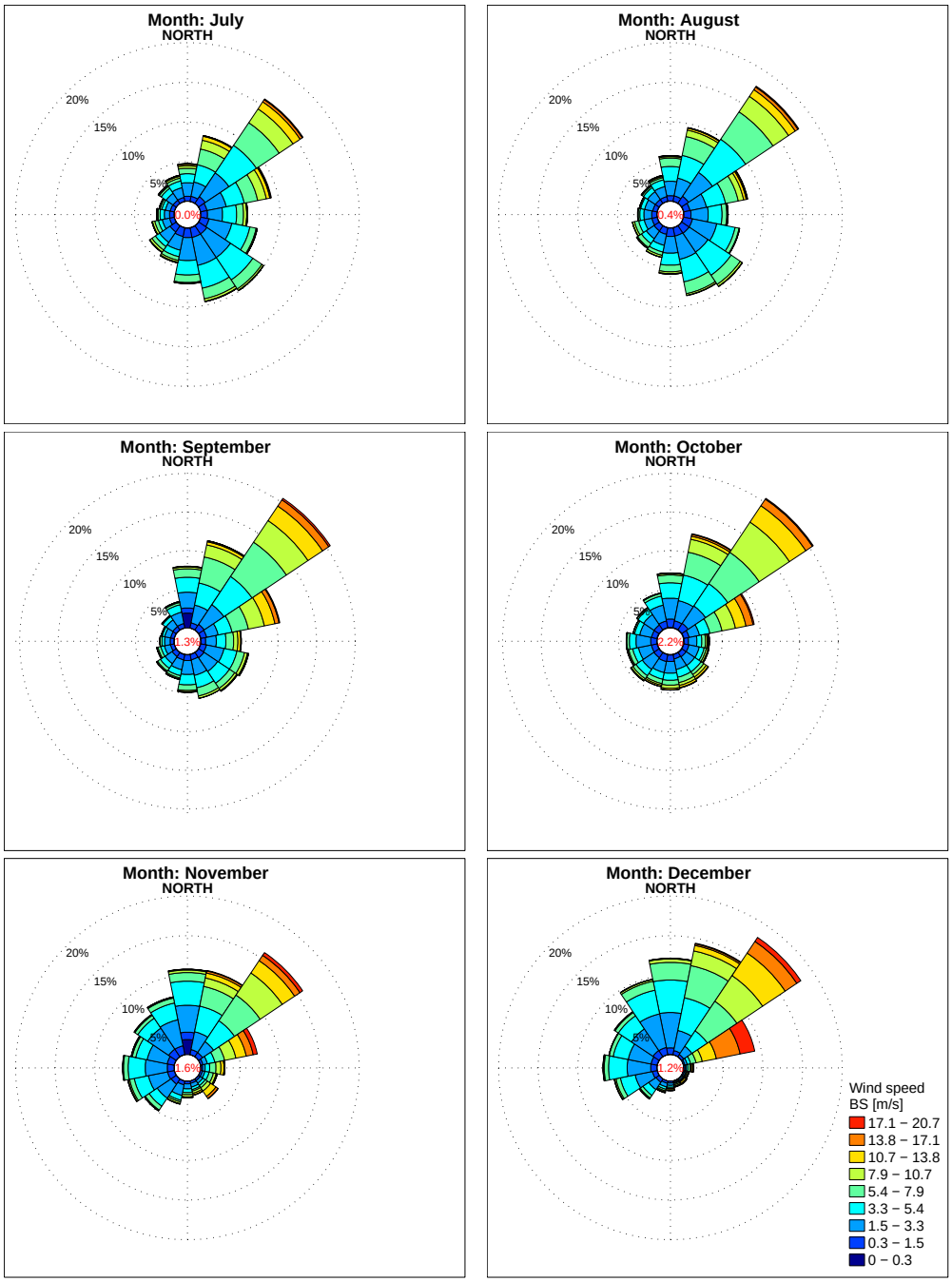

Figure 2.22: Wind rose for monthly evolution of mean wind speed. Station: PAA

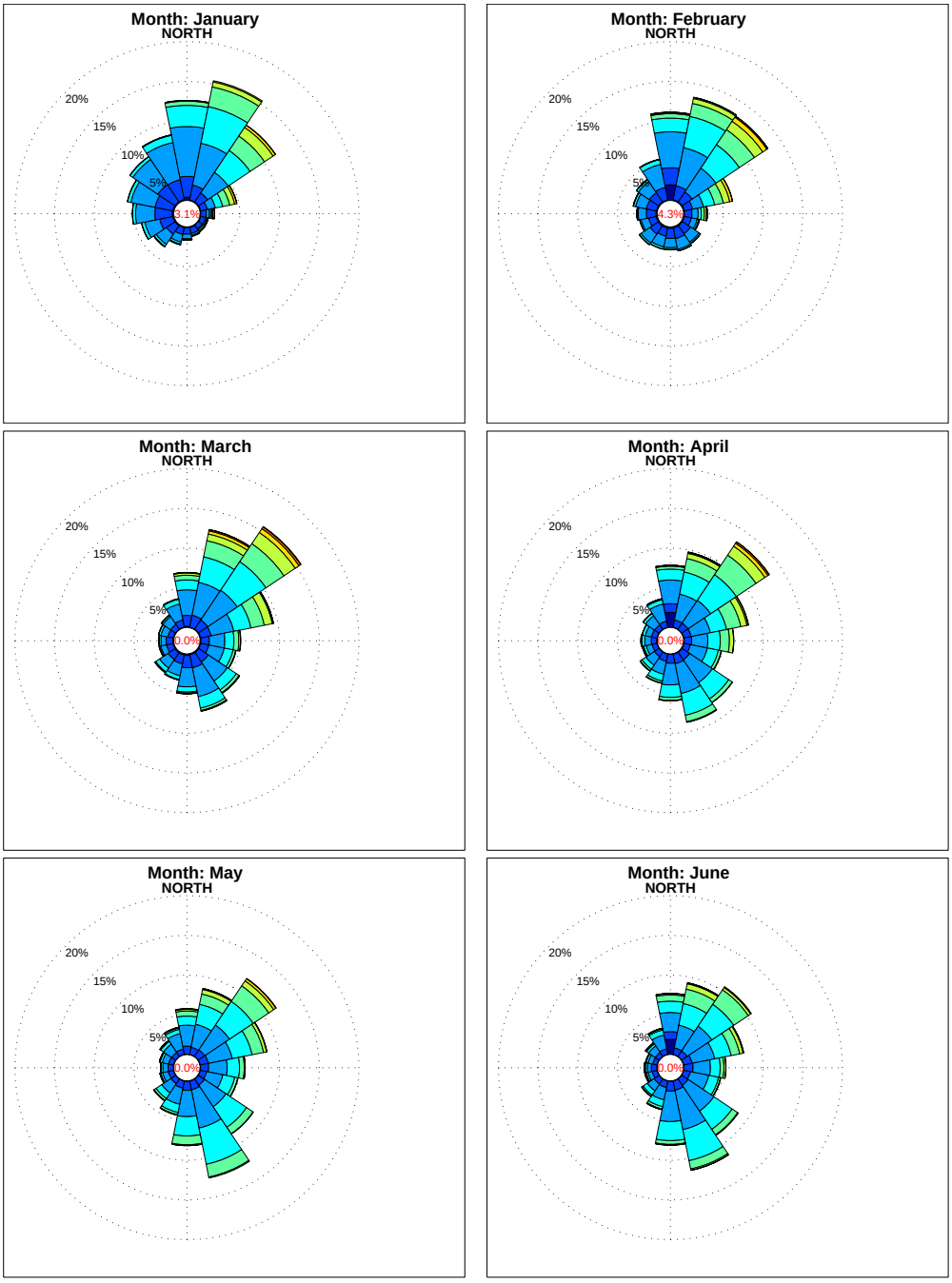

Figure 2.23: Wind rose for monthly evolution of mean wind speed. Station: SAL

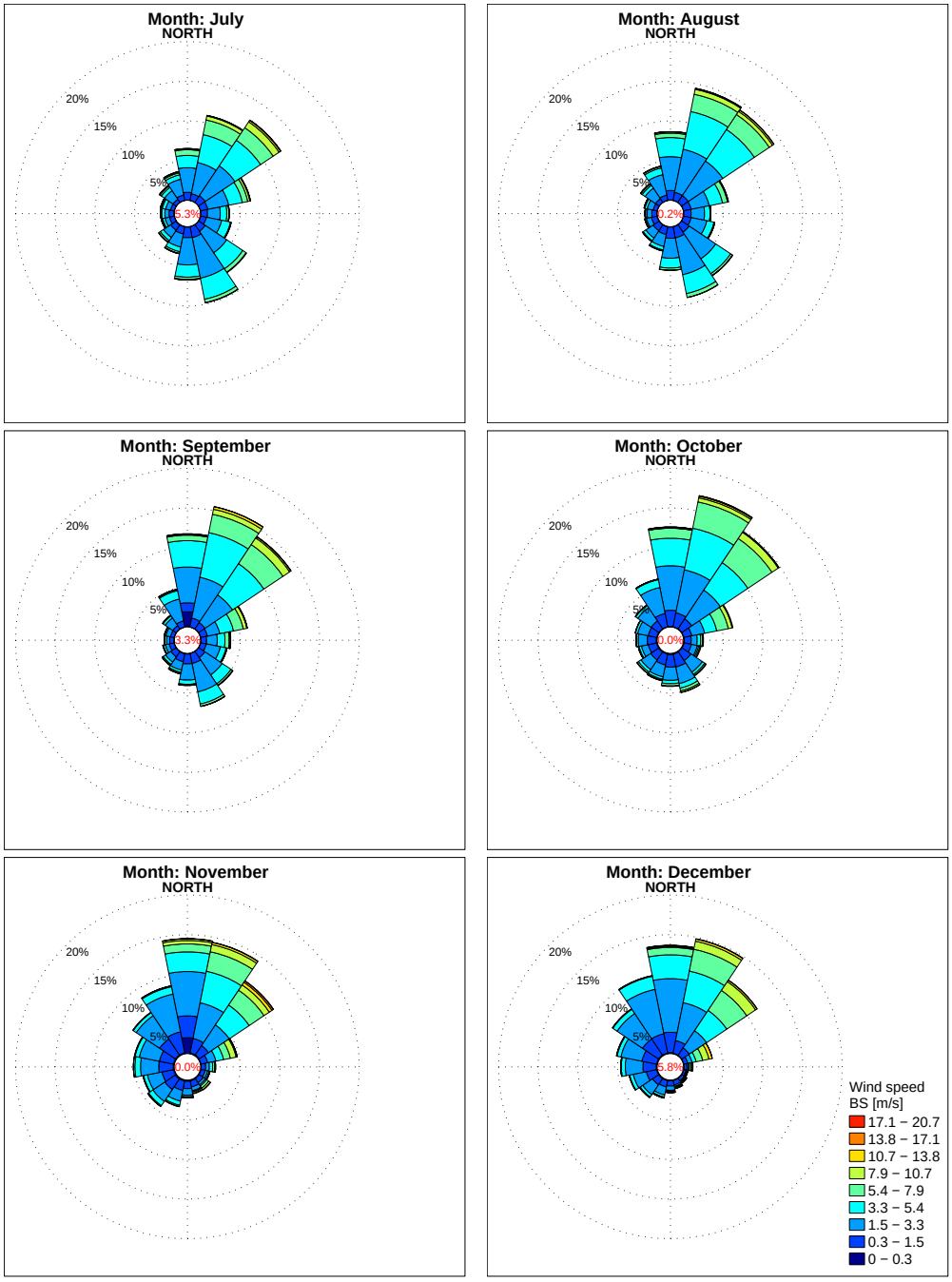

Figure 2.24: Wind rose for monthly evolution of mean wind speed. Station: SAL

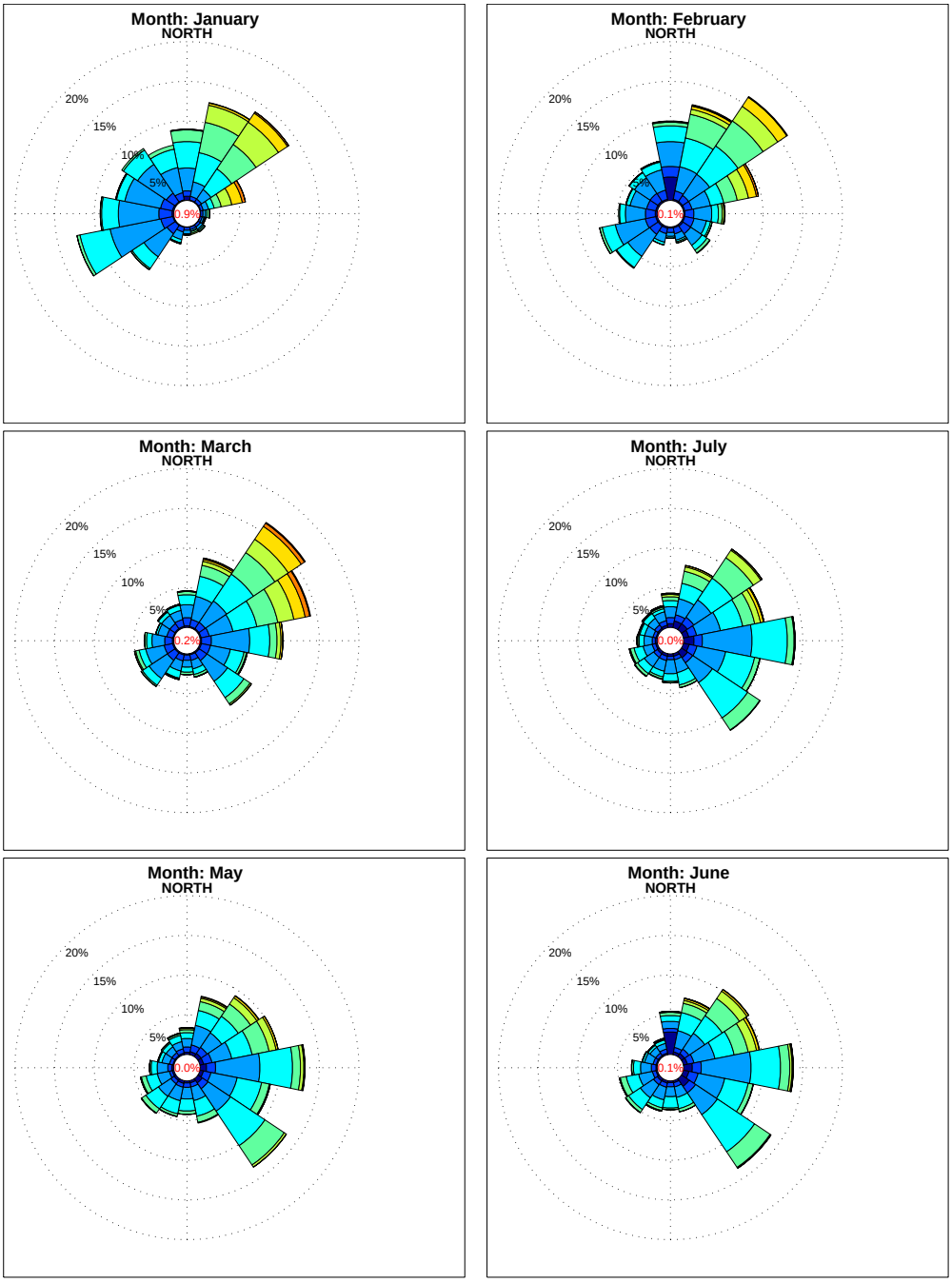

Figure 2.25: Wind rose for monthly evolution of mean wind speed. Station: CHI

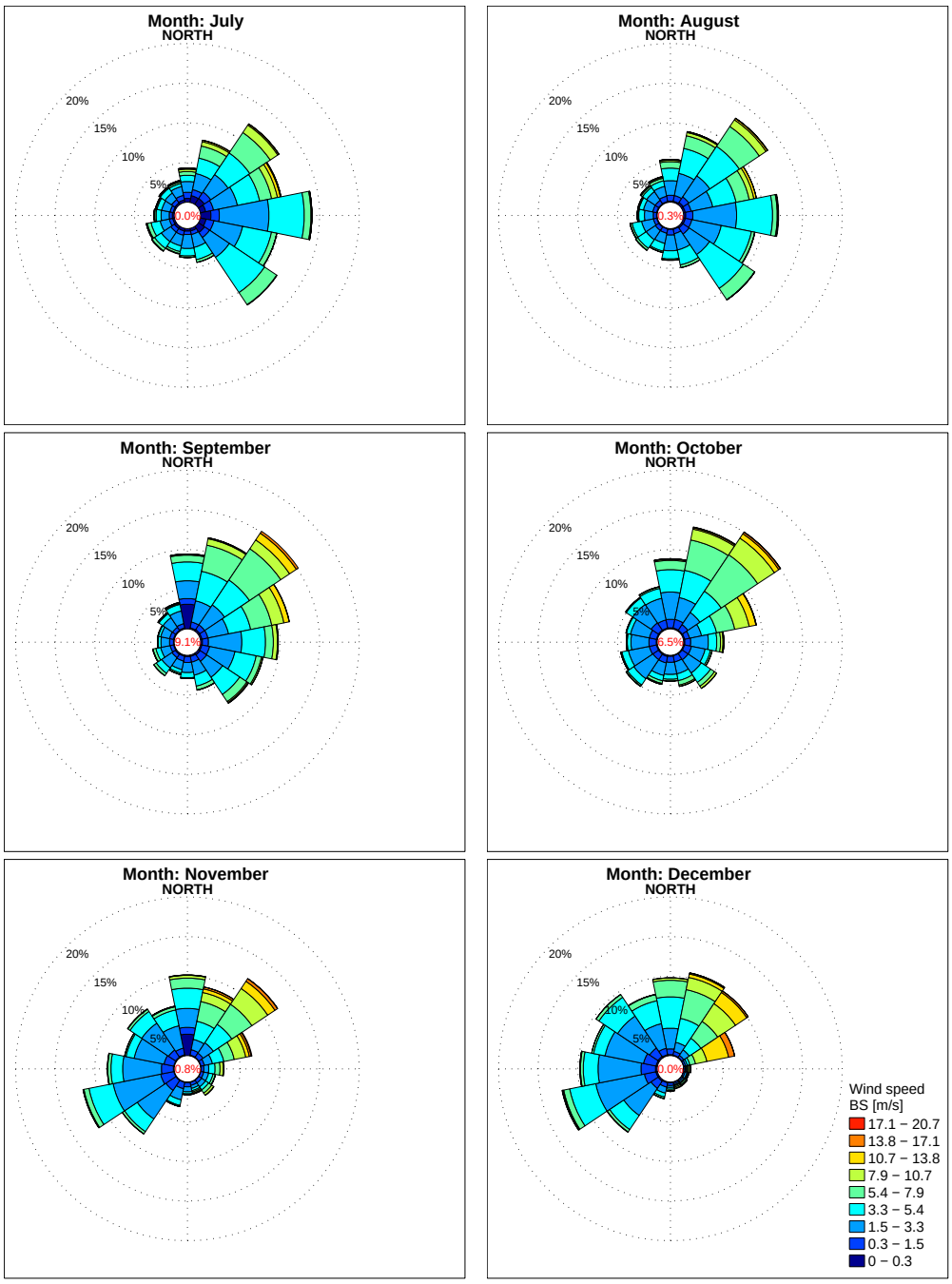

Figure 2.26: Wind rose for monthly evolution of mean wind speed. Station: CHI

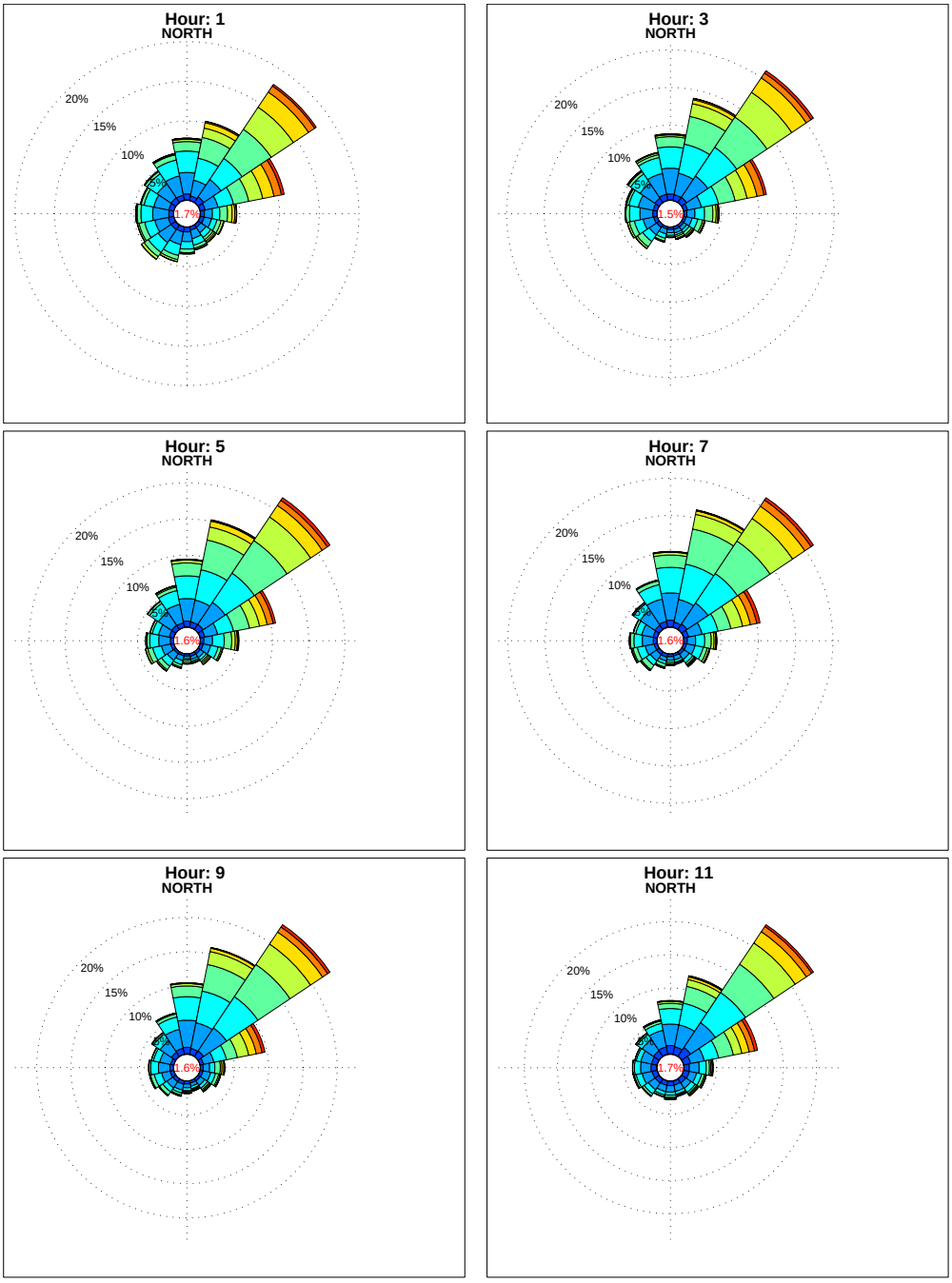

Figure 2.27: Wind rose for hourly evolution of mean wind speed. Station: PAA

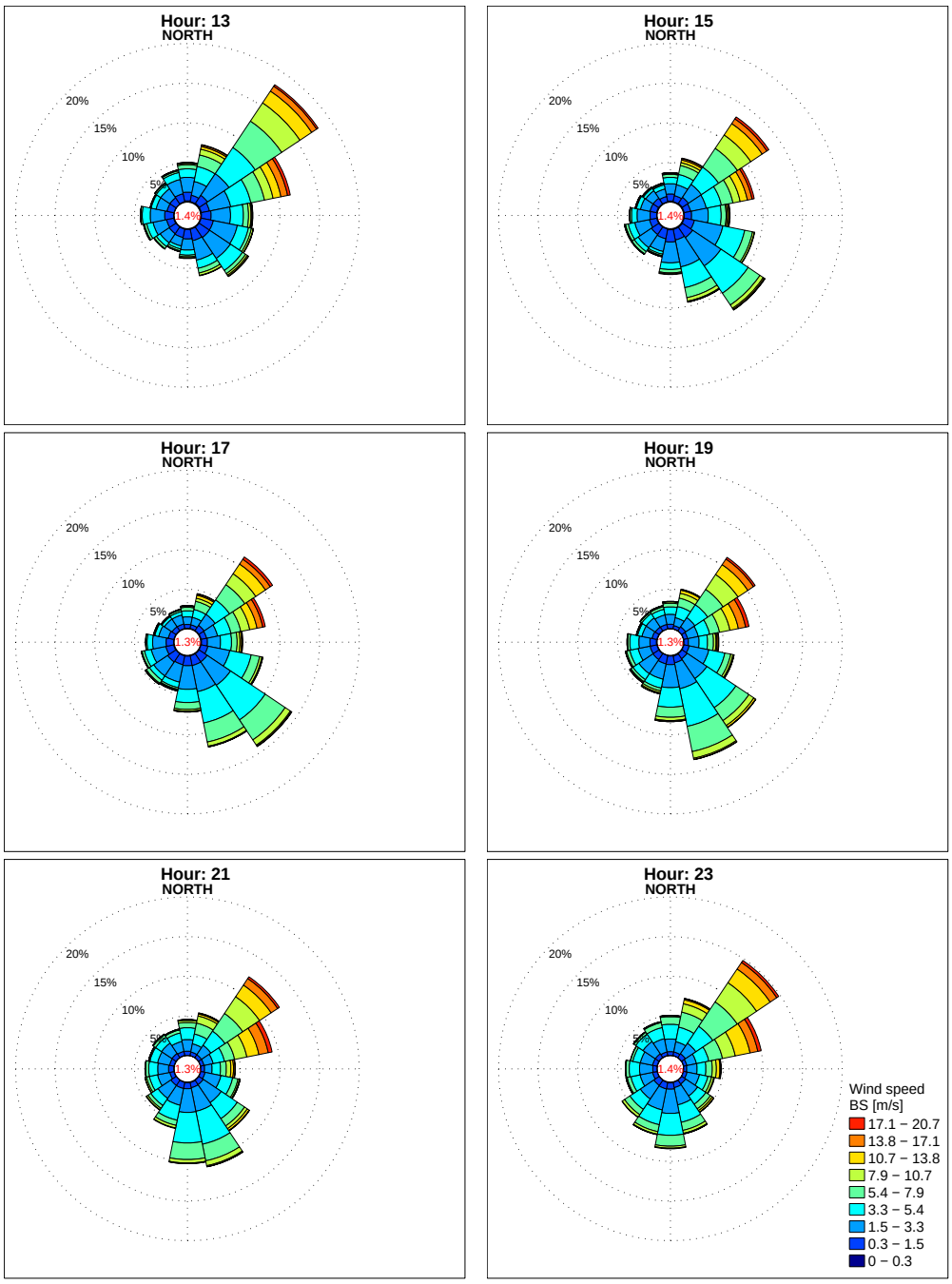

Figure 2.28: Wind rose for hourly evolution of mean wind speed. Station: PAA

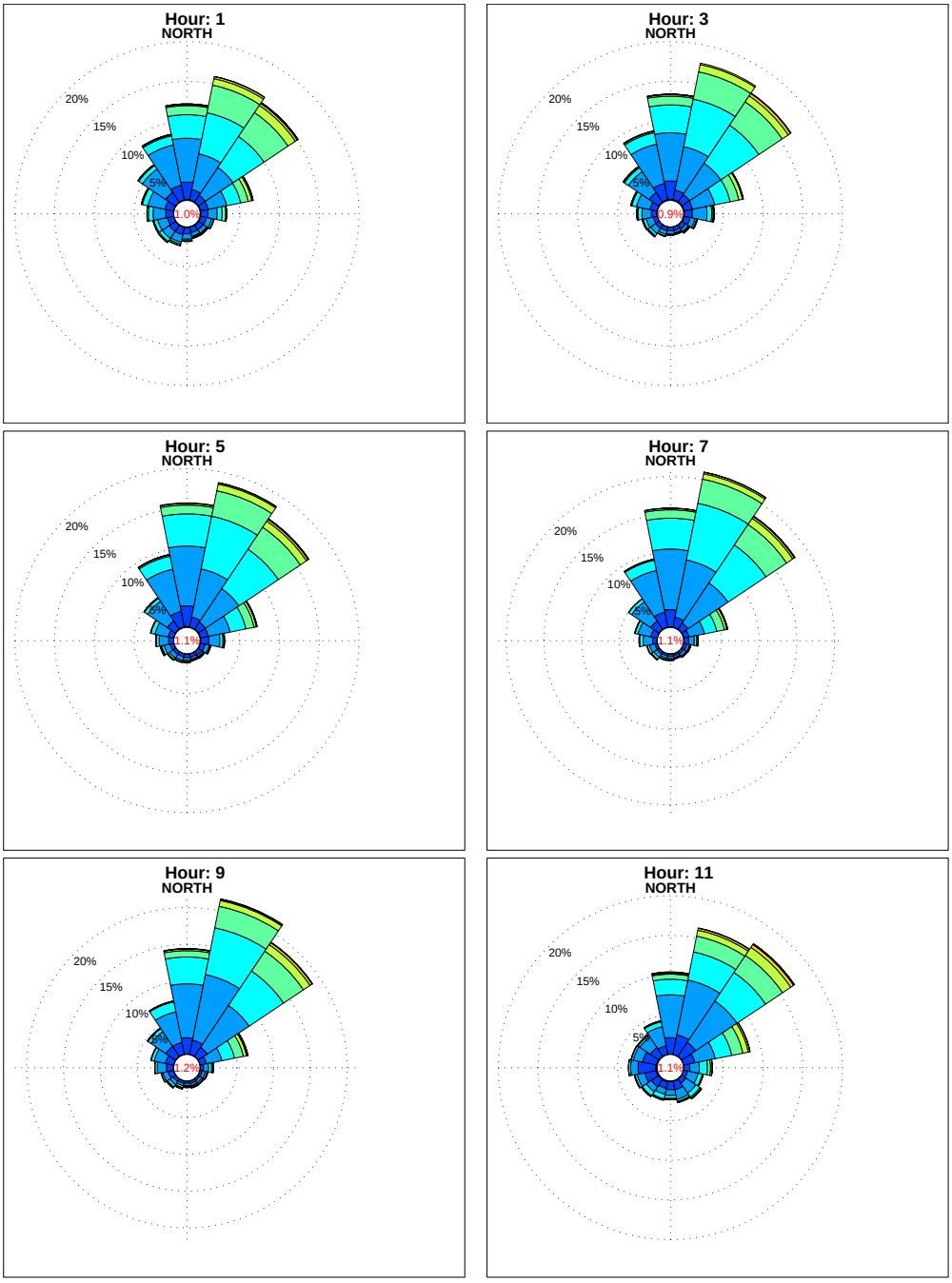

Figure 2.29: Wind rose for hourly evolution of mean wind speed. Station: SAL

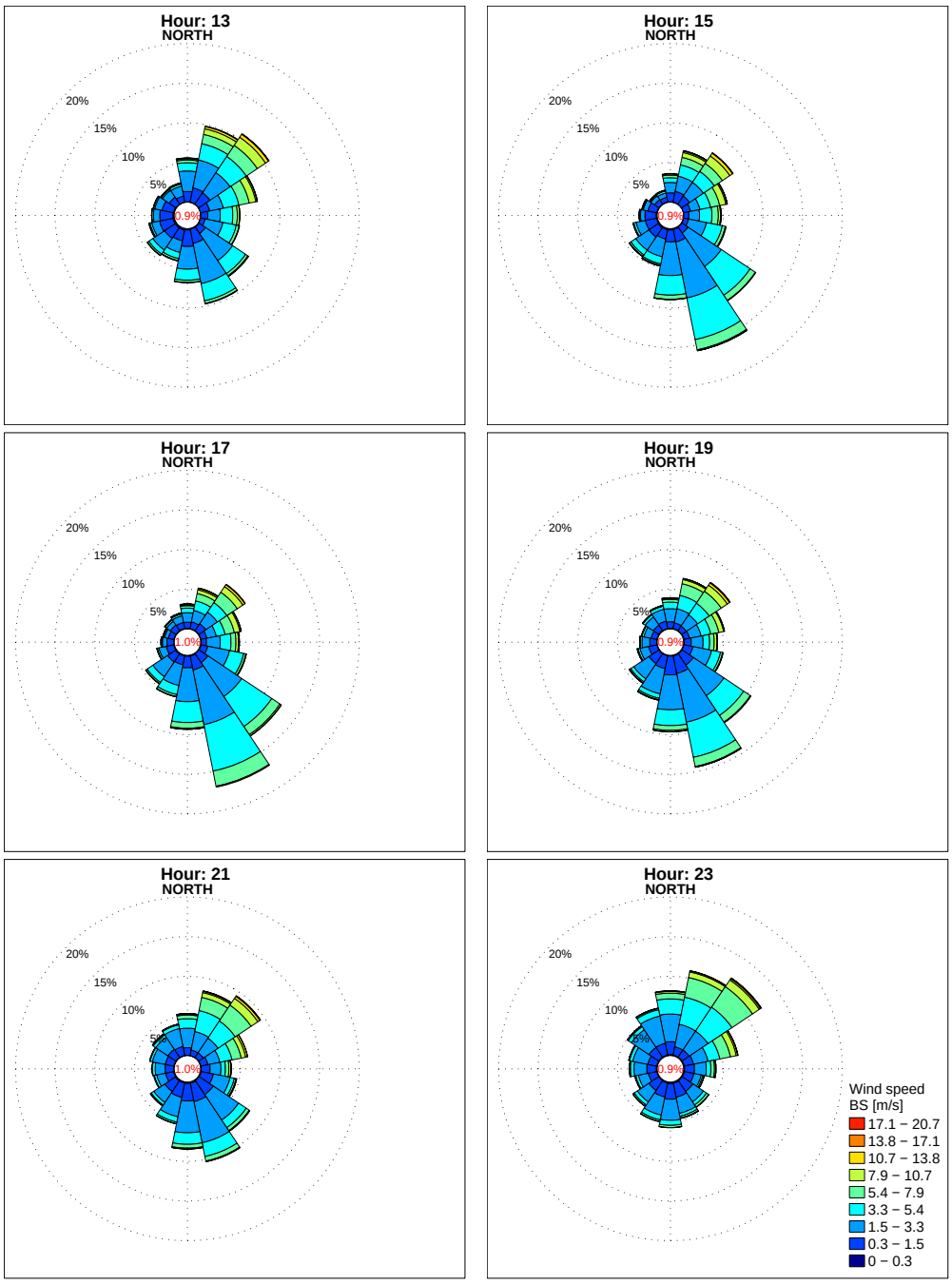

Figure 2.30: Wind rose for hourly evolution of mean wind speed. Station: SAL

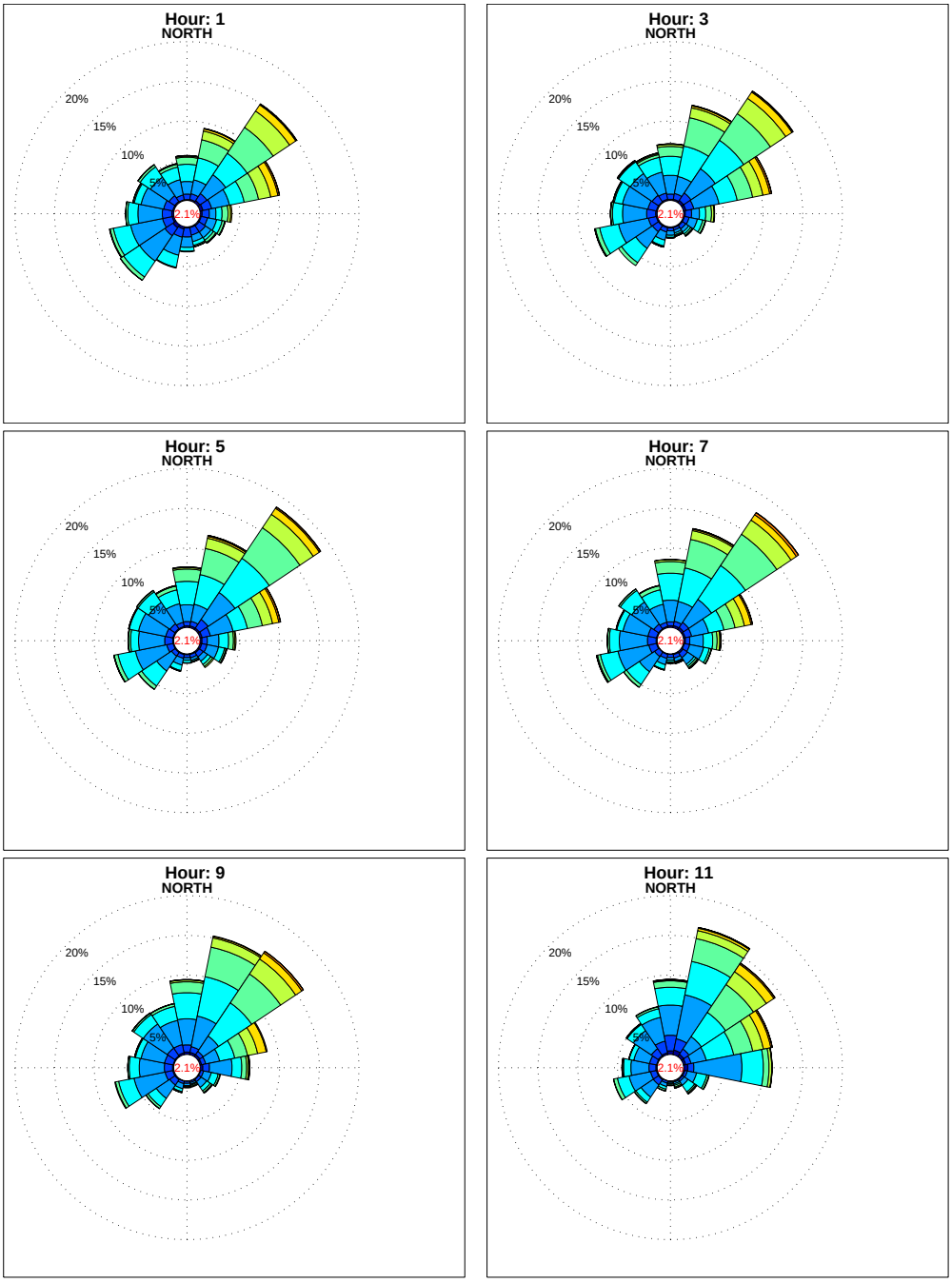

Figure 2.31: Wind rose for hourly evolution of mean wind speed. Station: CHI

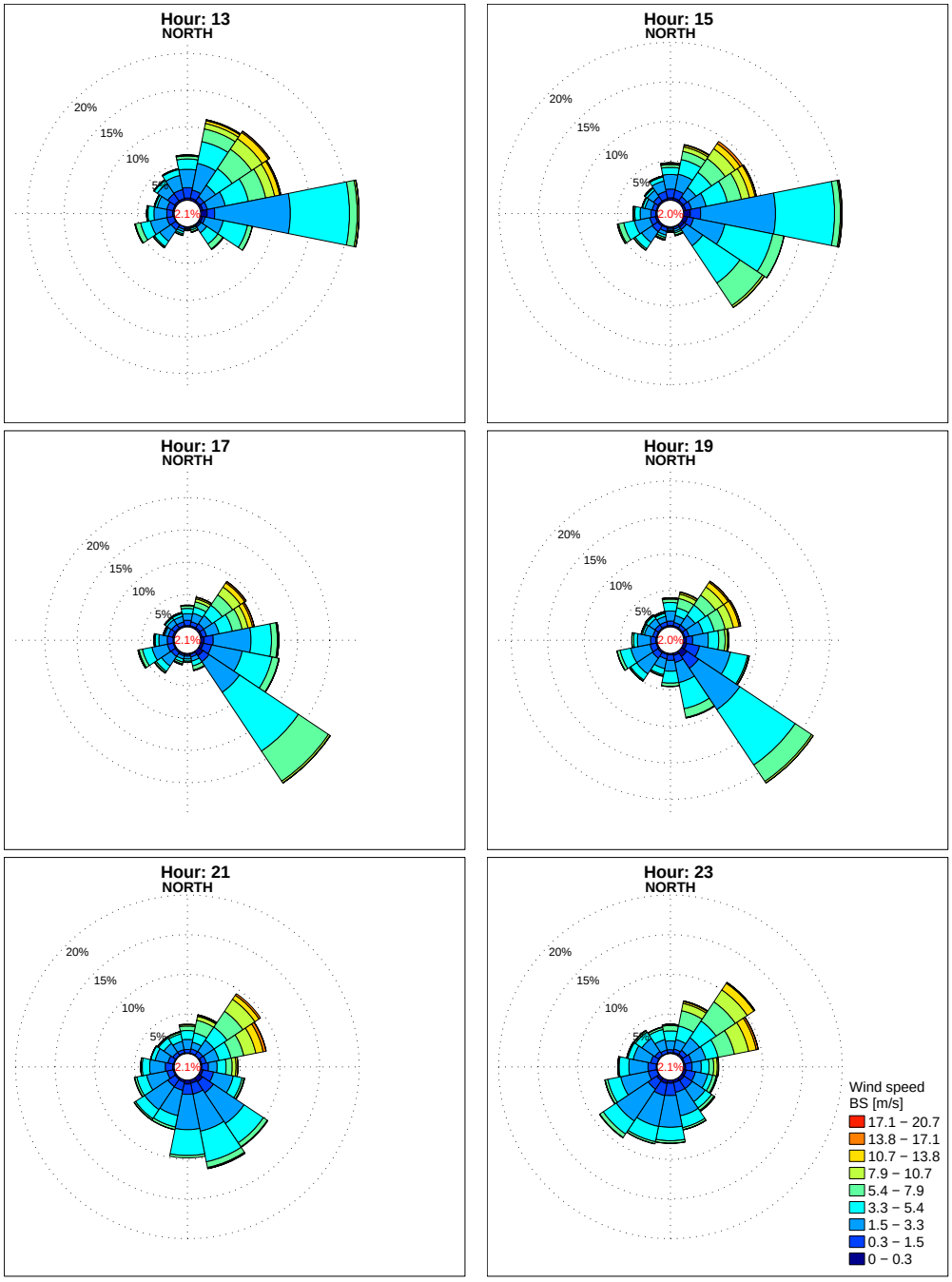

Figure 2.32: Wind rose for hourly evolution of mean wind speed. Station: CHI

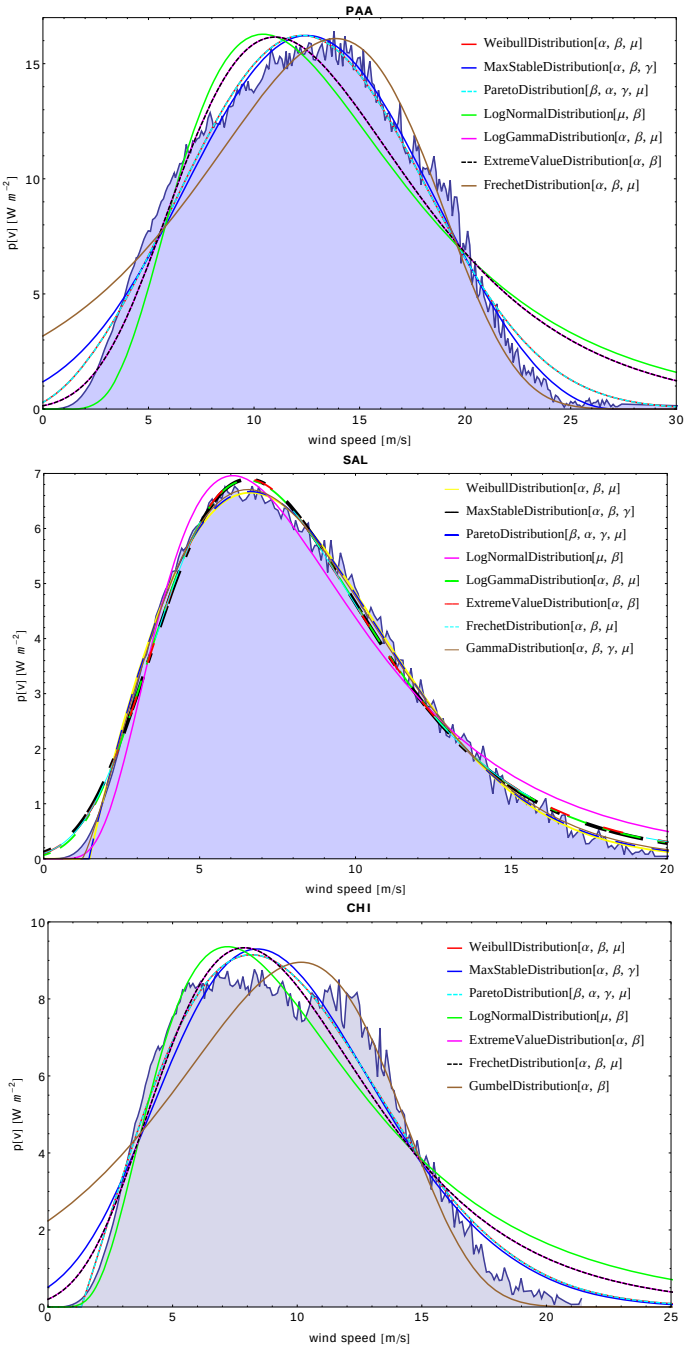

Figure 2.33: Global wind power density distribution: histograms of the entire dataset for the three stations with the calculated PDF.

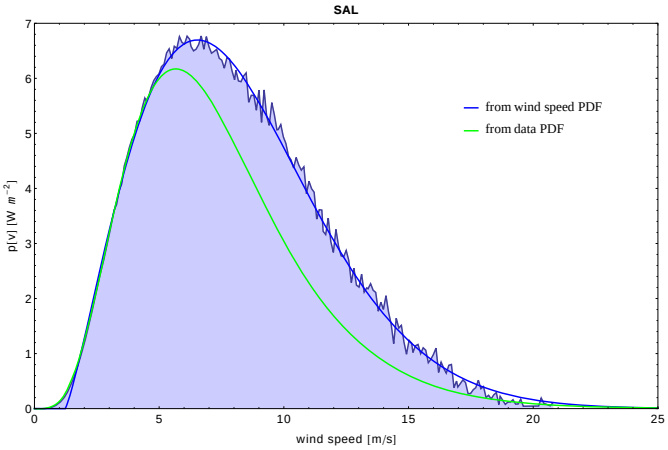

Figure 2.34: Global wind power density distribution: histograms of the entire dataset; the PDF calculated applying the power density distribution equation to the dataset; the PDF calculated applying the equation to the PDF derived for wind speed.

Part III

Drainage channel formation

Chapter 3

Rill spacing in hillslopes

Abstract

A simple two-dimensional model of flow field and bed topography along an hill-slope is proposed to investigate the key mechanisms leading to stability/instability of the system and the formation of periodic parallel drainage channels (rills). A linear stability analysis is carried out to perturb flow field and bed topography, leading to an eigenvalue problem. Channel inter-axis is derived by marginal stability analysis as function of the fundamental parameters of the system. The results are dependent on four parameters: the depth of the water sheet; the length of the hill-slope; the critical velocity for erosion; the concentration at the bed. A sensitivity analysis on this parameter space has been made for a wide range of values.

The role of bed load transport is found to be crucial for stabilizing the system and leading to a draining channel generation.

Despite the substantial simplicity, the model appears to mimic the essential physics of the system, giving reasonable values for the fill inter-axis for the investigated parameter space.

Figure 3.1: Regular spacing of parallel rills in Dinosaur Provincial Park, Alberta - Canada (by @Fotomorgana).

3.1 Formulation of the problem

In many environments it is possible to see drainage channels that appear to be parallel and uniformly spaced (see fig. 3.1). The characteristic wavelength of channel inter-axes seems to be an emergent property of the hydrodynamic and sediment transport processes that act on these environments (Perron et al., 2008 [44]).

Studying the formation of erosional rills, Smith and Bretherton (1972)[45] showed that an erodible surface under a sheet flow is unstable with respect to lateral perturbations, leading to incipient channel formation; in particular, they demonstrated that the shortest-wavelength grow faster, resulting in instability and no preferred wavelength. To overcome this instability, Loewenherz (1991)[46] introduced an artificial smoothing function and she obtained that the intermediate wavelengths grow faster, leading to a stable channel formation.

Later on, several researchers have investigated drainage channel formation by free-surface flows, both analytically ([47], [48], [49]) and numerically ([50], [51]). There exists a lot of different models, often specialized to describe a particular conditions of channel formation. This leads to great difficulties in satisfactory interpretations of the underlying mechanisms, and in this way, the results are hardly comparable. Izumi and Parker (2000, [48]), for example, based the model on the Froude number and a moving reference, obtaining a downstream-driven theory. On the other hand, Perron et al. (2008, [44]) concentrate on a landscape Peclet number, which quantifies the relative importance of advective and diffusive sediment transport processes.

Apart the differences, the existing models indicate that it is possible to use the equations for shallow water flow, together with appropriate formulations of sediment transport, to provide a theory of channel formation.

The strategy of the present research is to suitably simplify the relevant equations, to construct an analytical model of periodically spacing channel formation. The focus is limited to channelization due to surface sheet flow.

In section 3.2 it is introduced the geometry of the analysed system and the general assumption and notations. The model is described in section 3.3, while the boundary conditions are reported in section 3.4. The scaling of the equations is described in section 3.5, and the perturbation analysis is developed in section 3.6. The analytical solution is reported in section 3.7; the results are shown in section 3.8. Finally section 3.9 reports the conclusions.

3.2 Domain and general assumptions

The domain is an hill-slope with given width B_0^* and length L_0^*. The longitudinal x-axis is posed at the centre of the domain and is pointing downstream. H^* represents the local free surface elevation; D^* is the water depth and η^* is the bed elevation. They all are measured respect to a common reference plane (the reference is such that at $x^* = 0$, $\eta^* = 0$). Here and in

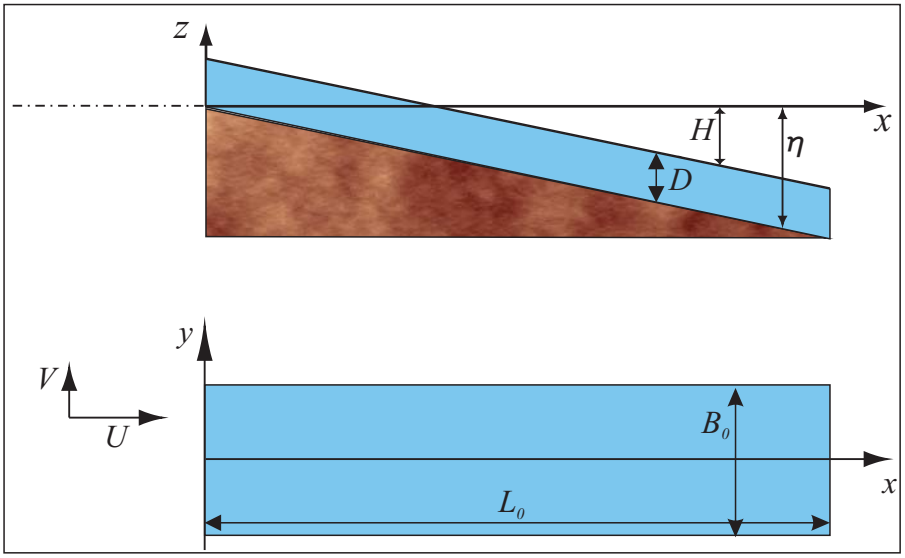

Figure 3.2: A stretch of the investigated domain with the relevant notations

the following, a superscript asterisk denotes dimensional quantities. A sketch of the investigated domain is showed in figure 3.2.

Being the morphological time scale (associated with bed surface evolution in response to erosion) much larger than the flow time scale (associated with the response of the flow to the bed changing), it is reasonable to adopt the quasi-steady state approach for the flow field, Accordingly, the unsteady terms in the equations are neglected. Moreover, it is assumed the absence of density- and wind-driven currents.

The unperturbed flow is uniform with constant (depth averaged) velocity $U^*[x, y, t] = U_0$; in the basic state the bed is flat and tilted, with unperturbed water depth D_0^*.

The slope of the bed surface is mild for the flow to be critical. Sediment is cohesionless with geometric mean size d_s^* and density ρ_s. The bed is erodible and sediment is transported as both suspended load and bed load; the Shields stress exceeds its critical value everywhere. The sediment balance is described by the 2-D Exner's equation.

3.3 Governing equations

According to the present assumptions, a depth-averaged model is used, where the governing flow field equations are the shallow water equations associated with two-dimensional sheet flow:

$$\frac{\partial D^*}{\partial t^*} + \frac{\partial U^* D^*}{\partial x^*} + \frac{\partial V^* D^*}{\partial y^*} = 0 \tag{3.1}$$

$$\frac{\partial U^*}{\partial t^*} + U^* \frac{\partial U^*}{\partial x^*} + V^* \frac{\partial U^*}{\partial y^*} + g \frac{\partial H^*}{\partial x^*} + \frac{\tau_x^*}{\rho_w D^*} = 0 \tag{3.2}$$

$$\frac{\partial V^*}{\partial t^*} + U^* \frac{\partial V^*}{\partial x^*} + V^* \frac{\partial V^*}{\partial y^*} + g \frac{\partial H^*}{\partial y^*} + \frac{\tau_y^*}{\rho_w D^*} = 0 \tag{3.3}$$

where t^* is time; x^* and y^* are the longitudinal (streamwise) and lateral Cartesian coordinates; H^* and D^* denote instantaneous free surface elevation and water depth, respectively; U^* and V^* are longitudinal and lateral components of the depth-averaged fluid velocity; g is gravitational acceleration; ρ_w is (mean) water density; τ_x^* and τ_y^* are components of bed shear stress in the x^* and y^* directions

$$\vec{\tau}^* = \rho_w C_f \sqrt{U^{*2} + V^{*2}} \vec{U}^* = \rho_w C_f \left\| \vec{U}^* \right\| \vec{U}^* \tag{3.4}$$

where C_f is the friction coefficient

$$C_f = \frac{g}{X^2},\ X = k_s D^{*\frac{1}{6}} \tag{3.5}$$

and k_s is the Gauckler-Strickler roughness coefficient.

The Exner balance equation governing the evolution of the bed elevation $\eta^* = H^* - D^*$, reads

$$(1-p)\frac{\partial \eta^*}{\partial t^*} = (Q_E^* - Q_D^*) - \nabla \cdot q_s^* \tag{3.6}$$

where Q_E^* and Q_D^* are the rate of erosion and deposition, q_s^* is the bed load fluxes per unit width; p is sediment porosity. The erosion and deposition

rates can be estimated using the Partheniades and Krone formulations

$$Q_e^* = Q_{e0}\left(\frac{\tilde{\tau}^*}{\tau_e^*} - 1\right)\bar{H}\left[\frac{\tilde{\tau}^*}{\tau_e^*} - 1\right] \tag{3.7}$$

$$Q_d^* = C_b w_s^*\left(1 - \frac{\tilde{\tau}^*}{\tau_d^*}\right)\bar{H}\left[1 - \frac{\tilde{\tau}^*}{\tau_d^*}\right] \tag{3.8}$$

$$\tilde{\tau}^* = |\tau^*| = \rho_w C_f\left(U^{*2} + V^{*2}\right) \tag{3.9}$$

where Q_{e0} is a characteristic erosion rate; τ_e^* and τ_d^* are threshold of bed shear stress for sediment erosion and deposition; w_s^* is sediment settling velocity; $C_b \sim 2C$ is the volumetric sediment concentration at the bed and $\bar{H}$ is the Heaviside function. Here the sediment concentration is considered dimensionless; to convert the values to the dimensional form it is necessary to multiply the dimensionless concentration for the sediment density.

As a first approximation, it is assumed that the net suspended flux $Q_e^* - Q_d^*$ varies continuously by tacking $\tau_e^* \sim \tau_d^*$ and $Q_{e0} \sim C_b w_s$, with $\tau_e^* = \rho_w C_f U_c^2$, and U_c is the threshold velocity for sediment movement. The net suspended flux is eventually written as

$$Q_e^* - Q_d^* \sim 4Cw_s\left(\frac{\tilde{\tau}^*}{\tau_e^*} - 1\right) = 4Cw_s\left(\frac{U^{*2} + V^{*2}}{U_c^2} - 1\right) \tag{3.10}$$

The bedload flux q_s can be model as in Lanzoni and Tubino (1999, [52])

$$q_s = \Phi\sqrt{\left(\frac{\rho_s}{\rho_w} - 1\right) g d_s^{*3}}\left(\cos\phi^*, \sin\phi^*\right) = \Phi Q_{s0}\left(\cos\phi^*, \sin\phi^*\right) \tag{3.11}$$

$$\Phi = 8\left(\vartheta^* - \vartheta_c\right)^{3/2}\bar{H}\left[\vartheta^* - \vartheta_c\right] \tag{3.12}$$

where ϕ^* denotes the angle between bedload transport direction and x-axis; Φ is the intensity of bedload transport in the classical Meyer-Peter and Muller form; ϑ^* is dimensionless bed shear stress (Shields parameter) and ϑ_c is its

critical value for incipient sediment motion

$$\vartheta^* = \frac{|\tau^*|}{(\rho_s - \rho_w)\, g d_s^*}. \tag{3.13}$$

Furthermore, it is:

$$\cos\phi^* = \cos\varphi \sim -\frac{3}{2}\frac{\vartheta_c}{\vartheta^* - \vartheta_c}\frac{\partial \eta^*}{\partial x^*} \tag{3.14}$$

$$\sin\phi^* = \sin\varphi - \frac{r}{\sqrt{\vartheta^*}}\frac{\partial \eta^*}{\partial y^*} \sim -\frac{r}{\sqrt{\vartheta^*}}\frac{\partial \eta^*}{\partial y^*} \tag{3.15}$$

where φ is the (small) angle between the bottom stress vector and the x-axis; r is a dimensionless parameter given by [53]

$$r = \frac{1}{9}\left(\frac{d_s^*}{D_0^*}\right)^{-0.3} \tag{3.16}$$

Accordingly, the Exner sediment balance equation governing the evolution of bed elevation becomes

$$\begin{aligned}(1-p)\frac{\partial \eta^*}{\partial t^*} = {} & E\left(\frac{U^{*2} + V^{*2}}{U_c^2} - 1\right) + \\ & - \nabla \cdot \left(8\left(\vartheta^* - \vartheta_c\right)^{3/2} \bar{H}\left[\vartheta^* - \vartheta_c\right] \sqrt{\left(\frac{\rho_s}{\rho_w} - 1\right) g d_s^{*3}} \cdot \right. \\ & \left. \cdot \left\{ -\frac{3}{2}\frac{\vartheta_c}{\vartheta^* - \vartheta_c}\frac{\partial \eta^*}{\partial x^*}, -\frac{r}{\sqrt{\vartheta^*}}\frac{\partial \eta^*}{\partial y^*} \right\} \right)\end{aligned} \tag{3.17}$$

where E is a suitably define erosion coefficient.

3.4 Boundary conditions

It is assumed that a uniform sheet of water flows over the hill slope. At the lateral water divide an impermeable condition is prescribed

$$V^* = 0 \quad \text{at } y^* = \pm\frac{B_0^*}{2} \tag{3.18}$$

$$Q^* = Q_0^* = U_0 D_0^* B_0^* \quad \text{at } x^* = 0 \tag{3.19}$$

while upstream discharge is assumed at the top of the hillslope. In other words, the hillslope is assumed to drain a constant amount of water.

3.5 Scaling

To derive an analytical solution of the problem, it is convenient to write the equations in dimensionless form using the following scaling

$$t = \frac{U_0}{L_0^*} t^*, \quad \{x, y\} = \frac{1}{L_0^*} \{x^*, y^*\}, \quad \{H, D, \eta, d_s\} = \frac{1}{D_0^*} \{H^*, D^*, \eta^*, d_s^*\} \tag{3.20}$$

$$\{U, V\} = \frac{1}{U_0} \{U^*, V^*\}, \quad \{\tau_x, \tau_y\} = \frac{1}{\rho_w C_f U_0^2} \{\tau_x^*, \tau_y^*\} \tag{3.21}$$

where D_0^* and U_0 are the depth and velocity in the basic state.

Note that only external scales, i.e. not resulting from morphological processes, are considered. The dimensionless continuity and momentum equations become

$$\frac{\partial D}{\partial t} + \frac{\partial U D}{\partial x} + \frac{\partial V D}{\partial y} = 0 \tag{3.22}$$

$$\chi_m \left(\frac{\partial U}{\partial t} + U \frac{\partial U}{\partial x} + V \frac{\partial U}{\partial y} \right) + \frac{\partial H}{\partial x} + \chi_\tau \frac{\tau_x}{D} = 0 \tag{3.23}$$

$$\chi_m \left(\frac{\partial V}{\partial t} + U \frac{\partial V}{\partial x} + V \frac{\partial V}{\partial y} \right) + \frac{\partial H}{\partial y} + \chi_\tau \frac{\tau_y}{D} = 0 \tag{3.24}$$

where

$$\chi_m = \frac{U_0^2}{g D_0^*}, \quad \chi_\tau = C_f \frac{U_0^2}{g D_0^*} \frac{L_0^*}{D_0^*} \tag{3.25}$$

The parameters χ_m and χ_τ, weighting inertia and friction with respect to gravitational effects in the momentum equation, are typically small.
The term $\frac{L_0^*}{D_0^*}$ represents the aspect ratio of the system. The dimensionless

bed shear stress components reads:

$$\{\tau_x, \tau_y\} = \sqrt{U^2 + V^2}\{U, V\} \tag{3.26}$$

The sediment balance equation becomes

$$\frac{1}{\sigma}\frac{\partial \eta}{\partial t} = (\vartheta - \alpha^2) - \mathcal{B}\nabla \cdot \left((\vartheta - \tilde{\vartheta}_c)^{\frac{3}{2}} \left\{ \frac{\mathcal{B}_\infty}{\mathcal{B}} \frac{1}{(\vartheta - \tilde{\vartheta}_c)} \frac{\partial \eta}{\partial y}, -\frac{r\mathcal{B}_\in}{\mathcal{B}\sqrt{\vartheta}} \frac{\partial \eta}{\partial y} \right\} \right) \tag{3.27}$$

$$\frac{1}{\sigma}\frac{\partial \eta}{\partial t} = (\vartheta - \alpha^2) - \mathcal{B}_\infty \frac{\partial}{\partial x}\left(\left(\vartheta - \tilde{\vartheta}_c\right)^{\frac{1}{2}} \frac{\partial \eta}{\partial x} \right) - \mathcal{B}_\in \frac{\partial}{\partial y}\left(\left(\vartheta - \tilde{\vartheta}_c\right)^{\frac{3}{2}} \frac{1}{\sqrt{\vartheta}} \frac{\partial \eta}{\partial y} \right) \tag{3.28}$$

where the dimensionless morphological time scale σ and the dimensionless bed-load parameters are defined as

$$\sigma = \frac{4}{1-p}\frac{L_0^*}{D_0^*}\frac{Cw_s}{U_0}\alpha^2 \tag{3.29}$$

$$\mathcal{B} = \alpha^2 \frac{2}{Cw_s}\frac{D_0^*}{L_0^2}\frac{(C_f U_0^2)^{3/2}}{\Delta g} \tag{3.30}$$

$$\mathcal{B}_\infty = \frac{3}{2}\mathcal{B}\tilde{\vartheta}_c \tag{3.31}$$

$$\mathcal{B}_\in = r\mathcal{B}\sqrt{\frac{\Delta g d_s}{C_f U_0^2}} \tag{3.32}$$

and the other parameters are

$$\alpha = \frac{U_c}{U_0}, \qquad \vartheta = U^2 + V^2 \tag{3.33}$$

$$\tilde{\vartheta}_c = \frac{\Delta g d_s \vartheta_c}{C_f U_0^2}, \qquad \Delta = \left(\frac{\rho_s}{\rho_w} - 1\right) \tag{3.34}$$

Introducing the following dimensionless relevant parameters

$$\beta = \frac{L_0^*}{D_0^*}, \quad Fr = \frac{U_0}{\sqrt{gD_0^*}} \quad \text{and} \quad Fr_* = \frac{U_0}{Cw_s} \tag{3.35}$$

the dimensionless parameters of the equations read

$$\chi_m = Fr^2, \qquad \chi_\tau = C_f \beta Fr^2 \tag{3.36}$$

$$\sigma = \frac{4}{(1-p)}\alpha^{-2}\beta Fr_*^{-1}, \qquad \mathcal{B} = \frac{2C_f^{3/2}}{\Delta}\alpha^2\beta^{-2}Fr^2 Fr_* \tag{3.37}$$

Finally, the boundary conditions becomes:

$$V = 0 \quad \text{at } y = \pm\frac{1}{2} \tag{3.38}$$

$$Q = Q_0 = 1 \quad \text{at } x = 0. \tag{3.39}$$

3.6 Perturbation analysis

In order to study the stability of transverse perturbations, the following perturbation of the basic state equilibrium is considered, in terms of the small parameter ε

$$\Psi = \Psi_{eq} + \varepsilon\tilde{\Psi} + O\left(\varepsilon^2\right) \tag{3.40}$$

where $\Psi = \{H, U, V, \eta\}$ is the solution, $\Psi_{eq} = \{H_0, U_0, V_0, \eta_0\}$ represents the basic state and $\tilde{\Psi} = \{H_1, U_1, V_1, \eta_1\}$ is the perturbation. The dimensionless equations are linearised by substituting the decomposition 3.40. Solutions are then taken to be of the normal mode form with

$$\tilde{H} = e^{\omega\sigma t}\hat{H}[x]\cos[ky] \tag{3.41}$$

$$\tilde{U} = e^{\omega\sigma t}\hat{U}[x]\cos[ky] \tag{3.42}$$

$$\tilde{V} = e^{\omega\sigma t}\hat{V}[x]\sin[ky] \tag{3.43}$$

$$\tilde{\eta} = e^{\omega\sigma t}\hat{\eta}[x]\cos[ky] \tag{3.44}$$

where k is the perturbation wave number in the transverse direction and ω is a complex number which is composed of a growth rate $Re[\omega]$ and a frequency $Im[\omega]$. $\hat{H}$, $\hat{U}$, $\hat{V}$ and $\hat{\eta}$ represent the longitudinal structure of the

perturbations. The chosen decomposition allows to separate the x, y and t dependencies.

3.7 Solution

3.7.1 Leading order problem

Using the perturbation expansion 3.40, at the leading order of approximation (ε^0) the quasi-steady state equations give

$$\frac{\partial U_0 D_0}{\partial x} + \frac{\partial V_0 D_0}{\partial y} = 0 \tag{3.45}$$

$$\chi_m \left(U_0 \frac{\partial U_0}{\partial x} + V_0 \frac{\partial U_0}{\partial y} \right) + \frac{\partial H_0}{\partial x} + \chi_\tau \frac{\sqrt{U_0^2 + V_0^2} U_0}{D_0} = 0 \tag{3.46}$$

$$\chi_m \left(U_0 \frac{\partial V_0}{\partial x} + V_0 \frac{\partial V_0}{\partial y} \right) + \frac{\partial H_0}{\partial y} + \chi_\tau \frac{\sqrt{U_0^2 + V_0^2} V_0}{D_0} = 0 \tag{3.47}$$

$$\frac{1}{\sigma} \frac{\partial \eta_0}{\partial t} = \left(U_0^2 + V_0^2 - \alpha^2 \right) - F\left[U_0, V_0, \eta_0 \right] \tag{3.48}$$

where F is a long expression function of U_0, V_0, η_0.

In the basic uniform sheet flow the transverse velocity is identically zero, $V_0[x, y, t] = 0$, while $U_0[x, y, t] = U_0$, $D_0[x, y, t] = D_0$. The momentum equations 3.46 and 3.47 then reduce to

$$\frac{\partial H_0}{\partial x} + \chi_\tau \frac{U_0^2}{D_0} = 0 \tag{3.49}$$

$$\frac{\partial H_0}{\partial y} = 0 \tag{3.50}$$

The second implies the independence of H_0 and η_0 from the y-coordinate. On the other hand, the hypothesis that the basic state is also characterized by equilibrium bed also implies that $\frac{\partial \eta_0}{\partial t} = 0$ and $\frac{\partial H_0}{\partial t} = 0$. From eq. 3.49, and considering a reference system such that at x=0 $\eta_0[0] = 0$, it then follows

$$H_0[x] = D_0^* - x \frac{\chi_\tau U_0^2}{D_0^*} \tag{3.51}$$

$$\eta_0[x] = -x\frac{\chi_\tau U_0^2}{D_0^*} \tag{3.52}$$

The sediment balance equation implies that $U_0 = \sqrt{U_c}$.

To derive the present solution it has been used a balance between the gravitational and the shear stress contributions in the momentum equation. The same solution is valid considering also the advection terms.

The founded solution is the classical one of ...

3.7.2 First order problem

Observing that the parameter χ_m, representing the square of the Froude number, is generally small, we assumed that $\chi_m = o(\epsilon^1)$ Taking into account the solution for the basic state, at the first order of approximation $o(\varepsilon)$ the quasi-steady state perturbed equations then become

$$U_0\frac{\partial D_1}{\partial x} + D_0\frac{\partial U_1}{\partial x} + D_0\frac{\partial V_1}{\partial y} = 0 \tag{3.53}$$

$$U_0 D_0^2\frac{\partial H_1}{\partial x} + \chi_\tau\left(2U_0^2 D_0 U_1 - U_0^2 D_1\right) = 0 \tag{3.54}$$

$$D_0\frac{\partial H_1}{\partial y} + \chi_\tau U_0 V_1 = 0 \tag{3.55}$$

$$\frac{1}{\sigma}\frac{\partial \eta_1}{\partial t} - 2U_0U_1 + \mathcal{B}_\infty\left(\sqrt{U_0^2 - \tilde{\vartheta}_c}\frac{\partial^2\eta}{\partial x^2} - \chi_\tau\frac{U_0^3}{D_0\sqrt{U_0^2+\tilde{\vartheta}_c}}\frac{\partial U_1}{\partial x}\right) + + \mathcal{B}_\in\left(\frac{(U_0^2-\tilde{\vartheta}_c)^{3/2}}{U_0}\frac{\partial^2\eta}{\partial y^2}\right) = 0 \tag{3.56}$$

Using the following expansion

$$H_1[x,y,t] = h_1[x]\exp[\omega\sigma t]\cos[ky] \tag{3.57}$$

$$U_1[x,y,t] = u_1[x]\exp[\omega\sigma t]\cos[ky] \tag{3.58}$$

$$V_1[x,y,t] = v_1[x]\exp[\omega\sigma t]\sin[ky] \tag{3.59}$$

$$\eta_1[x,y,t] = z_1[x]\exp[\omega\sigma t]\cos[ky] \tag{3.60}$$

the linearised $o(\varepsilon)$ equations become

$$U_0\frac{\partial h_1}{\partial x} + D_0\frac{\partial u_1}{\partial x} + kD_0v_1 - U_0\frac{\partial z_1}{\partial x} = 0 \tag{3.61}$$

$$U_0D_0\frac{\partial h_1}{\partial x} - \chi_\tau U_0^3 h_1 + 2\chi_\tau U_0^2 D_0 u_1 + \chi_\tau U_0^3 z_1 = 0 \tag{3.62}$$

$$kh_1 - \chi_\tau\frac{U_0}{D_0}v_1 = 0 \tag{3.63}$$

$$2U_0u_1 + \chi_\tau\mathcal{B}_\infty\frac{U_0^3}{D_0\sqrt{U_0^2-\tilde{\vartheta}_c}}\frac{\partial u_1}{\partial x} - \mathcal{B}_\infty\frac{U_0^2-\tilde{\vartheta}_c}{\sqrt{U_0^2-\tilde{\vartheta}_c}}\frac{\partial^2 z_1}{\partial x^2} + \\ + k^2\mathcal{B}_\in\frac{(U_0^2-\tilde{\vartheta}_c)^{3/2}}{U_0}z_1 = \omega z_1 \tag{3.64}$$

The problem posed by this system of partial differential equations is characterized by eigenvalues ω that are function of the wavenumber k. These eigenvalues are calculated numerically by Chebyshev Spectral Methods and the solutions are analysed as function of the fundamental parameters, i.e. β, Fr and Fr_*. A sensitivity analysis is carried out for these parameters. It is thus possible to locate the regions of stability of the physical system and the wavelengths of the fastest growing perturbations leading to rill formation.

3.8 Model results

Figure 3.3 shows a typical distribution of the growth rate of perturbations $Re[\omega]$ as function of the wavenumber k. Clearly, the number of eigenvalues is equal to the number of discretization points used along the longitudinal direction; their values depend on the parameters β, Fr and Fr_*. The first 3 eigenvalues are reported in figure 3.4; the first 2 curves are identical, as they are complex conjugates. It is important to note that each curve pass twice the $\omega = 0$ line (controlling the marginal stability).

The results of the analysis on the dependence of the eigenvalues from the discretization cardinality, associated with the spectral method (Chebyshev) used to solve the system of linearized partial differential equations, are

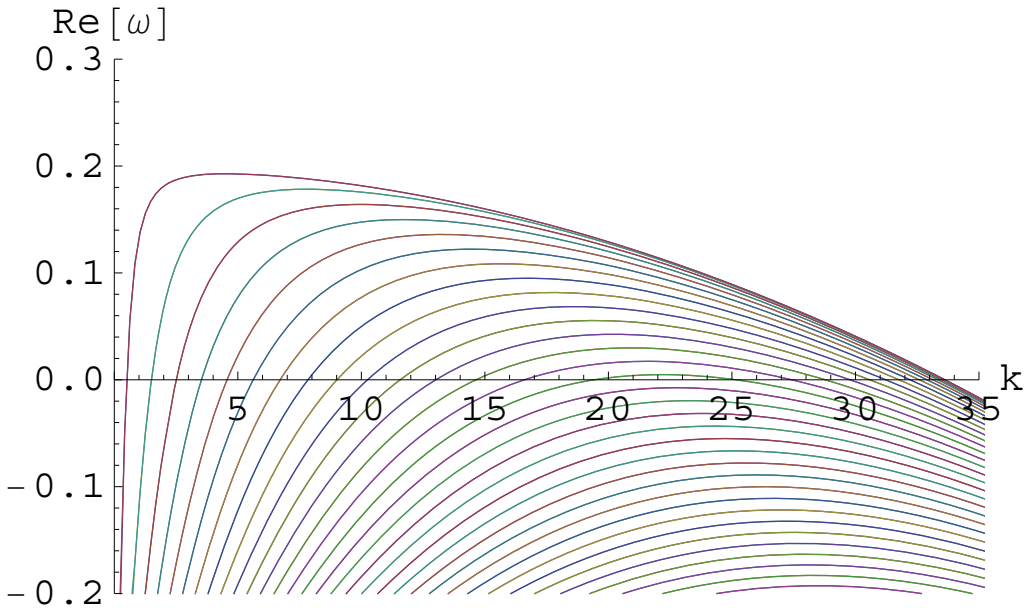

Figure 3.3: Perturbation growth rate as function of the wavenumber k. Parameter values: $\alpha = 0.45$, $\beta = 50$, $Fr = 0.14$, $Fr_* = 89 \times 10^4$.

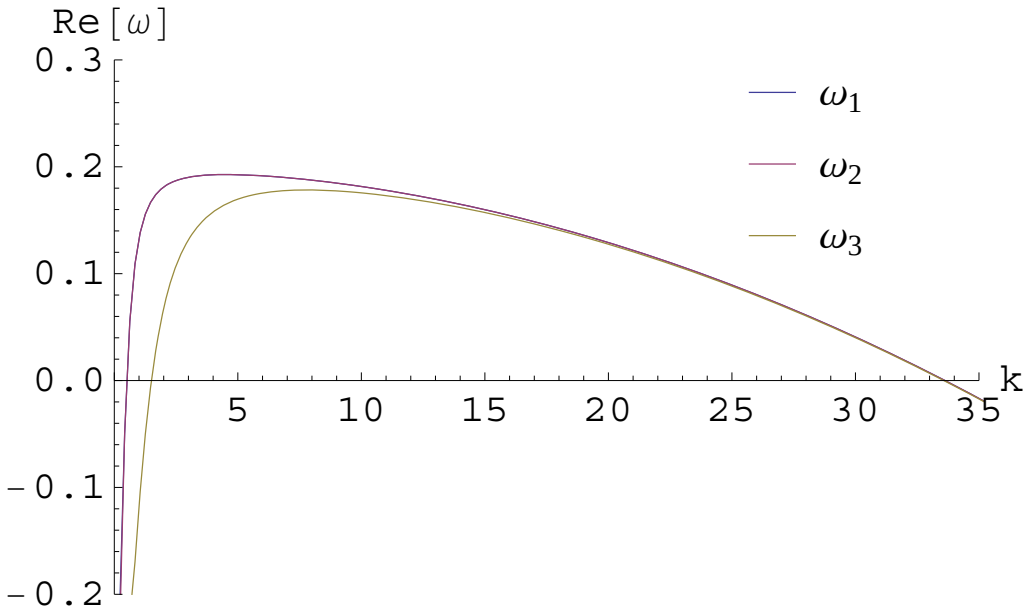

Figure 3.4: Perturbation growth rate resulting from the first 3 modes as function of the wavenumber k. The curve ω_1 and ω_2 are complex conjugate. Parameter values: $\alpha = 0.45$, $\beta = 50$, $Fr = 0.14$, $Fr_* = 89 \times 10^4$

Figure 3.5: Dependency of the eigenvalues from the number of points (50-400) of discretization used in the Chebyshev spectral method. The vertical axis is used simply to separate the eigenvalues with different discretization.

shown in figure 3.5. It could be seen that, starting form a sufficiently high number of discretization points, the system is quite stable: increasing the discretization, the first eigenvalues remain fixed and the new ones are all smaller than the previous. The minimum number of points depends on the relevant parameters. In addition, for very small values of the wavenumber, there is another small dependency of the eigenvalues on the number of discretization points. It has been found that a good choice for the system to be completely stable (that is, no more variations of the curves of the first eigenvalues is observed by increasing the number of discretization points) is to use about 300 discretization points.

The parameter space ($\beta \times Fr_* \times Fr$), has been explored fixing two parameters and varying the other. Some results are reported in figure 3.6. Typical values of the dimensional quantities used to calculate the dimensionless parameters are: 0.01-0.1 m for D_0^*; 0.1-1 m/s for U_C; 0.1 to 1000 m for L_0; 10^{-6} to 10^{-2} for the concentration C.

Two example of marginal stability curves in the ($k \times \beta$) and ($k \times C$)-planes

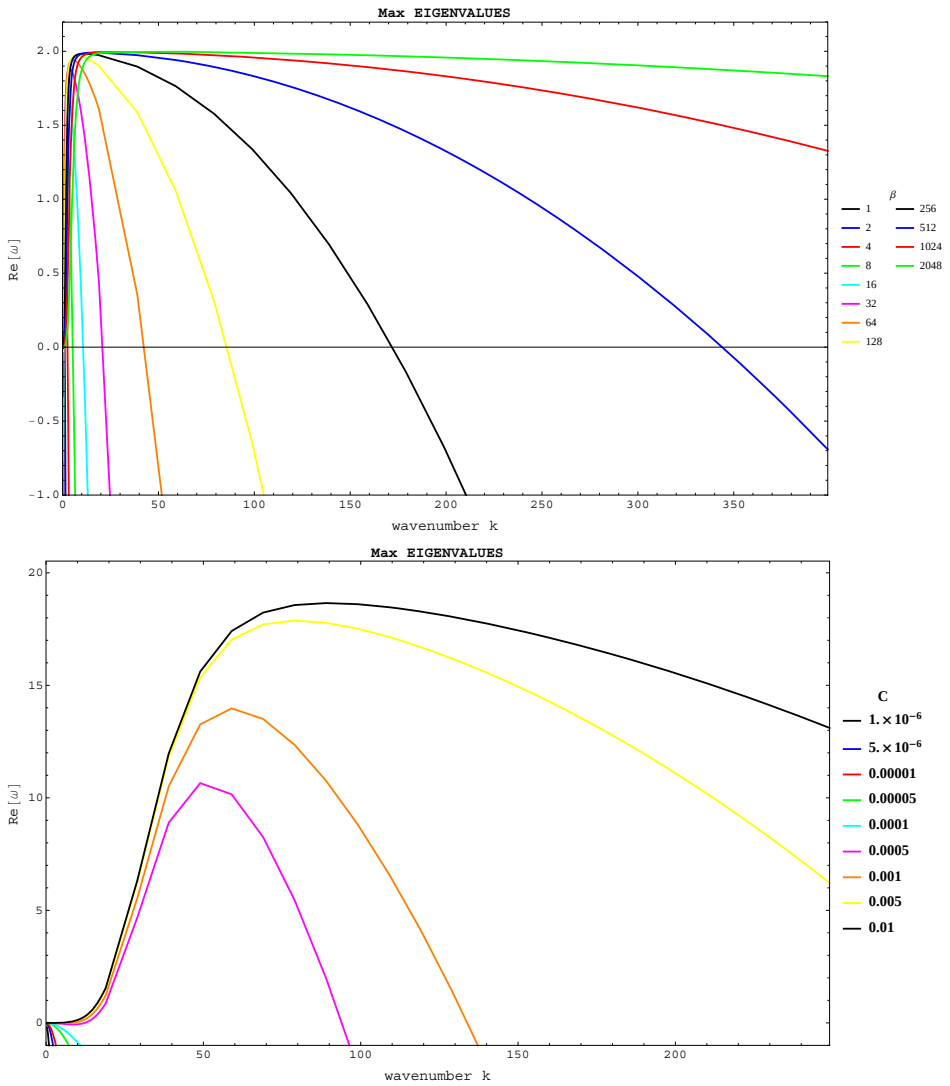

Figure 3.6: Perturabtion growth rate $Re[\omega]$ as a function of the wavenumber for different values of the parameters: for β parameter, with $Fr_* = 18 \times 10^4$ (top) and for concentration, with $\beta = 100$ (bottom).

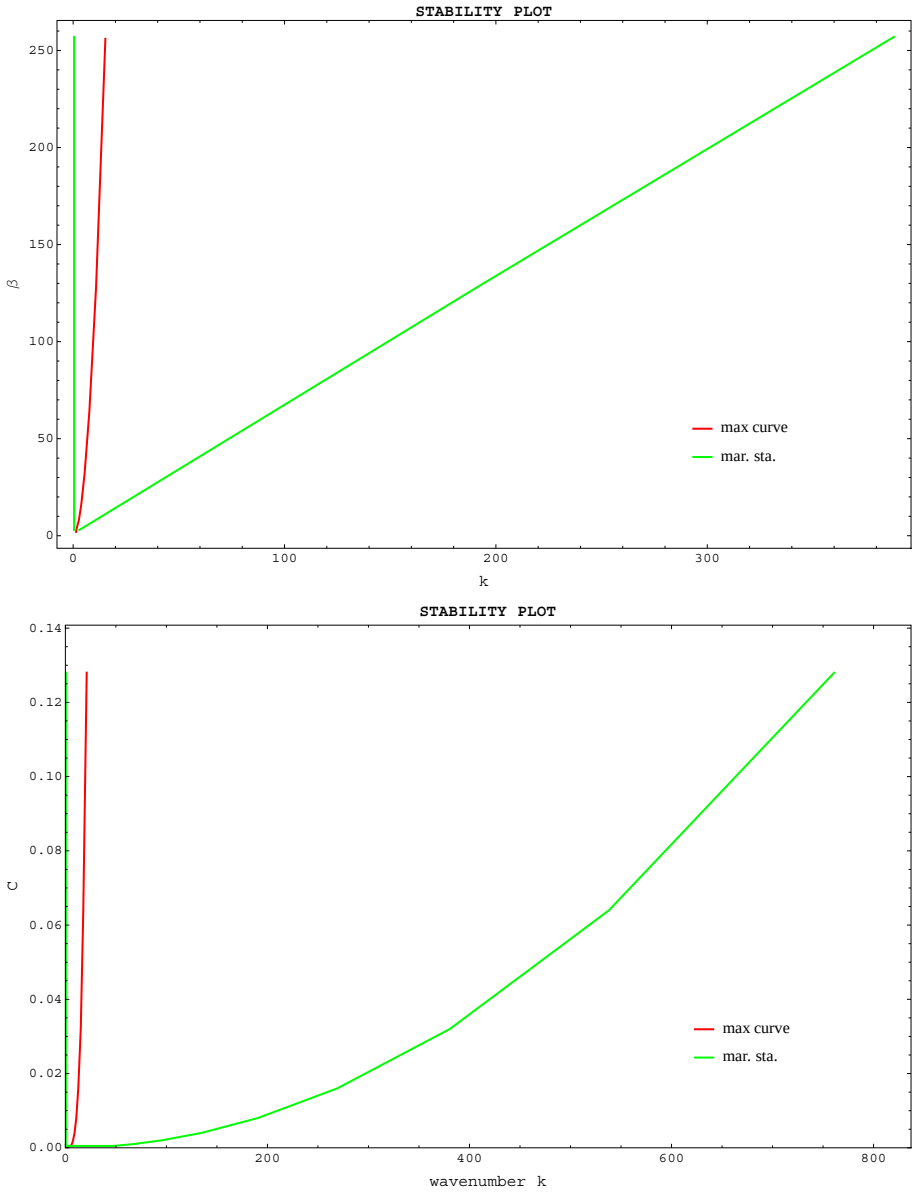

Figure 3.7: Marginal stability curve for the first mode: in the $\beta \times k$-plane for $Fr_* = 18 \times 10^4$ (top); in the $C \times k$-plane for $\beta = 100$ (bottom).

are given in figure 3.7.

The value of the wavenumber for which the maximum growth rate $Re[\omega]$ occurs, corresponds to the spacing of the periodical drainage channels. The channel inter-axis in fact is

$$L = \frac{2\pi}{k} \tag{3.65}$$

and returning to dimensional quantites

$$L^* = \frac{2\pi}{k} L_0^* \tag{3.66}$$

Figures 3.8 and 3.9 analyse the dependency from sediment concentration for different values of water depth D_0 and critical velocity for erosion U_c. The sediment concentration is varied in the range $10^{-6} - 10^{-2}$. The β parameter varies in the range $2 - 2^15$, which puts a limit in the maximum hillslope length from about 200 to 1000 meters, depending on the selected water depth. In both figures, the used value for the water depth are 0.01, 0.03 and 0.06 m, from top to bottom. Two values of the critical velocity U_c (0.2 and 0.4 m/s) have been also considered.

For a fixed set of the parameters D_0, U_c and C (i.e., a single curve in the figures 3.8 and 3.9), there is a critical limit β_c above which a stability condition occurs. This means that, to ensure the development of parallel channels with periodic spacing, the hillslope length must be greater than a minimum value (that is parameter dependent). Starting from this minimum value, the channel spacing increases with increasing the hillslope length. For a fixed sediment concentration (and fixed D_0 and U_c) a shorter hillslope implies an increase in the number of channels for unit width.

Looking at a fixed hillslope length and changing only the sediment concentration (i.e., moving along a vertical line in the figures 3.8 and 3.9), the channel spacing reduces increasing the suspended sediment concentration. In other words, at the bed for a fixed hillslope an increised erosion leads to a denser drainage network.

Increasing the water depth implies a considerable increment in channels spacing, that is a reduction of the number of channels for unit of hillslope width, as well an increment to possible hillslope lengths leading to the development of stable parallel channels with periodic spacing: the aforementioned critical values β_c becomes shorter with increasing water depth.

Finally, increasing the critical velocity U_c (i.e., increasing the grain size) tends to slightly increase the channel inter-axis.

3.9 Summary and conclusions

It has been developed a physical based model to study the formation of a network of periodic parallel drainage channel (rills).Analytical solutions are found by suitably scaling and performing a perturbation analysis. The associated eigenvalue problem is solved by Chebyshev spectral method. The channel inter-axis is derived by considering the maximum growth rate of perturbations as function of the fundamental parameters of the system: the depth of the water sheet; the length of the hill-slope; the critical velocity for erosion; the concentration at the bed. Despite the model is very simple, the results seam able to mimic the physics of drainage channel formation. The stabilizing mechanism is found to be related to the correction of bedload due to the longitudinal bed-slope. The most important parameters emerge to be the water depth and the sediment concentration; a marginal role is connected to the critical velocity for erosion, at least for the analysed values.

Clearly, in order to quantify the reliability of the predictions an extensive comparison with the results reported in literature and in field measurements needs to be carried out.

Further investigations are also worthwhile to understand a whether the introduction of the dispersive terms in the momentum equations can lead, beside longitudinal effects on bedload, to a further stabilization of the system.

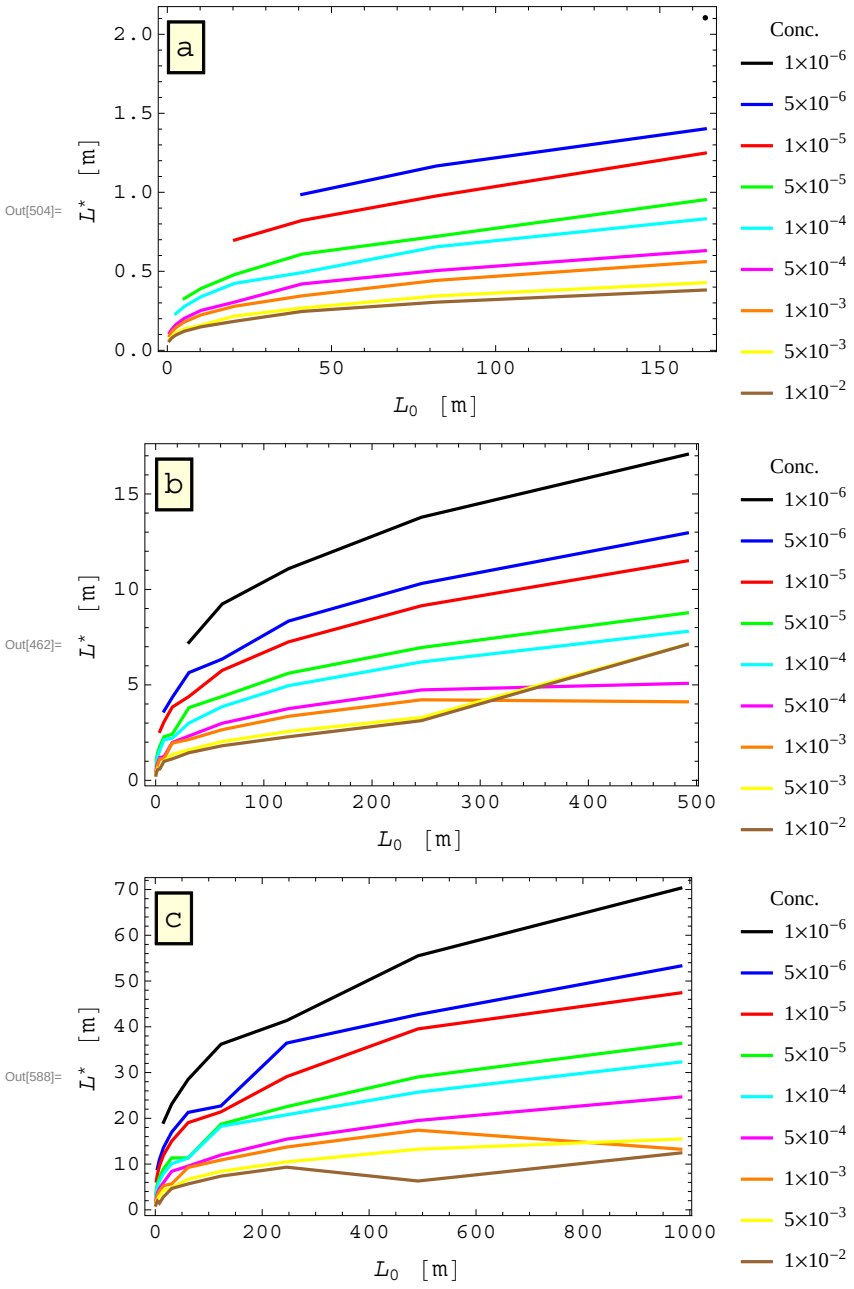

Figure 3.8: Characteristic spacing L between drainage channels as a function of the hillslope length for different selections of the various parameters: a) $D_0 = 0.01$ m; b) $D_0 = 0.03$ m; c) $D_0 = 0.06$ m. The critical velocity for sediment erosion is $U_c = 0.2$ m/s. The suspended sediment concentration C at the bed is varied in the range $10^{-6} - 10^{-2}$.

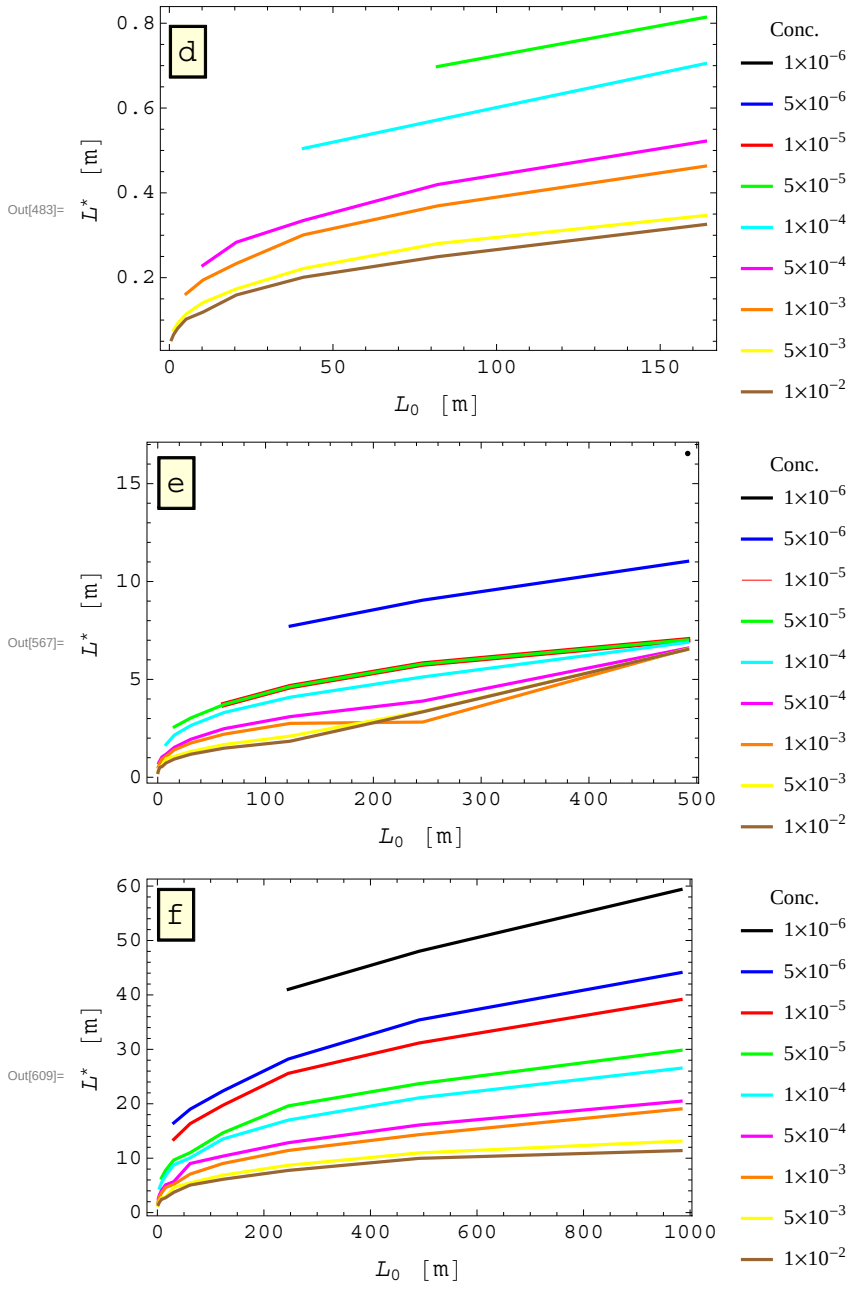

Figure 3.9: Characteristic spacing L between drainage channels as a function of the hillslope length for different selections of the various parameters: a) $D_0 = 0.01$ m; b) $D_0 = 0.03$ m; c) $D_0 = 0.06$ m. The critical velocity for sediment erosion is $U_c = 0.4$ m/s. The suspended sediment concentration C at the bed is varied in the range $10^{-6} - 10^{-2}$.

3.10 Parameters and constants

Dimensionless relevant parameters

$$d_s = \frac{d_s^*}{D_0^*} \sim 5 \times 10^{-5},\ \text{grain parameter}\ ; d_s \in \left[10^{-4}, 10^{-2}\right]$$
$$\beta = \frac{B_0^*}{D_0^*} \sim 100, \frac{\text{aspect ratio parameter}}{\text{cross section parameter}}; \beta \in [5, 30]$$
$$\vartheta_0 = \frac{C_f U_c^2}{\Delta g D_0^* d_s} \sim 0.27,\ \text{Shields parameter}\ ; \vartheta_0 \in [0.05, 0.30]$$
$$F_{r*} = \frac{U^*}{C w_s} = \frac{\sqrt{\frac{\tau_0}{\rho_w}}}{C w_s} = \frac{\sqrt{C_f \left(U_0^2 + V_0^2\right)}}{C w_s} = \frac{\sqrt{C_f U_c^2}}{C w_s} \sim 2530,\ \text{Froude parameter}$$

Dimensionless parameters

$$\chi_m = \frac{\Delta d_s}{C_f} \vartheta_0 \sim 0.004,\ \text{inertial parameter}$$
$$\chi_\tau = \Delta d_s \beta \vartheta_0 \sim 0.0016,\ \text{friction parameter}$$
$$\sigma = \frac{8 r d_s \sqrt{C_f}}{1-p} \beta^{-1} \sqrt{\vartheta_0} \sim 9.4 \times 10^{-8},\ \text{morphological time parameter}$$
$$e = \frac{1}{2r} \beta^2 \vartheta_0^{-\frac{1}{2}} \sim 1.5 \times 10^{-5},\ \text{diffusion parameter}$$
$$\vartheta_{cn} = \frac{\vartheta_c}{\vartheta_0} \sim 0.16$$
$$R = \frac{1}{r} \beta \sqrt{\vartheta_0} \sim 104$$

Accessories

$$|\tau_0^*| = \rho_w C_f \left(U_0^2 + V_0^2\right) \sim 2 \frac{kg}{m s^2},\ \text{bed shear stress}$$
$$r = 0.5,\ \text{dimensionless erosion coefficient}$$

$$Q_{s0} = \sqrt{\left(\frac{\rho_s}{\rho_w} - 1\right) g d_s^{*3}} \sim 1.2 \times 10^{-6} \frac{m^2}{s}$$

$$\Phi = 8\left(\vartheta_0 - \vartheta_c\right)^{3/2} \sim 0.88, \text{ Mayer-Peter-Muller parameter}$$

$$\Theta = \frac{|\tau_0^*|}{(\rho_s - \rho_w)\, g d_s^*} \sim 3.4, \text{ dimensionless Shields parameter}$$

Constant and characteristic values

$D_0^* \sim 0.01m$, water depth

$L_0^* \sim 10^2 m$, channel length

$U_0 \sim 0.5 \frac{m}{s}$, flow velocity

$p \sim 0.3$, porosity

$C \sim 0.0001$, mean sediment concentration

$U_c \sim 0.2 \frac{m}{s}$, threshold velocity for sediment movement

$k_s \sim 30 \frac{m^{1/3}}{s}$, roughness coefficient

$C_f \sim 0.004$, friction coefficient

$d_s^* \sim 5 \times 10^{-5} m$, sediment geometric mean size

$\rho_s \sim 2.2 \times 10^3 \frac{kg}{m^3}$, sediment mean density

$\Delta = \frac{\rho_s}{\rho_w} - 1 \sim 1.2$

$w_s \sim 5 \times 10^{-4} \frac{m}{s}$, sediment settling velocity

$\vartheta_c \sim 0.043$, dimensionless critical shear stress

$g = 9.8 \frac{m}{s^2}$, gravity acceleration

$\rho_w \sim 10^3 \frac{\mathrm{kg}}{m^3}$, water density

Appendix A

Conservation equations

Incompressible fluid mass conservation equation

$$\frac{\partial \rho}{\partial t} + \nabla \cdot (\rho \vec{u}) = 0 \tag{A.1}$$

$$\frac{d\rho}{dt} = \frac{\partial \rho}{\partial t} + (\vec{u} \cdot \nabla)\, \rho \vec{u} = \frac{\partial \rho}{\partial t} + (\rho\, (\vec{u} \cdot \nabla)\, \vec{u} + (\vec{u} \cdot \vec{u})\, \nabla \rho) = 0 \tag{A.2}$$

Since the density gradient is usually much smaller than the velocity divergence and ρ can be considered practically constant in time, the mass conservation equation can be approximated to (Batchelor, 19XX)

$$\nabla \cdot \vec{u} = 0. \tag{A.3}$$

Mass conservation equation equivalent

Integrating the mass conservation equation, $\nabla \cdot \vec{u} = 0$, over the depth, applying Leibniz integral rule and considering the kinematic boundary conditions at the water surface, $z = \eta[x, y, t]$ and at the bed $z = -H[x, y, t]$

$$\begin{cases} -u|_\eta \dfrac{\partial \eta}{\partial x} - v|_\eta \dfrac{\partial \eta}{\partial y} + w|_\eta = \dfrac{\partial \eta}{\partial t} \text{ at } z = \eta \\ u|_{-H} \dfrac{\partial H}{\partial x} + v|_{-H} \dfrac{\partial H}{\partial y} + w|_{-H} = \dfrac{\partial H}{\partial t} \text{ at } z = -H \end{cases} \tag{A.4}$$

yields

$$\frac{\partial}{\partial x}\int_{-H}^{\eta} u\,dz + \frac{\partial}{\partial y}\int_{-H}^{\eta} v\,dz = 0 \tag{A.5}$$

The first term however vanishes because of the assumption of along-estuary uniform flow condition. It then terms out that

$$\frac{\partial}{\partial y}\int_{-H}^{\eta} v\,dz = 0 \Longrightarrow \int_{-H}^{\eta} v\,dz = \text{constant for all y} \tag{A.6}$$

and the constant is zero because of the zero flux boundary condition at the banks, namely

$$\int_{-H}^{\eta} v\,dz = 0 \text{ for all y} \tag{A.7}$$

On the other hand, the along-estuary uniform flow condition implies that

$$\int_{-H}^{\eta} u\,dz = F[y] \tag{A.8}$$

and integrating across the section

$$Q = \int_{0}^{B}\int_{-H}^{\eta} u\,dz\,dy = constant \tag{A.9}$$

Hence, the flow discharge does not vary along the estuary and it is equal to $U\cos(\omega_T t)$ because of the boundary conditions.
Concluding, the integral conditions A.7 and A.9 ensure the overall mass conservation within the estuary.

Appendix B

Coriolis Force

As the Earth rotate, the momentum equations must account for centrifugal and Coriolis forces. In the local (non inertial) system the Earth angular velocity is

$$\vec{\Omega} = \begin{pmatrix} 0 \\ \Omega \cos[\varphi] \\ \Omega \sin[\varphi] \end{pmatrix} \tag{B.1}$$

with $\Omega = \frac{2\pi}{24\text{h}} \sim 7.2910^{-5} s^{-1}$ and being φ the latitude. The centrifugal force is

$$\vec{a}_{cf} = \vec{\Omega} \times \left(\vec{\Omega} \times \vec{r} \right) \tag{B.2}$$

where $\vec{r}$ is the vector from the Earth centre to the origin of the local reference system. This force can be included in the geopotential:

$$\vec{g}^{*} = -g\vec{e_3} - \vec{\Omega} \times \left(\vec{\Omega} \times \vec{r} \right) = -\nabla\Phi \tag{B.3}$$

$$\tag{B.4}$$

where $\vec{e_3}$ denotes the unit vector in the direction normal to the Earth surface and

$$\Phi = gz - \frac{(\Omega r \cos[\varphi])^2}{2} \tag{B.5}$$

The Coriolis force is given by

$$\begin{aligned}\vec{a}_C = -2\left(\vec{\Omega} \times \vec{u}\right) = -2 \begin{pmatrix} 0 \\ \Omega \cos[\varphi] \\ \Omega \sin[\varphi] \end{pmatrix} \times \begin{pmatrix} u \\ v \\ w \end{pmatrix} = \\ = -2\Omega \begin{pmatrix} w\cos[\varphi] - v\sin[\varphi] \\ u\sin[\varphi] \\ u\cos[\varphi] \end{pmatrix}\end{aligned} \tag{B.6}$$

It represents a deflecting force, which produces an acceleration perpendicular to the velocity. In particular the u components is accelerated both in the y and z direction; v component is accelerated in the x direction; w component is accelerated in the x direction. When the vertical component of the velocity is much smaller than horizontal components ($w << u, w << v$), the Coriolis force simplifies as

$$\begin{aligned}\vec{a}_C \sim -2\Omega \begin{pmatrix} -v\sin[\varphi] \\ u\sin[\varphi] \\ 0 \end{pmatrix} = -f \begin{pmatrix} -v \\ u \\ 0 \end{pmatrix} = \\ = -f \begin{pmatrix} 0 \\ 0 \\ 1 \end{pmatrix} \times \begin{pmatrix} u \\ v \\ w \end{pmatrix} = -f e_3 \times \vec{u}\end{aligned} \tag{B.7}$$

where f is the Coriolis parameter, $f = 2\Omega \sin[\varphi]$. The plane tangential to the Earth's surface (with x pointing eastward, y Northward and z positive in the outward radial direction) is called the f-plane, since Ω becomes $(0, \tilde{f}, f)$, $\tilde{f} = 2\Omega \cos[\varphi]$. Clearly the Earth's surface is a constant geopotential surface.

Appendix C

Characteristic dimensionless numbers

The importance of the various terms in the Navier-Stokes equations can be investigated using the following dimensionless numbers

$$Fr = \frac{\text{Inertial force}}{\text{Gravitational force}} = \frac{(\vec{u}\cdot\nabla)\,\vec{u}}{g} \sim \frac{U^2}{gL} \text{ Froude Number} \tag{C.1}$$

$$Eu = \frac{\text{Inertial force}}{\text{Pressure gradient force}} = \frac{(\vec{u}\cdot\nabla)\,\vec{u}}{\frac{1}{\rho}\nabla p} \sim \frac{\rho U^2}{\Delta p} \text{ Euler Number} \tag{C.2}$$

$$Ro = \frac{\text{Inertial force}}{\text{Coriolis force}} = \frac{(\vec{u}\cdot\nabla)\,\vec{u}}{2\left(\vec{\Omega}\times\vec{u}\right)} \sim \frac{U}{fL} \text{ Rossby Number} \tag{C.3}$$

$$Re = \frac{\text{Inertial force}}{\text{Frictional force}} = \frac{(\vec{u}\cdot\nabla)\,\vec{u}}{\nu\cdot\nabla^2\vec{u}} \sim \frac{UL}{\nu} \text{ Reynolds Number} \tag{C.4}$$

The Reynolds number provides an estimate of the order of magnitude of inertia terms vs frictions terms. For high enough Re, inertia tends to dominate over friction and, when a critical value Re_c is exceed, a transition occur from laminar to turbulence flow conditions. The value of Re_c depends on the investigated flow field for laminar vs turbulence behaviour of the fluid, in case of dominance of the inertial force (turbulence production) or viscous friction (turbulence dissipation) respectively. Critical Reynolds number is about 5^5.

Appendix D

Reynolds Averaged Navier-Stokes equation

The Reynolds averaged Navier-Stokes equations (RANS) are turbulence-averaged equations of motion for a Newtonian fluid. The average is taken statistically for unsteady turbulence while a time average can be used in the case of stationary turbulence (i.e., when the turbulence average quantities do not depend on time). The basic idea is the Reynolds decomposition, whereby an instantaneous quantity is decomposed into its turbulence-averaged and fluctuating components. The equations resulting from substituting this decomposition into the Navier-Stokes equations and average over the turbulence can be used to solve the flow field in terms of turbulence-average quantities. For a stationary, incompressible Newtonian fluid, these equations can be written as

$$\rho\bar{u}_j\frac{\partial\bar{u}_i}{\partial x_j} = \rho\bar{f}_i + \frac{\partial}{\partial x_j}\left(-\bar{p}\delta_{ij} + \mu\left(\frac{\partial\bar{u}_i}{\partial x_j} + \frac{\partial\bar{u}_j}{\partial x_i}\right) - \rho\overline{u_i'u_j'}\right) \tag{D.1}$$

where the over-bar represents time-averaged quantities and the prime denotes fluctuating quantities. The left-hand side represents the variation in mean momentum of fluid element owing to the convection by the mean flow. This variation is balanced by the mean body force, the isotropic stress owing to

mean pressure field, the viscous stress and Reynolds stress resulting from the fluctuating velocity field. The presence of the non-linear Reynolds stress requires additional modelling (the turbulence model) to close the system of governing equations. To derive RANS equations the starting point is the Navier-Stokes equations (NS)that for an incompressible Newtonian fluid read

$$\frac{\partial u_i}{\partial x_i} = 0 \tag{D.2}$$

$$\frac{\partial u_i}{\partial t} + u_j \frac{\partial u_i}{\partial x_j} = f_i - \frac{1}{\rho}\frac{\partial p}{\partial x_i} + \nu \frac{\partial^2 u_i}{\partial x_j \partial x_i} \tag{D.3}$$

where $\vec{f}$ represents external forces. Each instantaneous quantity is split into turbulence-averaged and fluctuating components and the resulting equations are averaged over turbulence.

Taking advantage of the definition of mean, of the linearity of the various terms (except for the convective acceleration), the continuity equation yields

$$\frac{\partial \bar{u}_i}{\partial x_i} = 0 \tag{D.4}$$

$$\tag{D.5}$$

while for momentum equation the result is

$$\frac{\partial \bar{u}_i}{\partial t} + \bar{u}_j \frac{\partial \bar{u}_i}{\partial x_j} = \bar{f}_i - \frac{1}{\rho}\frac{\partial \bar{p}}{\partial x_i} + \nu \frac{\partial^2 \bar{u}_i}{\partial x_j \partial x_i} - \frac{\partial \overline{u'_j u'_i}}{\partial x_j} \tag{D.6}$$

Last term on the right-hand side represents physically the mean transport of fluctuating momentum by turbulent velocity fluctuations, and it can be considered as an added stress on the fluid

$$\frac{\partial \bar{u}_i}{\partial t} + \bar{u}_j \frac{\partial \bar{u}_i}{\partial x_j} = \bar{f}_i - \frac{1}{\rho}\frac{\partial}{\partial x_i}\left(\bar{p}\delta_{ij} + \mu \frac{\partial \bar{u}_i}{\partial x_j} - \rho \overline{u'_j u'_i}\right) \tag{D.7}$$

It is thus possible to define the Reynolds stress tensor τ, as the turbulence-average advection of u'_i by u'_j (i.e., advection of momentum or velocity fluctuations). It leads to a spread of momentum (diffusion) by turbulence that

is independent of viscosity

$$\tau_{ij} = -\rho\overline{u_j' u_i'} = -\rho \begin{pmatrix} \overline{u'^2} & \overline{u'v'} & \overline{u'w'} \\ \overline{v'u'} & \overline{v'^2} & \overline{v'w'} \\ \overline{w'u'} & \overline{w'v'} & \overline{w'^2} \end{pmatrix} \tag{D.8}$$

The related tensor is symmetric and it introduces 6 new unknown, to be solved by a suitable closure model. Note that the total turbulent kinetic energy is one half of the τ trace. On the other hand, the continuity equation can be rewritten as

$$\frac{\partial u_i}{\partial x_i} = \frac{\partial\left(\overline{u_i} + u_i'\right)}{\partial x_i} = \frac{\partial \overline{u_i}}{\partial x_i} + \frac{\partial u_i'}{\partial x_i} = 0 \Longrightarrow \frac{\partial u_i'}{\partial x_i} = 0 \tag{D.9}$$

Hence, both the average flow field and fluctuating velocity field satisfy the average continuity condition.

Appendix E

Beaufort wind scale

The Beaufort wind scale is an empirical evaluation of wind speed by observed condition at sea or on land. It is commonly used to describe the wind force. It is divided into series of values which represent specific ranges of wind velocity; each class has a corresponding description of wind effects on some common features like trees, waves, smock, ...

Beaufort number	wind speed range (m/s)	wind description term	wind effects on land	wind effects on sea	wave height (m) probable	wave height (m) max
0	0-0.3	calm	smoke rises vertically	sea is a mirror	0	0
1	0.3-1.5	light air	smoke drift, leaves rustle	scaly ripples	0.1	0.1
2	1.6-3.3	light breeze	wind felt on face, vanes begin to move	small wavelets, glossy crests	0.2	0.3
3	3.4-5.4	gentle breeze	light flags extended, leaves move	large wavelets, crest begin to break, scattered whitecaps	0.6	1.0
4	5.5-7.9	moderate breeze	dust, leaves paper lifted, small trees branches move	small wave, some whitecaps	1.0	1.5
5	8.0-10.7	fresh breeze	small trees begin to sway	moderate waves, many whitecaps, some spray	2.0	2.5
6	10.8-13.8	strong breeze	large branches move, whistle wires	large waves, common whitecaps, more spray	3.0	4.0
7	13.9-17.1	near gale	whole trees moving, inconvenience in walking	mountain sea, white foam streaks off breakers	4.0	5.5
8	17.2-20.7	gale	difficult to walk, breaking twigs	moderately high waves, crests break into spindrift	6.0	7.5
9	20.8-24.4	strong gale	minor structural damage	high waves, dense foam, roll, spray reduce visibility	7.0	10.0
10	24.5-28.4	storm	uprooted and broken trees, structural damage	very high waves, heavy rolling, white sea, lower visibility	9.0	12.5
11	28.5-32.6	violent storm	widespread damage to structure	exceptional high waves, foam patches, poor visibility	11.5	16.0
12	32.7-36.9	hurricane	severe structural damage	air filled with foam, exceptional waves, completely white sea, bad visibility	14.0	> 16

Table E.1: Beaufort wind scale and open sea probable wave height. Are reported only the first 13 classes, because their are suffices to completely describe Adriatic Sea possible events

Bibliography

[1] A. Valle-Levinson. *Estuarine Physics*. Contemporary Issues in. 2010.

[2] W. R. Geyer. Three-dimensional tidal flow around headlands. *Journal of Geophysical Research*, 98(C1):955–966, 1993.

[3] K. M. H. Huijts. *Modelling the transverse distribution of velocity and suspended sediment in tidal estuaries*. PhD thesis, 2010.

[4] S. N. Chen, L. P. Sanford, and D. K. Ralston. Lateral circulation and sediment transport driven by axial winds in an idealized, partially mixed estuary. *Journal of Geophysical Research*, 114(C1):2006, 2009.

[5] H. Burchard, R. D. Hetland, E. Schulz, and H. M. Schuttelaars. Drivers of residual estuarine circulation in tidally energetic estuaries: straight and irrotational channels with parabolic cross section. *Journal of Physical Oceanography*, 41(3):548–570, 2011.

[6] Tjerk J. Zitman and Henk M. Schuttelaars. Importance of cross-channel bathymetry and eddy viscosity parameterisation in modelling estuarine flow. *Ocean Dynamics*, 62(4):603–631, 2012.

[7] G. P. Schramkowski and H. E. De Swart. Morphodynamic equilibrium in straight tidal channels: combined effects of the coriolis force and external overtides. *Journal of Geophysical Research*, 107(C12-3227):20,1–20,17, 2002.

[8] W.H. Munk and E.R. Anderson. Notes on a theory of the thermocline. *J. Mar. Res.*, 7:276–295, 1948.

[9] K.F. Bowden, L.A. Fairbairn, and P. Hughes. The distribution of shearing stresses in a tidal current. *Geophys. J. Roy. Astron. Soc.*, 2:288–305, 1959.

[10] K.R. Dyer. *Estuaries: a physical introduction 2nd edition.* John Wiley and sons, Chichester, 1973.

[11] H.B. Fischer, E.J. List, R.Y.C. Koh, J. Imberger, and N.H. Brooks. *Mixing in inland and coastal waters.* Academic Press, New York, 1979.

[12] T. Meissner, D. Smith, and F. Wentz. A 10 year intercomparison between collocated special sensor microwave imager oceanic surface wind speed retrievals and global analyses. *Journal of Geophysical Research*, 106(C6):11,731–11,742, 2001.

[13] P. Canestrelli, A. Cucco, F. De Biasio, G. Umgiesser, L. Zampato, and S. Zecchetto. The use of quikscat wind fields in water level modeling of the adriatic sea. 2003.

[14] Adam H. Monahan. The probability distribution of sea surface wind speeds. part i: theory and sea winds observations. *Journal of Climate*, 19:497–520, 2006.

[15] H. J. Isemer and L. Hasse. The scientific beaufort equivalent scale: effects on wind statistics and climatological air-sea flux estimates in the north atlantic ocean. *Journal of Climate*, 4(819-836), 1991.

[16] R. Wanninkhof. Relationship between wind speed and gas exchange over the ocean. *Journal of Geophysical Research*, 97(C5):7373–7382, 1992.

[17] R. Wanninkhof and W. Mc Gillis. A cubie relationship between air-sea co2 exchange and wind speed. *Geophysical Research Letters*, 26(13):1889–1892, 1999.

[18] J. Wu and I. K. Tsanis. Numerical study of wind-induced water currents. *Journal of Hydraulic Engineering*, May:388–395, 1995.

[19] S. Carniel, J. C. Warner, J. Chiggiato, and M. Sclavo. Investigating the impact of surface wave breaking on modeling the trajectories of drifters in the northern adriatic sea during a wind-storm event. *Ocean Modelling*, 30(2-3):225–239, 2009.

[20] H. Burchard. Combined effects of wind, tide, and horizontal density gradients on stratification in estuaries and coastal seas. *Journal of Physical Oceanography*, 39(9):2117–2136, 2009.

[21] X. Yang and Q. Zhang. Joint probability distribution of winds and waves from wave simulation of 20 years (1989-2008) in bohai bay. *Water Science and Engineering*, 6(3):296–307, 2013.

[22] H. K. Johnson. On modelling wind-waves in shallow and fetch limited areas using the method of holthuijsen, booij and herbers. *Journal of Coastal Research*, 14(3):917–932, 1998.

[23] L. Carniello, A. DAlpaos, and A. Defina. Modeling wind waves and tidal flows in shallow micro-tidal basins. *Estuarine Coastal and Shelf Science*, 92(2):263–276, 2011.

[24] S. Fagherazzi and P. L. Wiberg. Importance of wind conditions, fetch, and water levels on wave-generated shear stresses in shallow intertidal basins. *Journal of Geophysical Research-Earth Surface*, 114(F3), 2009.

[25] A. Jouon, J. P. Lefebvre, P. Douillet, S. Ouillon, and L. Schmied. Wind wave measurements and modelling in a fetch-limited semi-enclosed lagoon. *Coastal Engineering*, 56(5-6):599–608, 2009.

[26] I. Moller, T. Spencer, J. French, D. J. Leggett, and M. Dixon. Wave transformation over salt marshes: a field and numerical modelling study from north norfolk, england. *Estuarine Coastal and Shelf Science*, 49:411–426, 1999.

[27] M. Tonelli, S. Fagherazzi, and M. Petti. Modeling wave impact on salt marsh boundaries. *Journal of Geophysical Research*, 115(C9), 2010.

[28] G. Mariotti, S. Fagherazzi, P. L. Wiberg, K. J. McGlathery, L. Carniello, and A. Defina. Influence of storm surges and sea level on shallow tidal basin erosive processes. *Journal of Geophysical Research-Oceans*, 115(C11), 2010.

[29] L. Carniello, A. D'Alpaos, and A. Defina. The effect of wind-waves and tidal currents on sediment resuspension in shallow microtidal basin. In *XXXII Convegno Nazionale di Idraulica e Costruzioni Idrauliche*, pages 1–10, 2010.

[30] M. Marani, A. D'Alpaos, S. Lanzoni, and M. Santalucia. Understanding and predicting wave erosion of marsh edges. *Geophysical Research Letters*, 38(21), 2011.

[31] X. B. Chao, Y. F. Jia, F. D. Shields, S. S. Y. Wang, and C. M. Cooper. Three-dimensional numerical modeling of cohesive sediment transport and wind wave impact in a shallow oxbow lake. *Advances in Water Resources*, 31(7):1004–1014, 2008.

[32] P. Kessarkar, V. P. Rao, R. Shynu, I. M. Ahmad, P. Mehra, G. S. Michael, and D. Sundar. Wind-driven estuarine turbidity maxima in mandovi estuary, central west coast of india. *Journal of Earth Syst. Sci.*, 118(4):369–377, 2009.

[33] S. A. Talke and M. T. Stacey. Suspended sediment fluxes at an intertidal flat: The shifting influence of wave, wind, tidal, and freshwater forcing. *Continental Shelf Research*, 28(6):710–725, 2008.

[34] J. A. Carta, P. Ramrez, and S. Velzquez. A review of wind speed probability distributions used in wind energy analysis. *Renewable and Sustainable Energy Reviews*, 13(5):933–955, 2009.

[35] E. C. Morgan, M. Lackner, R. M. Vogel, and L. G. Baise. Probability distributions for offshore wind speeds. *Energy Conversion and Management*, 52(1):15–26, 2011.

[36] Tian Pau Chang. Estimation of wind energy potential using different probability density functions. *Applied Energy*, 88(5):1848–1856, 2011.

[37] J. Zhou, E. Erdem, G. Li, and J. Z. Shi. Comprehensive evaluation of wind speed distribution models: A case study for north dakota sites. *Energy Conservation and Management*, 51:1449–1458, 2010.

[38] A. Sarkar, S. Singh, and D. Mitra. Wind climate modeling using weibull and extreme value distribution. *International Journal of Engineering, Science and Thecnology*, 3(5):100–106, 2011.

[39] J. Waewsak, C. Chancham, M. Landry, and Y. Gagnon. An analysis of wind speed distribution at thasala, nakhon si thammarat, thailand. *Journal of Sustainable Energy and Environment*, 2:51–55, 2011.

[40] Jos Antonio Carta and Dunia Mentado. A continuous bivariate model for wind power density and wind turbine energy output estimations. *Energy Conversion and Management*, 48(2):420–432, 2007.

[41] A. Massalin and P. Canestrelli. *Il vento nellAdriatico settentrionale nel periodo 1983 2004*. Istituzione Centro Previsioni e Segnalazioni Maree, 2006.

[42] M. T. Prtenjak, Z. Pasaric, M. Orlic, and B. Grisogono. Rotation of sea/land breezes along the northeastern adriatic coast. *Annales Geophysicae*, 26:1711–1724, 2008.

[43] M. Orlic, B. Penzar, and I. Penzar. Adriatic sea and land breezes: Clockwise versus anticlockwise rotation. *Journal of Applied Meteorology*, 27:675–679, 1988.

[44] J. T. Perron, W. E. Dietrich, and J. W. Kirchner. Controls on the spacing of first-order valleys. *Journal of Geophysical Research-Earth Surface*, 113(F04016):1–21, 2008.

[45] T. R. Smith and F. P. Bretherton. Stability and the conservation mass in drainage basin evolution. *Water Resources Research*, 8(6):1506–1529, 1972.

[46] D. S. Loewenherz. Stability and the initiation of channelized surface drainage: a reassessment of the short wavelength limit. *Journal of Geophysical Research*, 96(B5):8453–8464, 1991.

[47] D. S. Loewenherz Lawrence. Hydrodynamdice scriptiofno r advectivsee diment transporpt rocesseasn d rill initiation. *Water Resources Research*, 30(11):3203–3212, 1994.

[48] N. Izumi and G. Parker. Linear stability analysis of channel inception: downstream-driven theory. *Journal of Fluid Mechanics*, 419:239–262, 2000.

[49] N. Izumi and K. Fujii. Channelization on plateaus composed of weakly cohesive fine sediment. *Journal of Geophysical Research-Earth Surface*, 111(F1), 2006.

[50] T. R. Smith and G. E. Merchant. Conservation principles and the initiation of channelized surface flows. *Natural and Anthropogenic Influences in Fluvial Geomorphology*, page 25, 1995.

[51] Terence R. Smith. A theory for the emergence of channelized drainage. *Journal of Geophysical Research*, 115(F2), 2010.

[52] S. Lanzoni and M. Tubino. Grain sorting and bar instability. *J. Fluid Mech.*, 393:149–174, 1999.

[53] A. M. Talmon, M. C. L. M. van Mierlo, and N. Struiksma. Laboratory measurements of the direction of sediment transport on transverse alluvial-bed slopes. *Journal of Hydraulic Research*, 33(4):495–517, 1995.

Acknowledgements

This work is dedicated to the memory of Angelo, friend and example in life and work, who would have been delighted in following the many ups and downs of this not only academic adventure.

I am grateful to my family, who has supported me all the time - and they are still with me, despite the hard work of the last month!

I would thank the fate for this experience, in particular for the year in the Netherlands, really an interesting experience for me and my family. I would complain against the doom for some bad fortune I was not used to.

I acknowledge Stefano for helpful discussion, for the "simple problem" I have been working on in the last 2 years, for the many things he had taught me, his supply and patience; Mario who showed me the upside of numerical methods; Marco who introduced me in this field and for the discussion in statistical analysis.

A special danke wel to the friend Henk, who was always there to help me in the bad luck. It has been a great opportunity to work with you; I enjoyed your conversation, your work and your teaching.

I acknowledge the Istituzione Centro Previsioni e Segnalazioni Maree (ICPSM) of the Venice municipality for providing the wind and tide database. In particular the author is grateful to Franca Pastore (ICPSM) for detailed description of the database and collaboration in wind data quality analysis.

This work was generously supported by Fondazione Cariparo through the Project "Dottorati di ricerca" of the year 2010 with subject "Bio-morfodinamica di ambienti lagunari e cambiamenti climatici"

The author acknowledges support from the University of Padua (Italy) and University of Delft (The Netherlands).

Thanks to everyone who contributed directly or indirectly to this research!